INTRAMOLECULAR ELECTRON TRANSFER IN MIXED-VALENCE TRIARYLAMINES

A Dissertation
Presented to
The Academic Faculty

by

Kelly Lancaster

In Partial Fulfillment
of the Requirements for the Degree
Doctor of Philosophy in the
School of Chemistry and Biochemistry

Georgia Institute of Technology
December 2009

INTRAMOLECULAR ELECTRON TRANSFER IN MIXED-VALENCE TRIARYLAMINES

Approved by:

Dr. Jean-Luc Brédas, Advisor
School of Chemistry and Biochemistry
Georgia Institute of Technology

Dr. Seth Marder
School of Chemistry and Biochemistry
Georgia Institute of Technology

Dr. David Sherrill
School of Chemistry and Biochemistry
Georgia Institute of Technology

Dr. Thomas Orlando
School of Chemistry and Biochemistry
Georgia Institute of Technology

Dr. Bernard Kippelen
School of Electrical and Computer Engineering
Georgia Institute of Technology

Date Approved: July 17, 2009

ACKNOWLEDGEMENTS

I never intended to come to graduate school for chemistry; rather, I wanted to teach, and so I gained a great deal of tutoring experience as an undergraduate at North Carolina State University. It was not until Prof. Mike Whangbo, my quantum chemistry teacher, told me I was a good candidate for graduate school that I began to consider an advanced degree in chemistry. During my last year at NC State, he created a position for me in his lab so that I might gain some research experience. It was his support that gave me the confidence to apply to graduate school, and for that, I am much indebted.

Still, I was rather naïve when I arrived at Georgia Tech. When it came time to join a group, I chose Prof. Jean-Luc Brédas based not on his research, but on the large Led Zeppelin poster in his office. It turned out not to be such a bad criterion. I cannot imagine another advisor more open to my wish to pursue teaching while in graduate school, or more patient as I learned what it meant to be a researcher.

I would like to acknowledge my committee members, two of which I had an opportunity to work with both inside and outside of class. Prof. Seth Marder, who taught me that organic chemistry is more than mechanisms, also bought textbooks for my entire chemistry class when I was an NSF graduate teaching fellow. Prof. David Sherrill, who was an excellent computational and quantum chemistry teacher, also served as a judge for a National Chemistry Week outreach event I helped organize. Prof. Bernard Kippelen and Prof. Thomas Orlando also provided support for which I am grateful.

I would like to acknowledge my coworkers, the “Bredators,” who not only taught me how to program, but also taught me about the world. In regard to the former, I also thank Ryan Pirkl, who introduced me to MATLAB. He, along with Dr. Amalia Agnew and Dr. Sigi Sanchez-Carrera, provided much needed encouragement over the years. The work in this thesis was done under the guidance of Dr. Slava Coropceanu, to whom I am much indebted, and builds on his earlier work with Dr. Chad Risko, Dr. Simon Jones and Dr. Steve Barlow. I acknowledge the helpful advice of all of them. This thesis would be incomplete, however, were it not for Dr. Susan Odom. It was she who did most of the experimental work in the chapters to follow, and she who introduced me to ESR spectroscopy. But above all, she gave a purpose to my work by being the first to take an interest in it, and for that, I am grateful.

And of course, I would like to acknowledge my parents. I am only here because of the importance they placed on education in our home. It was my mom who, always with book in hand, passed on to me a love of the written word. Through our walks in the woods, my dad taught me to appreciate nature; through our time spent with educational toys, he gave me the tools with which to study it. It was he who taught me how to be a good student, but more than that, he showed me how to be a good person. I owe all of my success, in school and in life, to him.

TABLE OF CONTENTS

LIST OF TABLES

LIST OF FIGURES

LIST OF ABBREVIATIONS

AM1	Austin Model 1
CC	Coupled Cluster
CI	Configuration Interaction
CV	Cyclic Voltammetry
DFT	Density Functional Theory
DPV	Differential Pulse Voltammetry
ESR	Electron Spin Resonance
ET	Electron Transfer
HF	Hartree-Fock
HOMO	Highest-Occupied Molecular Orbital
IV	Intervalence
LUMO	Lowest-Unoccupied Molecular Orbital
MV	Mixed-Valence
NIR	Near Infrared
NPB	N,N'-diphenyl-N,N'-(1-naphthyl)-1,1'-biphenyl-4,4'-diamine
PKS	Piepho-Krausz-Schatz
SOMO	Singly-Occupied Molecular Orbital
TD	Time-Dependent
TPD	N,N'-diphenyl-N,N'-(3-methylphenyl)-1,1'-biphenyl-4,4'-diamine
UV	Ultraviolet
VT	Variable-Temperature

SUMMARY

Mixed-valence compounds are of interest as model systems for the study of electron transfer reactions. In Chapter 1, we find that the intramolecular electron transfer processes and patterns of charge delocalization in such compounds depend on the interplay between the electronic (V) and the vibronic (λ) coupling. One can obtain both parameters from a Hush analysis of the intervalence band that arises upon *optical* intramolecular electron transfer if the band is intense and well-separated from other bands. This is quite often the case for mixed-valence triarylamines. As such, both Hush analysis and simulation of the intervalence band are widely used to classify these types of compounds as charge localized (class-II) or delocalized (class-III). Yet one must estimate the diabatic electron transfer distance (R) to calculate V in the Hush formalism. For mixed-valence triarylamines, R is commonly taken as the N–N distance; Chapters 3 and 4 show this to be a poor approximation in many cases.

In Chapter 2, we find that the activation barrier to *thermal* intramolecular electron transfer in a class-II mixed-valence compound is also related to the parameters V and λ. Thus, if one can capture the rate of thermal electron transfer at multiple temperatures, then two experimental methods exist by which to extract V and λ. One technique that is widely used for organic mixed-valence compounds is variable-temperature electron spin resonance (ESR) spectroscopy. This method is only rarely used to determine thermal electron transfer rates in mixed-valence triarylamines, though, as the electron transfer in most of the class-II compounds is too fast to observe on the ESR timescale. Chapters 4

and 5 show, for the first time, that one can use ESR spectroscopy to measure thermal electron transfer rates in mixed-valence triarylamines for which an intervalence band is also observable. Simulation of ESR spectra based on density functional theory calculations and comparison with optical data can also uncover the nature (i.e., adiabatic or nonadiabatic) of the electron transfer process.

While Chapters 1 and 2 introduce the theory behind the two intramolecular electron transfer pathways in mixed-valence compounds, and Chapters 3–5 show that one can observe and correlate optical and thermal electron transfer in certain two- and three-center triarylamines, Chapter 6 is largely an outlook chapter. There, we find that two types of intervalence states can coexist within a single molecule. It is also this final chapter which shows that the concept of bridge energy and its effect on electronic coupling can reconcile the central results of the thesis.

The reader shall find a large amount of experimental data in the chapters to follow. *The author does not intend to imply that any of this work is her own.* Indeed, most of the data in Chapters 3–5 are the work of Dr. Susan Odom, Dr. Simon Jones and Dr. Stephen Barlow. Dr. Susan Odom, in particular, characterized the thiophene-based compounds and recorded most of the ESR spectra. The experimental data in Chapter 6 is culled from the literature. The main contribution of the author is not in the collection of data, but rather in the interpretation of the data from a theoretical viewpoint. It was the synergy between experiment and theory that led to the most important contributions of this thesis, and so both are given weight here.

CHAPTER 1

OPTICAL INTRAMOLECULAR ELECTRON TRANSFER IN MIXED-VALENCE TRIARYLAMINES

1.1 Introduction to Mixed-Valence Compounds

"Mixed-valence" compounds are those that contain groups that are identical but for their states of oxidation. In one compound is thus found both oxidizing and reducing agents. An example of an organic mixed-valence compound with two such redox centers is shown in Figure 1.1. In this example, the centers are equivalent by symmetry, so that an interchange of valences results in an equivalent structure. To convert from one form to another involves the transfer of one electron. Already, one might ask: Is the electron localized as is drawn in the valence bond structure, or is it delocalized over both centers? The attempt to answer this question for mixed-valence triarylamines is one of the central aims of this chapter and those that follow.

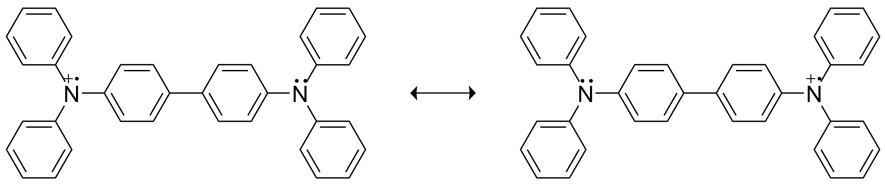

Figure 1.1 Example of a two-center mixed-valence triarylamine

The true beauty of mixed-valence compounds, however, is that their properties are rarely just the sum of those of the redox centers taken separately. One such property of many mixed-valence compounds is the presence of an intense absorption in the electronic spectrum, one that cannot be attributed to either redox center alone. The absorption of light is instead due to an oscillation between valences. This optical electron

transfer gives rise to the intense colors seen in many mixed-valence compounds, particularly those with metal centers. It was this feature that led to the creation of the field of mixed-valence chemistry, and it is here that we begin.

1.2 Classification of Mixed-Valence Compounds

Not all mixed-valence compounds exhibit an "intervalence" band. Before an optical electron transfer can occur, the redox centers must interact. Robin and Day were among the first to recognize that mixed-valence properties depend on the extent of delocalization of the valence electrons.[1] The classification scheme they devised over 40 years ago remains in wide use today.

The salient features of Robin and Day's depiction of mixed-valence wave functions are as follows. Consider a two-center mixed-valence compound, such as that shown in Figure 1.1. Let us call the wave function for the form on the left ψ_a, and call that for the form on the right ψ_b. The extent of delocalization in the ground state wave function, ψ_1, is described in terms of the mixing of wave functions ψ_a and ψ_b:

$$\psi_1 = \sqrt{1-\alpha^2}\psi_a + \alpha\psi_b \qquad 1.1$$

Robin and Day's classification scheme is based upon the value of α. A class-I compound is defined as one where $\alpha = 0$. No mixing occurs in the ground state of the mixed-valence compound; i.e., $\psi_1 = \psi_a$. In a class-I compound, the electron is thus completely localized on one redox center. At the other extreme, a class-III compound is one for which $\alpha = 1/\sqrt{2}$. The ground state is thus an equal mixture of both wave functions, and the electron is completely delocalized over both redox centers. A class-II compound is defined for

the intermediate case in which some delocalization occurs ($\alpha > 0$), but the redox centers are still distinguishable. The classes are summarized in Table 1.1.

Table 1.1 Classification of mixed-valence compounds

Class	Ground state wave function	Description
I	ψ_a	Completely localized
II	$\sqrt{1-\alpha^2}\psi_a + \alpha\psi_b$	Intermediate
III	$\frac{1}{\sqrt{2}}(\psi_a + \psi_b)$	Completely delocalized

The real import of α, however, is that the intensity of an intervalence band depends upon its value. No intervalence absorption occurs in a class-I compound because no mixing occurs ($\alpha = 0$). The spectra of class-I compounds are merely sums of the spectra of the constituent centers. In contrast, class-II compounds do exhibit an absorption which is absent in the spectra of the redox centers taken separately ($\alpha > 0$). Robin and Day noted that the energy of the optical transition is equal to the changes in internal energy of the redox centers upon gaining or losing an electron[1] – a point also noted by Hush.[2] In later sections, we shall see that the location of the intervalence band for a class-III compound depends not on this "reorganization" energy, but rather on the interaction between centers.

1.3 Hush Theory of Intervalence Absorption

In parallel to Robin and Day, Hush formed his own theory of optical electron transfer in mixed-valence compounds.[2] Both models are based on the extent to which an electron can be regarded as localized at a particular center. By virtue of its more

quantitative nature, however, any attempt to extract information from an intervalence band is called a "Hush analysis." The theory of Hush follows.

1.3.1 Correlation of Band Intensity and Electron Delocalization

Hush noted that the intensity of an intervalence absorption depends on the degree of electron delocalization in the mixed-valence compound. Like Robin and Day, Hush used the parameter α to describe the amount of mixing between the localized wave functions ψ_a and ψ_b. He then compared the oscillator strength of the optical transition to that for a general band of Gaussian shape to obtain a correlation between α and the intervalence band intensity. As α is also related to the electronic coupling, V, between the redox centers, this gave the famous Hush equation:[3]

$$V = \frac{0.0206}{R}\sqrt{\varepsilon_{max}\nu_{max}\Delta\nu_{1/2}} \qquad 1.2$$

Here, ν_{max} (in cm^{-1}) is the energy of the band maximum, $\Delta\nu_{1/2}$ (in cm^{-1}) is the full-width at half-maximum, ε_{max} (in $M^{-1}cm^{-1}$) is the extinction coefficient of the band maximum, and R (in Å) is the distance between redox centers in the absence of electronic coupling. The numerical factor is a combination of fundamental constants evaluated to give V in cm^{-1}. In contrast to the other parameters, R is not directly available from optical data. For mixed-valence triarylamines, R is often taken as the N–N distance; later chapters show this to be a poor approximation.

The band intensity thus provides a measure of the interaction between redox centers. It must be noted, however, that Equation 1.2 applies only to Gaussian-shaped intervalence bands. This is true for many class-II compounds, but not for compounds near the class-II/III borderline. An equation applicable to all classes of mixed-valence

compounds was needed. One such relation was implicit in the derivation of the Hush equation, but went unnoticed for nearly 30 years:[4,5]

$$V = \frac{\mu_{12} \nu_{max}}{eR} \qquad 1.3$$

In this expression, μ_{12} is the transition dipole moment of the intervalence band, e is the electronic charge, and the other parameters are the same as before. Though no assumption about the band shape is made, R remains ill-defined. For the particular case of Gaussian-shaped bands, Equation 1.3 leads to Equation 1.2.

1.3.2 Correlation of Band Width and Absorption Energy

Hush also derived a relationship between the intervalence band width and the absorption maximum:[2]

$$\Delta\nu_{1/2} = \sqrt{16 \ln 2 k_B T \times \nu_{max}} = \sqrt{2310 \times \nu_{max}} \qquad 1.4$$

The second equality is obtained when $\Delta\nu_{1/2}$ and ν_{max} are in cm^{-1}, and the temperature is 300 K. One may thus compute the absorption energy from the band width, and vice versa. But both values are available from optical data, so what is the utility of such a relation? The answer comes from the fact that the Hush equations were derived for mixed-valence compounds in which the centers interact only weakly; that is, for class-II compounds. Any deviation from Equation 1.4 implies that this condition is not met. In later sections, we shall see that mixed-valence compounds with band widths smaller than those predicted by Equation 1.4 are often assigned to class-III.

1.4 Potential Energy Surfaces

Most of the Hush relations apply only to class-II compounds. For a treatment pertinent to all classes, we turn to the potential energy surfaces for a two-center mixed-valence compound. To begin, we define wave functions for the valence bond structures pictured in Figure 1.1. That is, we again define ψ_a as the wave function for the form on the left, while ψ_b is the wave function for that on the right. As pointed out before, the two centers are equivalent by symmetry; hence, ψ_a and ψ_b are degenerate. The diabatic potential energy for each form – before any interaction between the centers is allowed – is given by Equation 1.5:[6]

$$E_a = \lambda q^2 \qquad 1.5$$

$$E_b = \lambda(q-1)^2$$

In writing such an equation, we assume that the diabatic states are harmonic with identical force constants. Here, q is a dimensionless reaction coordinate, while λ is defined as the reorganization energy. E_a and E_b give identical parabolas, but are displaced along coordinate q.

Let us now allow the centers to interact. In the localized basis of ψ_a and ψ_b, the electronic Hamiltonian is given by:

$$H = \begin{bmatrix} E_a & H_{ab} \\ H_{ab} & E_b \end{bmatrix} \qquad 1.6$$

where $H_{ab} = \langle \psi_a \mid H \mid \psi_b \rangle$ is the electronic coupling matrix element. Coupling of the diabatic states leads to an avoided crossing at the intersection of the two parabolas. This

gives rise to two adiabatic surfaces, which are obtained by solving the secular determinant. The lower root corresponds to the ground state of the mixed-valence compound. As shown in Figure 1.2, the splitting at the avoided intersection is twice the electronic coupling matrix element of the secular equation.

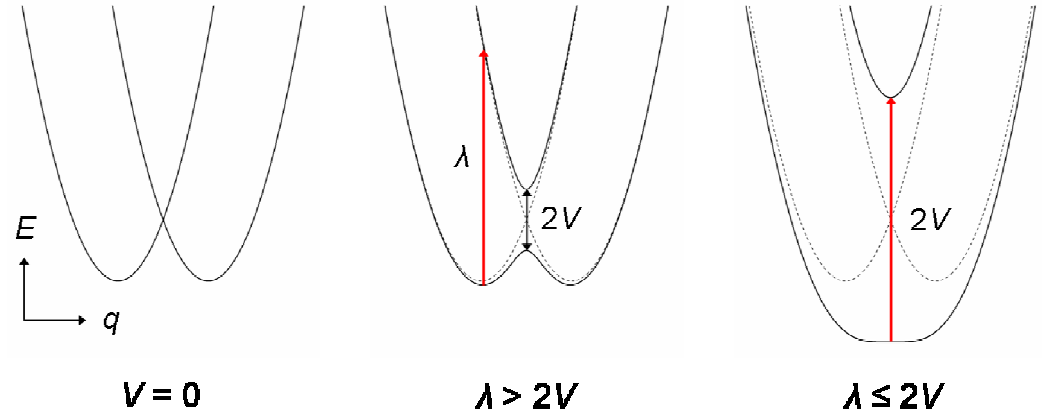

Figure 1.2 Potential energy surfaces for a two-center mixed-valence compound

H_{ab} is often referred to as V, and is done so here as well. When $V = 0$, one simply recovers the two diabatic surfaces. This is the case for a class-I compound. When $V \neq 0$, but $\lambda > 2V$, the ground state is described by a double well potential. The two equivalent minima correspond to two "broken-symmetry" states wherein the electron is mainly localized on one of the redox centers. This is the case for a class-II compound. The vertical separation of the curves from either of the adiabatic minima is equal to the energy of the intervalence transition; i.e.:

$$\lambda = \nu_{max} \qquad 1.7$$

Equation 1.7 was first published by Hush.[2] Finally, when $\lambda \leq 2V$, the ground state has only one minimum. This is the case for a class-III compound. The absorption maximum

is no longer a measure of the reorganization energy, but is instead a measure of the electronic coupling:

$$V = \frac{\nu_{max}}{2} \qquad 1.8$$

There are thus two ways in which to calculate V for a class-III compound. This is important because it allows one to estimate the correct value of R to enter in Equation 1.3. The relevant equations for each class of compound are collected in Table 1.2.

Table 1.2 Classification of mixed-valence compounds, part II

Class	Condition	Equations
I	$V = 0$	None
II	$\lambda > 2V$	$V = \frac{\mu_{12}\nu_{max}}{eR}$, $\lambda = \nu_{max}$
III	$\lambda \leq 2V$	$V = \frac{\mu_{12}\nu_{max}}{eR}$, $V = \frac{\nu_{max}}{2}$

1.5 Electron Delocalization in Mixed-Valence Triarylamines

We saw that the relative sizes of λ and V define the shape of the lower potential surface. The microscopic parameters, in turn, depend on the nature of the "bridge" connecting the centers. In what follows, we look at how Hush theory was applied to determine the effect of the bridge on the electronic coupling in two-center mixed-valence triarylamines. But first, the reader may wonder, why study mixed-valence triarylamines? The main consideration is of a practical nature. In order to apply a Hush analysis, the intervalence band must be intense and well-separated from other bands. This is quite

often the case for mixed-valence triarylamines. The monocations of two-center triarylamines also tend to be quite stable, which further facilitates the study of their mixed-valence properties.

Of equal import is the relevance of mixed-valence triarylamines to the field of organic electronics. Indeed, one of the first reports of an organic light-emitting diode used a thin film of a two-center triarylamine as the hole transport layer.[7] The charge carrier in this case was thus a mixed-valence compound. Examples of two-center triarylamines that continue to find application as organic semiconductors are shown in Figure 1.3.[8,9] Understanding the properties of such compounds is thus important for the optimization of electronic devices.

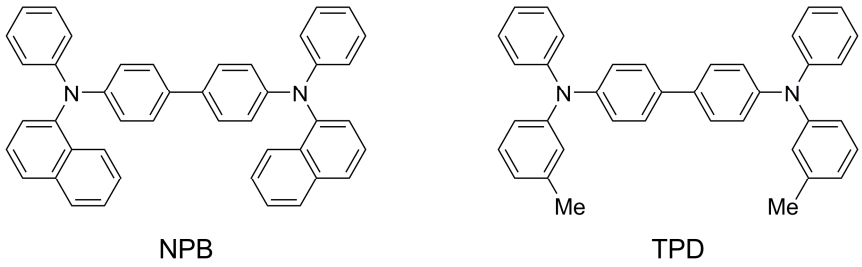

NPB TPD

Figure 1.3 Examples of two-center triarylamines used as hole transport layers in organic electronic devices

1.5.1 Effect of Bridge Length on Electronic Coupling

We begin with the work of Lambert and Nöll. To determine the effect of distance on the electronic coupling between two redox centers, they prepared a series of two-center triarylamines with varying bridge lengths.[10,11] Examples of the compounds are shown in Figure 1.4.

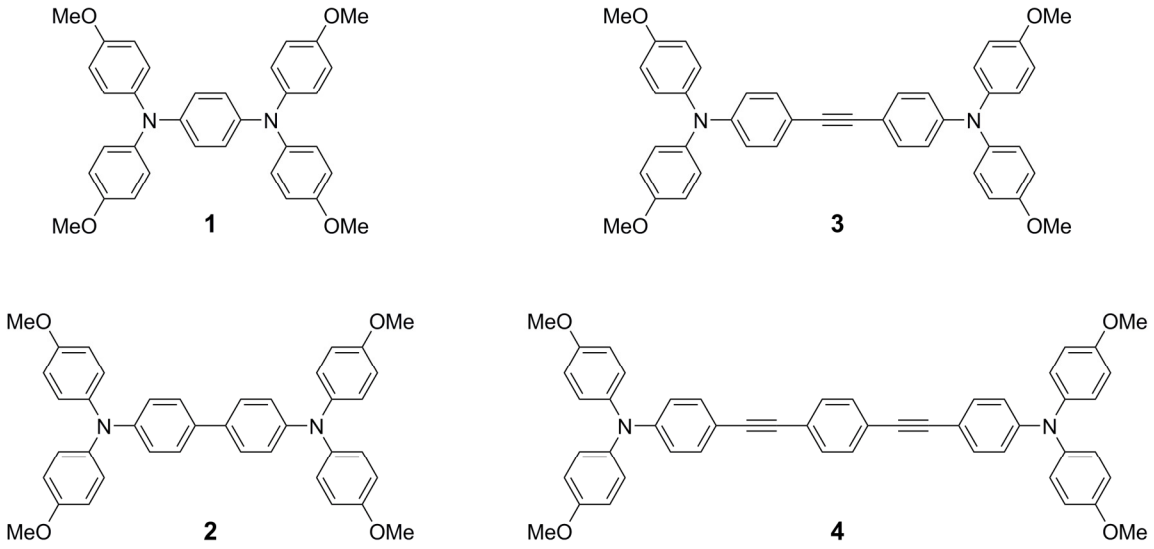

Figure 1.4 Examples of two-center triarylamines with different bridge lengths

The monocations of **1**–**4** showed intervalence bands in the near-IR region that were both intense and well-separated from other bands, and were thus amenable to Hush analysis. As the distance between redox centers decreased, the shape of the intervalence band became less symmetric, with the band width on the low energy side more narrow than that at high energy. Lambert and Nöll attributed the asymmetry to a cutoff at 2*V*, but it was later found that such a band shape is characteristic of many class-III mixed-valence triarylamines.[12] The microscopic parameters obtained from Hush analysis of the intervalence bands are collected in Table 1.3.

Table 1.3 Hush analysis of the intervalence bands for the monocations of **1**–**4**[a]

Compound	ν_{max} (cm^{-1})	$V_{Eq.1.3}$ (cm^{-1})	$V_{Eq.1.8}$ (cm^{-1})	Class
1	9530	3240	4770	III
2	6360	1550	3180	III
3	6190	1200	–	II
4	9490	500	–	II

[a] From Ref. 11.

Due to the asymmetry of the intervalence bands, the electronic coupling was evaluated using Equation 1.3. The diabatic electron transfer distance *R* was simply taken as the N–N separation. In each case, $V_{Eq.1.3}$ was smaller than $\nu_{max}/2$, and thus all were originally assigned as class-II mixed-valence compounds. A later study found, however, that the monocations of **1** and **2** belong to class-III, and so Equation 1.8 also applies.[12] The values of *V* computed from both equations are given in Table 1.3; the discrepancy between the two values is due to the approximation of *R* as the N–N distance in Equation 1.3. The diabatic states thus cannot be regarded as centered on the N atoms, but are displaced somewhat into the bridge.

As expected, the electronic coupling was found to decrease with distance between redox centers. Not only is *V* affected by distance, but so is electron delocalization – Lambert and Nöll showed that one can transform a mixed-valence triarylamine from class-II to class-III simply by varying the bridge length.

1.5.2 Effect of Bridge Saturation on Electronic Coupling

Not long after the seminal work of Lambert and Nöll, Barlow and coworkers synthesized a series of analogous two-center triarylamines in which the alkyne (C≡C) groups were replaced with alkene (HC=CH) groups.[13,14] The aim was to determine the effect of bridge saturation on the electronic coupling between redox centers. Examples of the compounds are shown in Figure 1.5.

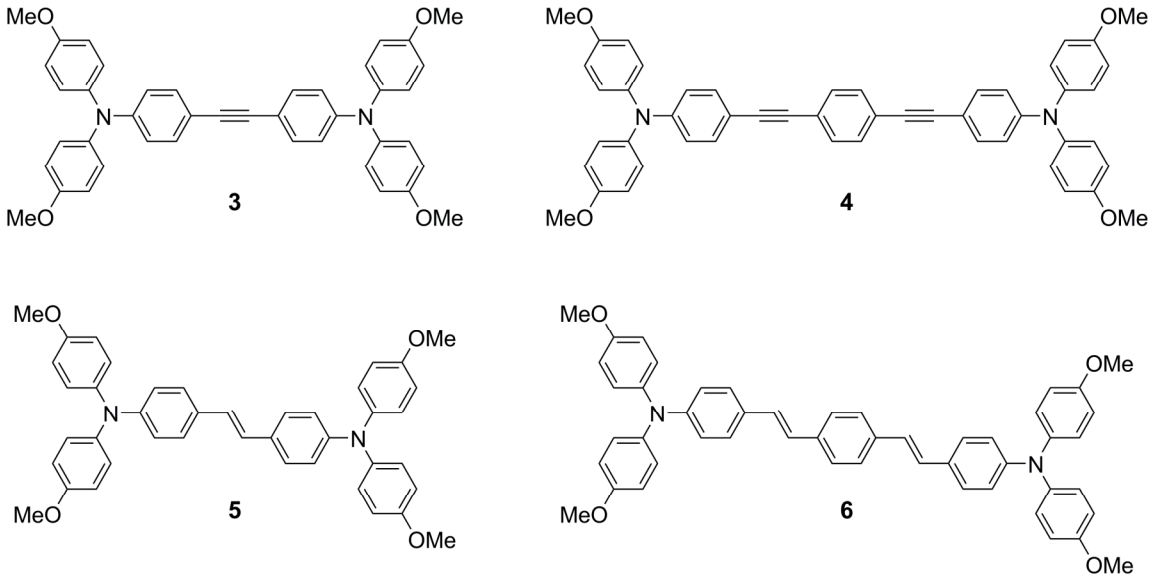

Figure 1.5 Examples of two-center triarylamines with different bridge saturation

Like their alkyne counterparts, the monocations of **5** and **6** showed intense intervalence bands in the near-IR region. The microscopic parameters from a Hush analysis of the optical bands are collected in Table 1.4.

Table 1.4 Hush analysis of the intervalence bands for the monocations of **3**–**6**[a]

Compound	ν_{max} (cm^{-1})	$V_{Eq.1.3}$ (cm^{-1})	$V_{Eq.1.8}$ (cm^{-1})	Class
3	5760	1080	–	II
5	6080	1400	3040	III
4	7780	490	–	II
6	6130	700	–	II

[a] From Refs. 13 and 14.

The intervalence band of $\mathbf{5}^+$ was asymmetric, and the width at half-height was less than the Hush limit given by Equation 1.4. Both features are those expected of class-III compounds. More evidence of delocalization was provided by the solvatochromism of the intervalence band – for class-III compounds, one expects only small shifts of the

absorption maximum upon changing the solvent polarity. This is because an optical electron transfer involves no change in dipole moment for a delocalized compound. The intervalence band of $\mathbf{5}^{+}$ showed only weak solvatochromism, and was thus assigned to class-III. In this case, one can estimate the electronic coupling using both Equations 1.3 and 1.8; comparison of the values indicated that the diabatic electron transfer distance *R* is considerably less than the N–N distance.

The monocations of the other compounds in the series were assigned to class-II based on their intervalence band shapes and solvatochromism. Barlow et al. thus showed that one could transform a mixed-valence triarylamine from class-II to class-III simply by varying the amount of bridge saturation.

1.5.3 Effect of Bridge Energy on Electronic Coupling

We saw that varying the bridge length and/or saturation has a large impact on the interaction between redox centers. In both cases, however, one is also varying the energy of the bridge. The longer bridges are easier to oxidize due to longer conjugation lengths – the energy of the highest occupied orbital increases with conjugation. Alkene (HC=CH) groups are as well more readily oxidized than alkyne (C≡C) groups. It is instructive then to compare compounds for which the only deviation is the bridge energy. Examples of such compounds are shown in Figure 1.6.

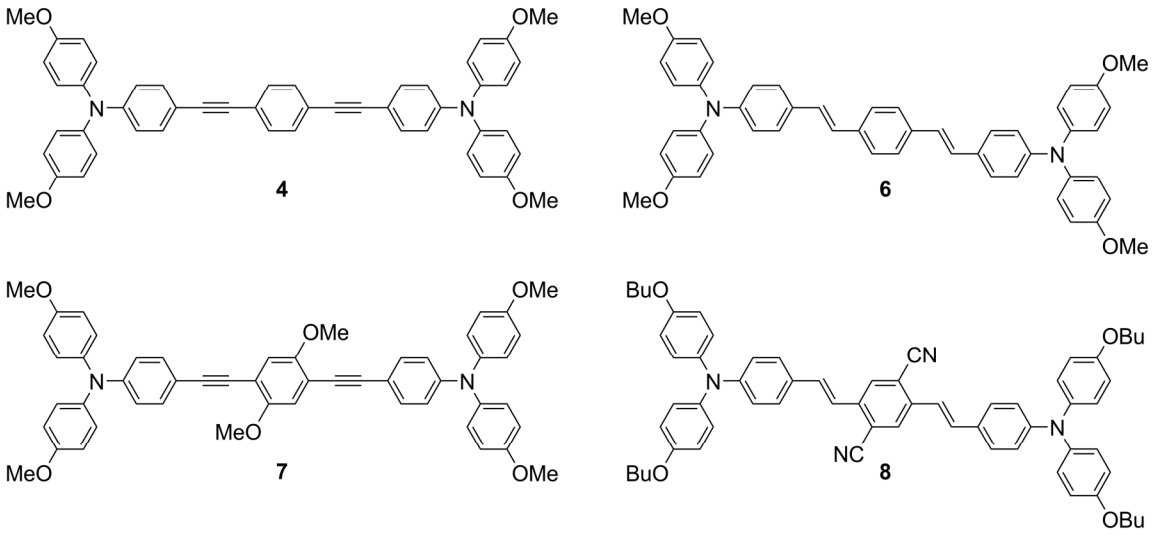

Figure 1.6 Examples of two-center triarylamines with different bridge energy

In one case, an electron-donating methoxy group was added to the bridge (**4** vs. **7**).[15,16] This should increase the bridge energy with respect to that of the parent compound. In the other case, an electron-withdrawing cyano group was added to the bridge (**6** vs. **8**).[17] This should decrease the bridge energy. The microscopic parameters obtained from a Hush analysis of the intervalence bands are collected in Table 1.5.

Table 1.5 Hush analysis of the intervalence bands for the monocations of **4**, **6**–**8**[a]

Compound	ν_{max} (cm^{-1})	$V_{Eq.1.3}$ (cm^{-1})	Class
4	8060	540	II
7	6520	670	II
6	6130	700	II
8	7450	480	II

[a] From Refs. 15 and 17.

In both pairs, the electronic coupling was found to increase with bridge energy. This is presumably due to an enhancement of resonance between the bridge orbitals and those of the redox centers. Not only is *V* affected by the ease with which the bridge can

be oxidized, but so is the absorption maximum. In both pairs, ν_{max} occurs at lower energy for the mixed-valence compound with the more electron-rich bridge. This shift can be attributed to a reduced solvent contribution to the reorganization energy; that is, the larger the extent of delocalization in the ground state, the less that solvent must reorient upon electron transfer.

1.6 Calculation of Electron Delocalization

In the last section, we saw that it can be difficult to assign two-center mixed-valence triarylamines to a particular class, as many fall near the class-II/III borderline. One might ask: Why not assign a compound based on the symmetry in its crystal structure? The reason is two-fold. A compound that is symmetric in solution can be asymmetric in the crystal due to the localizing influence of a counterion. At the same time, a compound that is asymmetric in solution can appear symmetric in the crystal due to crystallographic disorder. A crystal structure can only provide evidence, not proof, of a class-II or class-III compound. One might then ask: Why not simply compute the geometry with electronic structure methods? In the two cases to follow, we shall see why this is no simple matter.

1.6.1 Case of Localized Class-II Compound, Optimized Geometry Delocalized

We begin our case study with density functional theory, for which its developer, Walter Kohn, was awarded a Nobel Prize. DFT is based on a proof that the ground-state energy of a nondegenerate system is a unique functional of the electron density.[18,19] The density depends on only three coordinates, whereas the wave function depends on the coordinates of each electron. DFT methods are thus computationally much cheaper than wave function methods that contain the same amount of electron correlation, and they are

often used to study large organic compounds. The exact density functional is unknown, however, and must be approximated. As we shall see shortly, this can lead to error.

In the previous section, we saw that the monocation of **3** is a class-II mixed-valence compound. One would thus expect $\mathbf{3}^+$ to exhibit broken symmetry. An unrestricted DFT optimization, however, predicts a symmetric geometry. This is evident in the nature of the highest singly-occupied orbital – hereafter referred to as the SOMO – and by the equal spin density, ρ_N, on each N atom. The change in geometry upon losing an electron is identical for both triarylamines, which also shows that the charge in $\mathbf{3}^+$ is equally distributed over both centers.

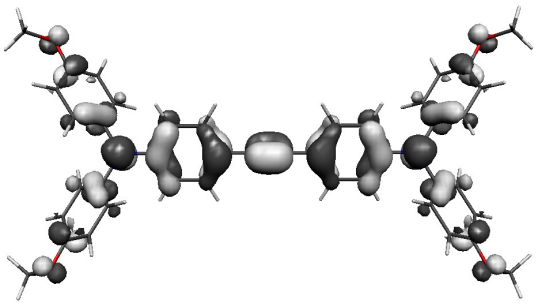

Figure 1.7 Highest singly-occupied orbital for $\mathbf{3}^+$ as computed with DFT

Table 1.6 DFT-computed[a] spin densities for the N atoms in $\mathbf{3}^+$

	N_1	N_2
ρ_N	0.16	0.16

[a] Using the B3LYP functional and the 6-31G(d,p) basis set

The failure of DFT in this case is due to the approximate nature of density functionals. The Coulomb term in such a functional contains the spurious interaction of an electron with itself. For an *exact* density functional, this "self-interaction" error is compensated by the exchange-correlation term. For an approximate density functional,

the terms no longer cancel. It is well-known that when redox centers are identical, the Coulomb repulsion is dominant and favors the distribution of charge over both centers.[20,21] DFT methods are thus prone to artificial delocalization of an unpaired electron. This is clearly not an issue when a mixed-valence compound is, in fact, delocalized. If a compound belongs to class-III, one can obtain good agreement between DFT and experiment. In this case, it is even possible to calculate the intervalence band directly; for that, one may use time-dependent DFT.

1.6.2 Case of Delocalized Class-III Compound, Optimized Geometry Localized

We turn now to our next case: the semi-empirical AM1 method.[22] In contrast to DFT, AM1 is a wave function method, albeit one in which only a minimal basis is used. Like other semi-empirical methods, AM1 neglects certain integrals and parameterizes others to compensate for the approximation. AM1 is often used to study large organic compounds due to its low computational cost. In this case, we use unrestricted AM1 to optimize the geometry of the monocation of **5**.

As we saw in the previous section, $\mathbf{5}^{+}$ is a class-III mixed-valence compound. One would thus expect a symmetric geometry. The AM1 optimization, however, gives a broken symmetry. This is evident in the localized nature of the SOMO, shown in Figure 1.8, and by the unequal spin density on each N atom, shown in Table 1.7. The change in geometry is also more pronounced for one of the triarylamine centers.

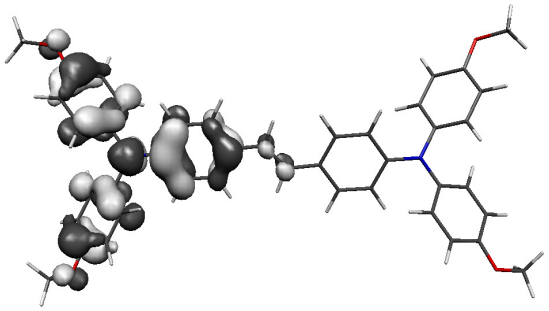

Figure 1.8 Highest singly-occupied orbital for $\mathbf{5}^+$ as computed with AM1

Table 1.7 AM1-computed spin densities for the N atoms in $\mathbf{5}^+$

	N_1	N_2
ρ_N	0.08	0.57

The failure of AM1 to predict a symmetric geometry is a result of the unrestricted wave function; that is, the spatial orbitals are not constrained to be identical for α and β spins. This can introduce "spin contamination," where the wave function contains spurious contributions from higher spin states. The amount of spin contamination is given by the expectation value of the S^2 operator. For a pure doublet state, this value is 0.75; the AM1 value for $\mathbf{5}^+$, however, is larger than 2. In general, the unrestricted AM1 method tends to localize an unpaired electron. As a corollary, AM1 correctly predicts an asymmetric geometry for the class-II mixed-valence monocation of **3**.

In both cases, one would assign an incorrect class based on computation alone. That is, DFT over-delocalizes class-II compounds, while AM1 over-localizes class-III compounds. In the chapters to follow, DFT is used, but with caution.

1.7 Simulation of Intervalence Band

The degree of delocalization in a mixed-valence compound depends on the interplay between the reorganization energy (λ) and the electronic coupling (V). As we saw in a previous section, one can obtain both parameters from a Hush analysis of the intervalence band. To calculate V, however, one must estimate R, the diabatic electron transfer distance. In mixed-valence triarylamines, this distance is not well-defined. In what follows, we outline an alternative approach: one can simulate the absorption band, and thereby extract the microscopic parameters. The values of λ and V are those that give the best fit to experiment.

We return now to our earlier potential energy surfaces. Such curves are solutions to the "static" problem; that is, they do not include T, the nuclear kinetic energy operator. To solve the full "dynamic" problem, one must allow nuclear motion. The adiabatic wave functions do not commute with T, however, and thus they cannot be used to predict absorption profiles. Be that as it may, the curves in Figure 1.2 are often used to simulate the intervalence band. In so doing, one assumes that: 1) the Born-Oppenheimer approximation is valid, 2) the vibrational wave functions overlap only at the classical turning points, and 3) the vibrational levels are not quantized. Such a treatment predicts a cutoff on the low energy side of the band at $2V$.[11,23] At best, however, this provides only a qualitative picture.

That brings us to the model of Piepho, Krausz and Schatz.[24,25] The PKS model marked the first solution of the dynamic problem for a two-center mixed-valence compound. The reader is referred to Appendix A for details of the derivation. In short, the model provides the vibronic eigenvalues and eigenfunctions for any class of

compound, be it valence trapped or not. One can then calculate the position and intensity of each transition that contributes to the intervalence band. As we show below, however, the PKS model is not without its own limitations.

In the PKS model, all parameters are defined in units of $h\nu_-$, where ν_- is the frequency associated with coordinate q_-. Here, q_- is an anti-symmetric linear combination of vibrations localized on the redox centers. In the delocalized basis of ψ_+ and ψ_-:

$$\psi_{\pm} = \frac{1}{\sqrt{2}}\left(\psi_a \pm \psi_b\right) \tag{1.9}$$

the vibronic Hamiltonian is given by:

$$\frac{H}{h\nu_-} = \begin{bmatrix} \frac{1}{2}\left(\dot{q}_-^2 + q_-^2\right) + \varepsilon & lq_- \\ lq_- & \frac{1}{2}\left(\dot{q}_-^2 + q_-^2\right) - \varepsilon \end{bmatrix} \tag{1.10}$$

As before, ψ_a and ψ_b correspond to the wave functions of the diabatic states. The reorganization energy is related to l, while the electronic coupling is given by ε. Both parameters are without dimension. To define an energy scale, one must assign a value to ν_-. In theory, this value can be estimated from vibrational data, but in practice, ν_- is chosen rather arbitrarily. This is one limitation of the PKS model. Given the values of l, ε, and ν_-, one can solve the secular determinant. The resulting eigenvalues and eigenfunctions are then used to simulate the intervalence band. To compare with experiment, one must assign a shape to each vibronic line. This is typically done with Gaussian functions of arbitrary width. This is yet another limitation. The most serious

limitation of the PKS model, however, is the neglect of two-center vibrations. Such are the modes that govern the *distance* between redox centers.

Coropceanu et al. were the first to apply the PKS model to a mixed-valence triarylamine.[26] In their study of the class-III cation of **1**, an initial guess for ε was obtained from an electronic structure calculation. All other parameters were obtained by fit to experiment. As shown in Figure 1.9, no combination of parameters was able to reproduce the high energy side of the intervalence band for $\mathbf{1}^+$. Coropceanu et al. noted that this was because the PKS model includes vibronic coupling to only one vibrational mode (q_-).[12] The model was later reformulated by Piepho to include coupling to symmetric, two-center vibrations (q_+).[27] One expects q_+ to play an important role in delocalized compounds, whereas q_- plays the major role in more localized mixed-valence compounds. As shown in Figure 1.9, a better fit for $\mathbf{1}^+$ was obtained by including vibronic coupling to q_+; in fact, coupling to q_- had little effect on the band shape for this class-III compound.

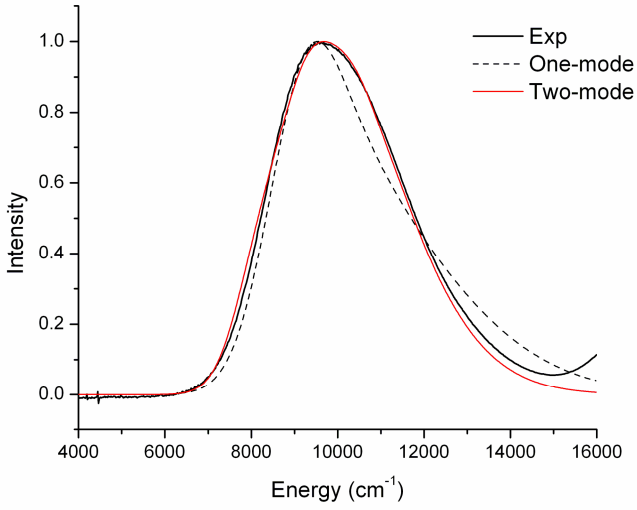

Figure 1.9 Intervalence band for the monocation of **1** and fits using the one-mode or two-mode vibronic coupling models[12]

The shape of an intervalence band thus depends on the interaction with symmetric (q_+) and anti-symmetric (q_-) modes. If the coupling with two-center vibrations is strong, the intervalence band can be broad even in the case of class-III compounds. Thus, the shape of the band alone is not a good measure of the degree of delocalization. We saw that the Hush formalism has limitations as does the more elaborate PKS model. Clearly, an alternative means by which to extract the microscopic parameters is needed. Such is the subject of the next chapter.

REFERENCES

[1] Robin, M. B.; Day, P. *Adv. Inorg. Chem. Radiochem.* **1967**, *10*, 247.

[2] Hush, N. S. *Prog. Inorg. Chem.* **1967**, *8*, 391.

[3] Hush, N. S. *Electrochim. Acta* **1968**, *13*, 1005.

[4] Creutz, C.; Newton, M. D.; Sutin, N. *J. Photochem. Photobiol. A: Chem.* **1994**, *82*, 47.

[5] Cave, R. J.; Newton, M. D. *Chem. Phys. Lett.* **1996**, *249*, 15.

[6] Sutin, N. *Prog. Inorg. Chem.* **1983**, *30*, 441.

[7] Tang, C. W.; Van Slyke, S. A.; *Appl. Phys. Lett.* **1987**, *51*, 913.

[8] Kido, J.; Kimura, M.; Nagai, K. *Science* **1995**, *267*, 1332.

[9] Van Slyke, S. A.; Chen, C. H.; Tang, C. W. *Appl. Phys. Lett.* **1996**, *69*, 2160.

[10] Lambert, C.; Nöll, G. *Angew. Chem. Int. Ed.* **1998**, *37*, 2107.

[11] Lambert, C.; Nöll, G. *J. Am. Chem. Soc.* **1999**, *121*, 8434.

[12] Coropceanu, V.; Malagoli, M.; André, J. M.; Brédas, J.-L. *J. Am. Chem. Soc.* **2002**, *124*, 10519.

[13] Barlow, S.; Risko, C.; Coropceanu, V.; Tucker, N. M.; Jones, S. C.; Levi, Z.; Khrustalev, V. N.; Antipin, M. Y.; Kinnibrugh, T. L.; Timofeeva, T.; Marder, S. R.; Brédas, J.-L. *Chem. Commun.* **2005**, 764.

[14] Barlow, S.; Risko, C.; Chung, S.-J.; Tucker, N. M.; Coropceanu, V.; Jones, S. C.; Levi, Z.; Brédas, J.-L.; Marder, S. R. *J. Am. Chem. Soc.* **2005**, *127*, 16900.

[15] Lambert, C.; Nöll, G.; Schelter, J. *Nat. Mater.* **2002**, *1*, 69.

[16] Lambert, C.; Amthor, S.; Schelter. J. *J. Phys. Chem. A* **2004**, *108*, 6474.

[17] Lancaster, K.; Odom, S. A.; Jones, S. C.; Thayumanavan, S.; Marder, S. R.; Brédas, J.-L.; Coropceanu, V.; Barlow, S. *J. Am. Chem. Soc.* **2009**, *131*, 1717.

[18] Hohenberg, P.; Kohn, W. *Phys. Rev.* **1964**, *136*, B864.

[19] Kohn, W.; Sham, L. J. *Phys. Rev.* **1965**, *140*, A1133.

[20] Merkle, R.; Savin, A.; Preuss, H. *J. Chem. Phys.* **1992**, *97*, 9216.

[21] Bally, T.; Sastry, G. N. *J. Phys. Chem. A* **1997**, *101*, 7923.

[22] Dewar, M. J. S.; Zoebisch, E. G.; Healy, E. F.; Stewart, J. J. P. *J. Am. Chem. Soc.* **1985**, *107*, 3902.

[23] Nelsen, S. F. *Chem. Eur. J.* **2000**, *6*, 581.

[24] Piepho, S. B.; Krausz, E. R.; Schatz, P. N. *J. Am. Chem. Soc.* **1978**, *100*, 2996.

[25] Wong, K. Y.; Schatz, P. N. *Prog. Inorg. Chem.* **1981**, *28*, 369.

[26] Coropceanu, V.; Malagoli, M.; André, J. M.; Brédas, J.-L. *J. Chem. Phys.* **2001**, *115*, 10409.

[27] Piepho, S. B. *J. Am. Chem. Soc.* **1988**, *110*, 6319.

CHAPTER 2

THERMAL INTRAMOLECULAR ELECTRON TRANSFER IN MIXED-VALENCE TRIARYLAMINES

2.1 Introduction to Mixed-Valence Compounds, Part II

In the previous chapter, we saw that interaction with light can induce an optical electron transfer in a mixed-valence compound, and that the intensity of the absorption depends on the amount of coupling between redox centers. But the intervalence band provides only a static picture of the electron transfer process. There is, of course, another way for an electron transfer to occur – thermal activation can also induce an oscillation of valence. This thermal electron transfer also depends on the degree of delocalization in the ground state. Another question that may arise is thus: If the electron is indeed localized, how *fast* do the two forms interconvert? The attempt to answer this question for mixed-valence triarylamines is the subject of the present chapter.

The study of electron transfer in solution is complicated when the transfer is between unconnected redox centers. The rate depends, among other factors, on the distance between the redox centers when the transfer occurs. In mixed-valence compounds, this distance is defined. Also, for the compounds considered here, the reactants are identical to the products. The driving force for the electron transfer reaction is thus zero, which further simplifies the problem. Mixed-valence compounds make ideal model systems for the study of electron transfer reactions. In what follows, the same equations apply whether the centers are linked or not.

2.2 Marcus Theory of Electron Transfer

We begin with the theory of Marcus, on which the field of electron transfer in chemistry is based and for which he was awarded a Nobel Prize.[1–4] Marcus studied reactions that involved the transfer of an electron only – those like the one depicted in Figure 2.1, where no bonds are broken or formed.

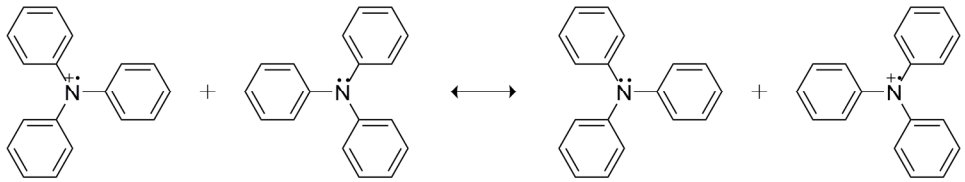

Figure 2.1 Example of *inter*molecular electron transfer

Marcus was the first to represent the potential energy of such a reaction as two displaced parabolas.[2] He noted that an electron transfer can only occur at or near the intersection of the two curves. In this way, the Franck-Condon principle is obeyed and energy is conserved. Marcus also noted that thermal fluctuations of the coordinates are needed to reach the intersection; that is, the solvent must reorient prior to electron transfer. The rate of thermal electron transfer will thus depend on the energy of this reorganization. Marcus wrote the rate constant of the reaction as:[1]

$$k_{\mathrm{ET}} = A \exp\left(\frac{-\Delta G^*}{k_B T}\right) \qquad 2.1$$

where k_{B} is the Boltzmann constant and T is temperature. In the next section, we shall see that the prefactor, A, depends on the nature of the electron transfer reaction. ΔG^* is the activation barrier to electron transfer and is given by:

$$\Delta G^* = \frac{\left(\lambda + \Delta G^0\right)^2}{4\lambda} \qquad 2.2$$

Thus, the activation barrier depends on λ, the reorganization energy. There are two contributions to λ: an "inner" part due to the changes in bond length upon loss or gain of an electron, and an "outer" part due to reorientation of the solvent. While Marcus derived formulas for both contributions, Hush showed later that one need not always calculate the reorganization energy – in certain cases, one can obtain λ directly from experiment.[5–6]

From Equation 2.2, we find that ΔG^* depends not only on λ, but also on the driving force for the reaction, $\Delta G°$. One of the more famous contributions of Marcus was his prediction of an "inverted" region in which the rate of electron transfer decreases with increasing driving force.[2] This result ran counter to chemical intuition. The so-called "normal" and inverted regions are illustrated in Figure 2.2. We see that the activation barrier will first decrease as $\Delta G°$ is varied from zero to some negative value, vanish at $\Delta G° = -\lambda$, and then increase when $\Delta G°$ is made still more negative.

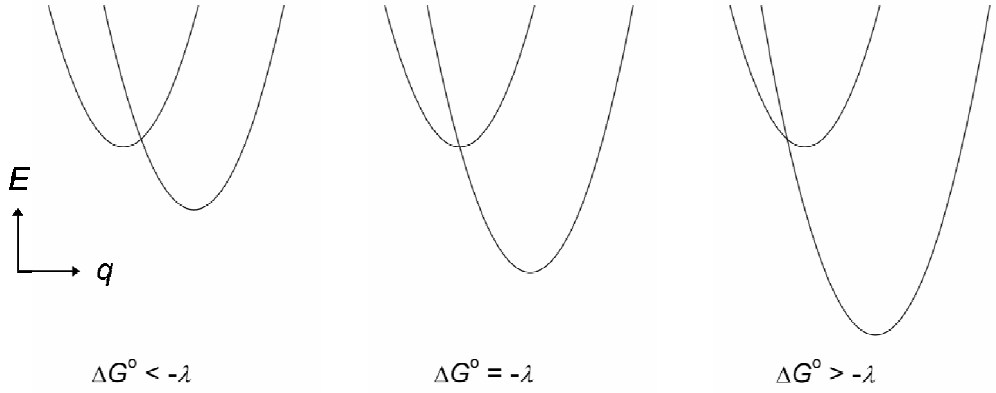

Figure 2.2 Potential energy surfaces for the "normal" and "inverted" regions

As noted earlier, the driving force is zero for the mixed-valence compounds considered here. The thermal electron transfer will thus always take place in the normal region. Our focus will instead be on the nature of the electron transfer reaction. For that, we turn to the prefactor *A*.

2.2.1 Adiabatic vs. Nonadiabatic Electron Transfer

Not all systems that reach the intersection region automatically undergo an electron transfer. The probability of forming products depends on the amount of coupling between the two reactants. When *V* is large, the reaction will proceed solely along the lower surface in Figure 2.3. That is, every trajectory that reaches the transition state will lead to products. Such reactions are called adiabatic. If, however, *V* is small, a given trajectory may easily "jump" over the small gap, remaining on the reactant surface without passing over to the product surface. The reaction can reach the transition state many times without leading to products. Such reactions are called nonadiabatic. The prefactor *A* depends on which regime is operable.

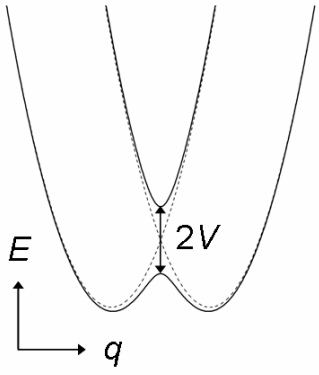

Figure 2.3 Potential energy surfaces for a class-II mixed-valence compound

In Marcus theory, the nuclear motion is treated classically, so the model cannot allow for the possibility that an electron transfer may not occur in the intersection region. We apply the semiclassical treatment of Sutin in what follows.[7] The prefactor *A*, no matter the regime, is given by Equation 2.3:

$$A = \nu_n \kappa_{el} \tag{2.3}$$

In this equation, ν_n is the frequency of nuclear motion along the reaction coordinate, and κ_{el} is the probability that an electron transfer will occur in the intersection region. The latter term is given by:

$$\kappa_{el} = \frac{2 - 2\exp\left(\frac{-\nu_{el}}{2\nu_n}\right)}{2 - \exp\left(\frac{-\nu_{el}}{2\nu_n}\right)} \tag{2.4}$$

where ν_{el} is an electronic frequency:

$$\nu_{el} = V^2 \sqrt{\frac{4\pi^3}{h^2 \lambda k_B T}} \tag{2.5}$$

The prefactor *A* thus depends on the interplay between the nuclear and electronic frequencies. When the electronic motion is slower than the nuclear motion ($\nu_{el} << \nu_n$), it follows that $\kappa_{el} = \nu_{el}/\nu_n$ and

$$A = \nu_{el} \tag{2.6}$$

This limit corresponds to the nonadiabatic case. The prefactor no longer depends on the frequency of nuclear motion, but is instead a function of the electronic coupling.

Otherwise, when the electronic motion is faster than the nuclear motion ($\nu_{el} >> \nu_n$), it follows that $\kappa_{el} = 1$ and

$$A = \nu_n \qquad 2.7$$

This limit corresponds to the adiabatic case. The prefactor depends solely on the nuclear frequency of crossing the barrier, and the system moves from the reactant to the product surface upon every passage through the intersection region. One of the goals of this thesis is to determine to which regime the intramolecular electron transfer in mixed-valence triarylamines belongs.

2.2.2 Optical vs. Thermal Electron Transfer

At its inception, Marcus theory applied only to "outer-sphere" electron transfer reactions – those in which the redox centers do not share a common ligand. Hush showed later that the same equations apply if one then connects the two redox centers to form a mixed-valence compound.[5] An example of this "inner-sphere" electron transfer was given in Figure 1.1. For mixed-valence compounds, we saw that one can obtain λ from a Hush analysis of the intervalence band that arises upon optical electron transfer: i.e., $\lambda = \nu_{max}$. This is the very same reorganization energy that appears in the equations for thermal electron transfer. The energy of the optical transition is thus related to the activation energy of the thermal transition:

$$\Delta G^* = \frac{\lambda}{4} = \frac{\nu_{max}}{4} \qquad 2.8$$

In this way, Hush was able to link the two pathways of electron transfer. In deriving Equation 2.8, both Marcus and Hush assumed little overlap of the electronic orbitals of

the two redox centers; it holds only in the limit of weak interaction. It is more appropriate to include the coupling, which, as shown in Figure 2.3, acts to lower the activation barrier:[7]

$$\Delta G^* = \frac{(\lambda - 2V)^2}{4\lambda} \qquad 2.9$$

When $V = 0$, as in a class-I mixed-valence compound, the activation barrier is given by Equation 2.8. In this case, however, the lack of orbital overlap precludes both optical and thermal electron transfer. When $\lambda \leq 2V$, as in a class-III compound, the activation barrier no longer exists. In this case, the electron is completely delocalized and no thermal electron transfer occurs. We find then that thermal electron transfer is only possible for class-II mixed-valence compounds.

In the last chapter, we saw that the energy and shape of the intervalence band depend on the electronic (V) and vibronic (λ) coupling. In this chapter, we find that the thermal activation barrier depends as well on both parameters. Thus, if one can capture the rate of thermal electron transfer at multiple temperatures, then two experimental techniques exist by which to extract V and λ. For mixed-valence compounds, the reactant and product are, by definition, identical. This fact precludes the use of any form of optical spectroscopy to follow the rate of electron transfer. One technique that is widely used for organic mixed-valence compounds is variable-temperature electron spin resonance spectroscopy. An overview of this technique is next.

2.3 Electron Spin Resonance Spectroscopy of Organic Radicals

Due to its spin, an electron possesses a magnetic moment. By virtue of its magnetic moment, an electron can interact with an external magnetic field. As shown in Figure 2.4, the interaction energy is different for α and β spins. This difference is called the Zeeman splitting, and is proportional to the strength, B, of the external magnetic field. In electron spin resonance (ESR) spectroscopy, transitions between the two energy levels are induced by electromagnetic radiation. The resultant ESR signal is usually recorded as the first derivative of the absorption with respect to B.

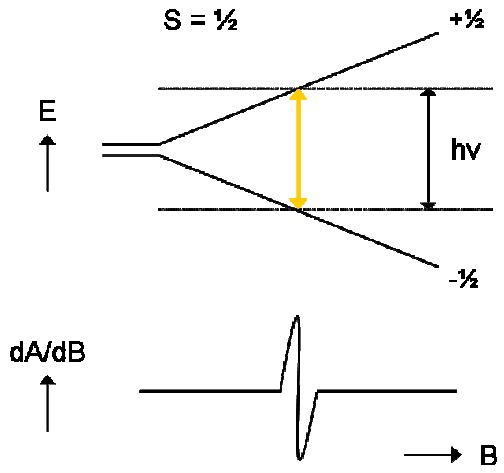

Figure 2.4 Zeeman splitting as a function of the strength, B, of the magnetic field

An electron can also interact with a magnetic ($I \neq 0$) nucleus. This interaction is much weaker than the Zeeman interaction, and can be treated as a perturbation – as shown in Figure 2.5, it splits every Zeeman energy level into several sublevels. This "hyperfine" interaction does not depend on B, and is the sum of a classical dipolar term and a quantum mechanical Fermi contact term. The dipolar interaction is anisotropic and is generally averaged out to zero in solution. The hyperfine splitting in the ESR spectra

of the organic radicals considered here is thus exclusively due to the isotropic Fermi contact term. This term is proportional to the spin density at the nucleus, ρ_X, where it is "contacted" by the unpaired electron.

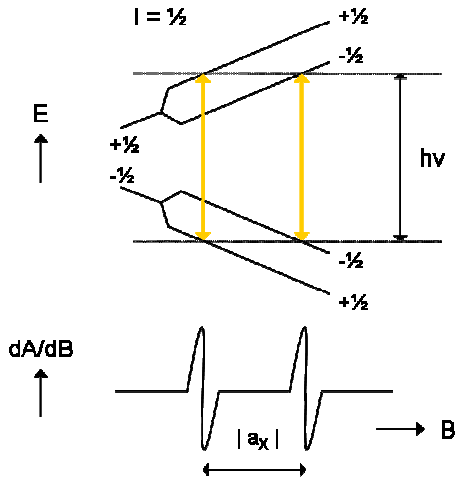

Figure 2.5 Hyperfine splitting of the Zeeman levels for a nucleus with $I = ½$

According to the ESR selection rules, two transitions are allowed for a nucleus with $I = ½$. The distance between the lines is the absolute value of the hyperfine coupling constant, a_X. This constant is diagnostic of the interaction between the nucleus, X, and the unpaired electron in a given radical, and is given by Equation 2.10. Here, we find that a_X depends on both K_X and ρ_X, where K_X is characteristic of the nucleus. In this way, ESR spectroscopy can provide information on the degree of delocalization of the unpaired electron in a mixed-valence compound.

$$a_X = K_X \rho_X \qquad 2.10$$

Only the absolute value of the coupling constant can be derived from an ESR spectrum. The sign of a_X depends on those of K_X and ρ_X. In the compounds to follow,

only ^{1}H (I = ½) and ^{14}N (I = 1) are magnetic, and for both, K_X is positive. The sign of a_X is thus reflected by that of the spin density. A positive value of ρ_X signifies that the probability of finding the unpaired electron with α spin in the orbital ψ is larger than that for β spin. If electron correlation is neglected, the spin density is determined solely by the squared wave function, ψ^2, of the singly-occupied orbital. An electron in a π-type orbital would thus have no spin density at any nucleus. If this were indeed the case, no hyperfine splitting would be observed in the ESR spectrum for any of the compounds considered here. This is not the case, however, because the unpaired electron spin *polarizes* the spins of the formally paired electron spins in the doubly occupied orbitals, so that the latter are no longer perfectly paired.

2.4 Calculation of Hyperfine Coupling Constants

An ESR spectrum is not always helpful in locating an unpaired electron. It is often difficult to assign a hyperfine coupling constant to a particular atom in the radical. It can also be difficult to extract small values of a_X from an ESR spectrum. An electronic structure calculation, on the other hand, gives the spin density of every atom in the compound, large or small. As we saw in the section above, the sign of a_X is not provided by an ESR experiment. In a calculation, however, the sign of the spin density, and thus the sign of the hyperfine coupling, is known. Calculation is thus a good complement to experiment. Below, we shall see that the hyperfine splitting is very sensitive to the basis set used and the amount of electron correlation included in the calculation.

2.4.1 Effect of Basis Set

In the previous section, we saw that the isotropic Fermi contact term depends on the spin density at the nucleus. To calculate ESR properties, one needs a basis set that

can adequately describe the wave function in this region. Most basis sets are composed of Gaussian functions, however, which do not satisfy the correct cusp condition at the nucleus. This problem can be overcome by using large basis sets, or, more effectively, by adding very tight *s* functions. Such a basis set was designed by Barone and coworkers.[8–9] Their EPR-II basis set was optimized for the computation of hyperfine coupling constants by DFT methods. As shown in Table 2.1, the EPR-II basis set contains twice as many contracted *s* functions as the 6-31G(d,p) basis.[10] EPR-III is a triple-zeta version of the double-zeta EPR-II.

Table 2.1 Comparison of basis sets by Pople[10] and Barone[8–9]

Basis set	H	B–F
6-31G(d,p)	(4s,1p) → [2s,1p]	(10s,4p,1d) → [3s,2p,1d]
EPR-II	(6s,1p) → [4s,1p]	(10s,5p,1d) → [6s,2p,1d]
EPR-III	(6s,2p) → [4s,2p]	(11s,7p,2d,1f) → [7s,4p,2d,1f]

To determine the effect of basis set size, we computed the hyperfine coupling constants of a triarylamine (TAA) monocation that will factor prominently in later chapters. The ESR spectrum of TAA^+ is given in Figure 2.6,[11] and the a_X values are collected in Table 2.2. As expected, we find that DFT to tends to over-delocalize the charge; the value of $a_{H(methyl)}$ is much larger than the experimental value. To our surprise, however, the 6-31G(d,p) basis gives better agreement than the larger EPR basis sets. The value of a_N is particularly low when using the basis sets of Barone. The accuracy of the Pople basis set could be due to a fortuitous cancellation of error.

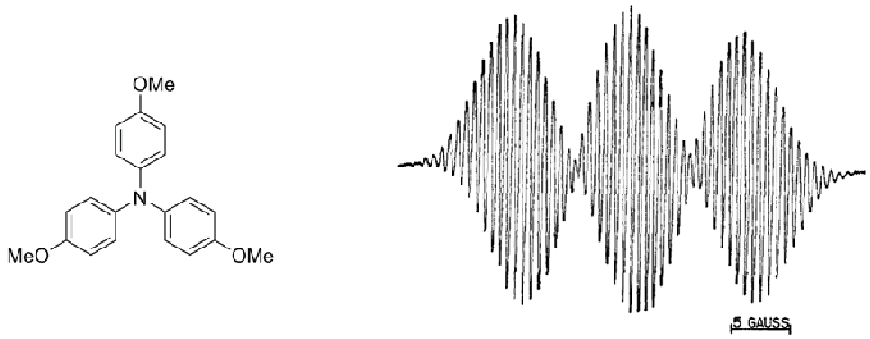

Figure 2.6 Structure of TAA and ESR spectrum for its monocation[11]

Table 2.2 Effect of basis set[a] on the hyperfine coupling constants (G) for TAA^+

Atom	Exp[b]	6-31G(d,p)	EPR-II		EPR-III	
		6*d*	5*d*	6*d*	5*d*	6*d*
N	8.97	7.45	6.38	6.49	6.47	6.51
H(ortho)	–1.76	–1.73	–1.70	–1.70	–1.66	–1.66
H(meta)	0.61	0.60	0.60	0.60	0.62	0.62
H(methyl)	0.65	1.02	1.08	1.08	1.06	1.06

[a] Computed at the DFT/B3LYP level. The geometry was optimized at the same level with the 6-31G(d,p) basis set. [b] From Refs. 11 and 12.

Also shown in Table 2.2 are the a_X values obtained with two types of *d* shells. The default for the Barone basis sets is five "pure" *d* functions in the Gaussian package,[13] whereas that for the Pople basis sets is six "Cartesian" *d* functions. A recent study of the hyperfine coupling constant for the ground state of the nitrogen atom found better agreement with experiment when six *d* functions were employed, no matter the size of the basis set.[14] We find the same trend for TAA^+. The improvement on adding a *d* function is, however, not enough to compensate for the small a_N value given by the EPR basis sets. In calculations hereafter, we use the 6-31G(d,p) basis with the default number of *d* functions.

2.4.2 Effect of Electron Correlation

One might also expect hyperfine coupling constants to be dependent on the level of theory at which they are computed. A recent study of the radical cations of a variety of amino derivatives found this indeed to be the case.[15] We focus on the trimethylamine (TMA) monocation in what follows. The hyperfine coupling constants were calculated using the configuration interaction (CI) and coupled cluster (CC) schemes including all single and double excitations: namely, CISD and CCSD. As shown in Table 2.3, including more electron correlation by going from CISD to CCSD gave better agreement with experiment. Then again, these *ab initio* correlated methods can only be applied to rather small systems; they are much too costly for the compounds studied here.

Table 2.3 Effect of electron correlation[a,b] on the hyperfine coupling constants (G) for TMA^+

Atom	Exp[c]	CISD	CCSD	DFT	
				B3LYP	BHandHLYP
N	20.55	23.17	19.82	15.51	22.47
H	28.56	26.33	26.76	30.55	29.16

[a] From Ref. 15. [b] Using the EPR-III basis set with five *d* functions. The geometry was optimized at the DFT/B3LYP level with the 6-311G(d) basis set. [c] From Ref. 16.

That brings us to density functional theory. In the same study, it was found that the percentage of Hartree-Fock (HF) exchange in the DFT functional affects the hyperfine coupling constant; the larger this percentage, the larger the value of a_N.[15] This is due to the balance of two opposing trends: the unrestricted HF method always overestimates spin polarization, whereas most DFT functionals underestimate this contribution. Hybrid functionals can thus provide accurate coupling constants. While it may appear from Table 2.3 that the BHandHLYP functional, which includes 50% of HF

exchange, outperforms B3LYP, which includes 20%, recall that the EPR-III basis set always underestimates the hyperfine splitting due to nitrogen. Indeed, another study found that the B3LYP functional gave better agreement (a_N = 18.4 G) when combined with the smaller 6-31G(d) basis set.[14] The DFT results are thus competitive with those obtained by more expensive post-HF methods. In calculations hereafter, we use the DFT/B3LYP level of theory to optimize the geometry and compute the hyperfine coupling. No separate electronic structure calculation is needed.

2.5 Simulation of Electron Spin Resonance Spectra

In the previous section, we saw that one can calculate hyperfine coupling constants, and thereby assign an observed a_X value to a specific nucleus in the radical. An electronic structure calculation cannot replace an ESR experiment, however, because it cannot predict the width of the hyperfine lines. This line width, ΔB, is due to the energy-time uncertainty principle. Instead, one typically simulates an ESR spectrum, and takes as a_X those values needed to give the best fit to experiment. In what follows, we discuss two types of simulation: dynamic, where the spin is allowed to exchange from one localized site to another, and static, where the spin stays put.

2.5.1 Static Simulation

We begin with the static case. To simulate an ESR spectrum, one must provide the computer program – here, the WinSIM program[17] – with the values of the coupling constants and the width of the hyperfine lines. In many cases, coupling constants too small to resolve from experiment are incorporated into ΔB. The effect of the line width on the shape of an ESR spectrum is illustrated in Figure 2.7 for a hypothetical class-III mixed-valence triarylamine. In this example, the hyperfine interactions due to the ^{1}H

nuclei are included in ΔB. We will find that most of the ESR spectra for two-center triarylamines tend toward the shape on the right.

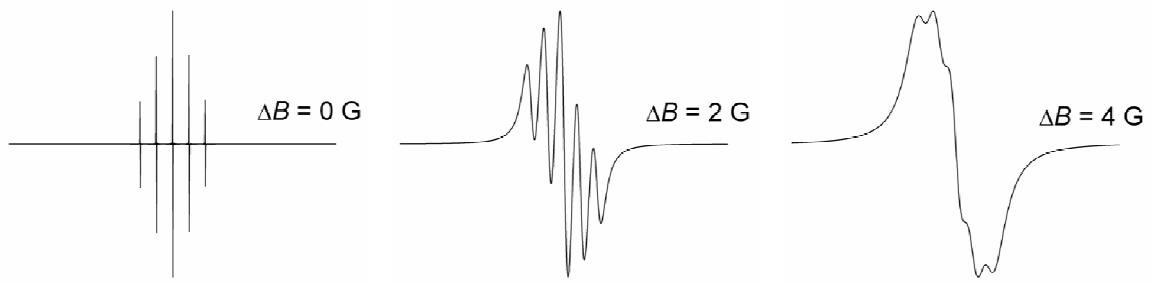

Figure 2.7 Effect of line width, ΔB, on the shape of a simulated ESR spectrum for a two-center class-III mixed-valence triarylamine with a(2N) = 4 G

2.5.2 Dynamic Simulation

Our goal, again, is to use ESR spectroscopy to measure the thermal electron transfer rates in class-II mixed-valence compounds. In ESR terminology, this process corresponds to an exchange of hyperfine coupling constants. If the rate of this exchange is slow on the ESR timescale – that is, if $k_{ET} < 10^8$ s^{-1} – the a_X values can be distinguished. If k_{ET} is fast on the ESR timescale, the spectrum will exhibit an averaged value of the coupling constants. If, however, the electron transfer rate is comparable to the ESR timescale, "anomalous" hyperfine patterns can be observed. To simulate such a spectrum, one needs a program that can compute ESR line shapes subject to intramolecular exchange. Such a program was developed by Heinzer.[18–19] We employ his "ESR-EXN" program below to simulate the exchange-broadened spectrum of a localized two-center triarylamine.

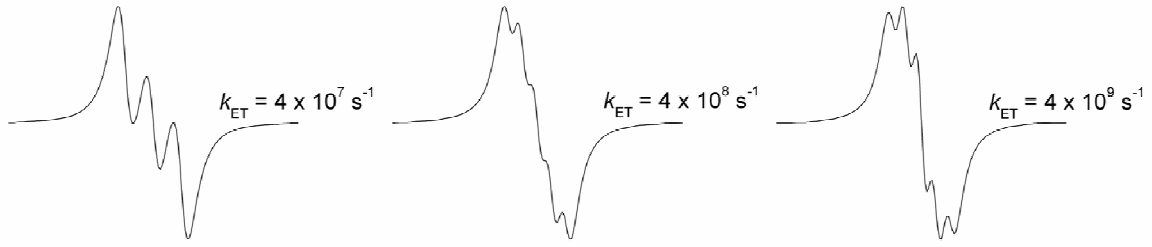

Figure 2.8 Effect of exchange rate, k_{ET}, on the shape of a simulated ESR spectrum for a two-center class-II mixed-valence triarylamine with a(1N) = 8 G and ΔB = 4 G

In addition to the input required for a static simulation, one must also provide the exchange rate in a dynamic simulation. When this rate is small, we can expect a three-line ESR spectrum like that shown in Figure 2.8. This shape is due to interaction of the unpaired electron with only one triarylamine center on the ESR timescale. When k_{ET} is large, we see a five-line ESR spectrum in which the second peak is higher than the first. This shape is identical to that of the delocalized case in the section above. When the exchange rate is comparable to the ESR timescale, we see an anomalous hyperfine pattern – a five-line spectrum in which the first peak is higher than the second. We shall see in chapters to follow that this signature means that the shape of the ESR spectrum is sensitive to temperature.

2.6 Electron Transfer in Mixed-Valence Triarylamines

In the previous chapter, we saw that two-center triarylamines are often used as hole-transport layers in organic electronic devices due to the stability of the monocations and the high mobility in the films. The mechanism of hole transport involves a series of *inter*molecular electron hops whereby a neutral compound transfers an electron to a neighboring mixed-valence monocation. In what follows, we will see how ESR

spectroscopy was used to study both this reaction and the *intra*molecular electron transfer reaction that occurs within the monocation.

2.6.1 Intermolecular Electron Transfer

Not many ESR reports of intermolecular electron transfer in two-center triarylamines exist. One of the few, if not the only, was done on TPD, the structure of which is shown in Figure 2.9.[20] In this study, TPD^+ monocation was generated by chemical oxidation of TPD. At low concentrations of TPD, the ESR spectrum showed a five-line pattern indicative of coupling to two equivalent nitrogen atoms. The unpaired electron thus appears delocalized over both redox centers on the ESR timescale. At higher concentration of TPD, however, the ESR spectrum showed a single line of Lorentzian shape. The line narrowing was attributed to an electron exchange between neutral TPD and its monocation.

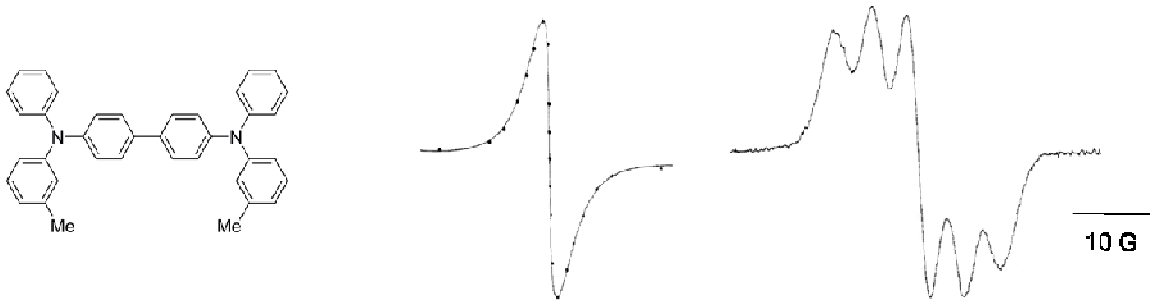

Figure 2.9 Structure of TPD and room temperature ESR spectra of its monocation at high (left) and low (right) concentration[20]

One may wonder what the import of such a study is to *intra*molecular electron transfer in mixed-valence triarylamines. When one performs an ESR study on a mixed-valence compound in solution, there is always the possibility that an intermolecular exchange occurs along with an intramolecular exchange. This study showed that the ESR

spectrum narrows when intermolecular electron transfer is significant. For the ESR studies hereafter, the concentration of monocation is optimized in order to prevent such loss of hyperfine coupling.

2.6.2 Intramolecular Electron Transfer

In order to extract rate data from an ESR study, the thermal electron transfer must occur on the ESR timescale. This places an upper limit of approximately 10^9 s^{-1} on the rates that can be measured, which, in turn, requires that the redox centers be only weakly coupled. The intensity of an intervalence band, however, increases with the square of V, and the coupling must be large enough to detect the optical transition. These two constraints are at odds with one another, which limits the number of mixed-valence compounds that can yield both measurable rates of thermal electron transfer and observable intervalence bands. We discuss two illustrative cases next.

2.6.2.1 Case of Intense Intervalence Band, Thermal Electron Transfer Too Fast

In the first chapter, we saw that the mixed-valence monocation of **3** shows an intervalence band that is both intense and well-separated from other bands.[21–22] $\mathbf{3}^+$ was assigned as a localized class-II compound due to the characteristics of this band. The room temperature ESR spectrum of $\mathbf{3}^+$ in Figure 2.10, however, shows a five-line pattern indicative of coupling to two equivalent nitrogen atoms.[23] The unpaired electron thus appears delocalized over both redox centers on the ESR timescale. What is more, the shape of the spectrum persists for temperatures as low as 180 K.[24] This is just one example of the many class-II mixed-valence triarylamines for which the thermal electron transfer is too fast to observe on the ESR timescale.

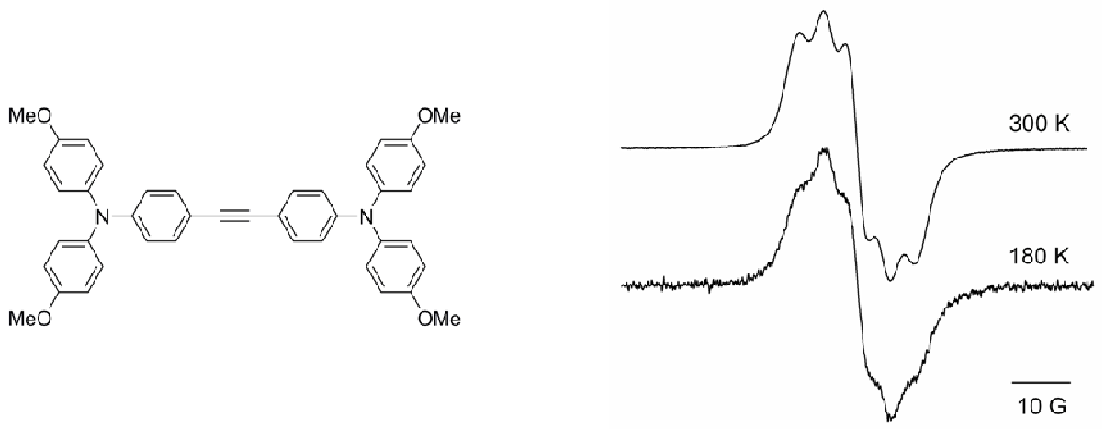

Figure 2.10 Structure of **3** and ESR spectra of its monocation at high and low temperature[24]

2.6.2.2 Case of No Intervalence Band, Thermal Electron Transfer Just Right

At the time of writing, the only ESR study of thermal electron transfer rates in mixed-valence triarylamines was done on the spiro-fused compound in Figure 2.11.[25] In this example, the triarylamine redox centers are linked perpendicularly to one another. Much like for $\mathbf{3}^+$, the room temperature ESR spectrum of $\mathbf{9}^+$ showed a five-line pattern indicative of coupling to two equivalent nitrogen atoms. As shown in Figure 2.11, however, the shape of the spectra changed with temperature. This indicated that the five-line pattern at high temperature is induced by thermal electron transfer between the two redox centers, and is not due to delocalization of the unpaired electron.

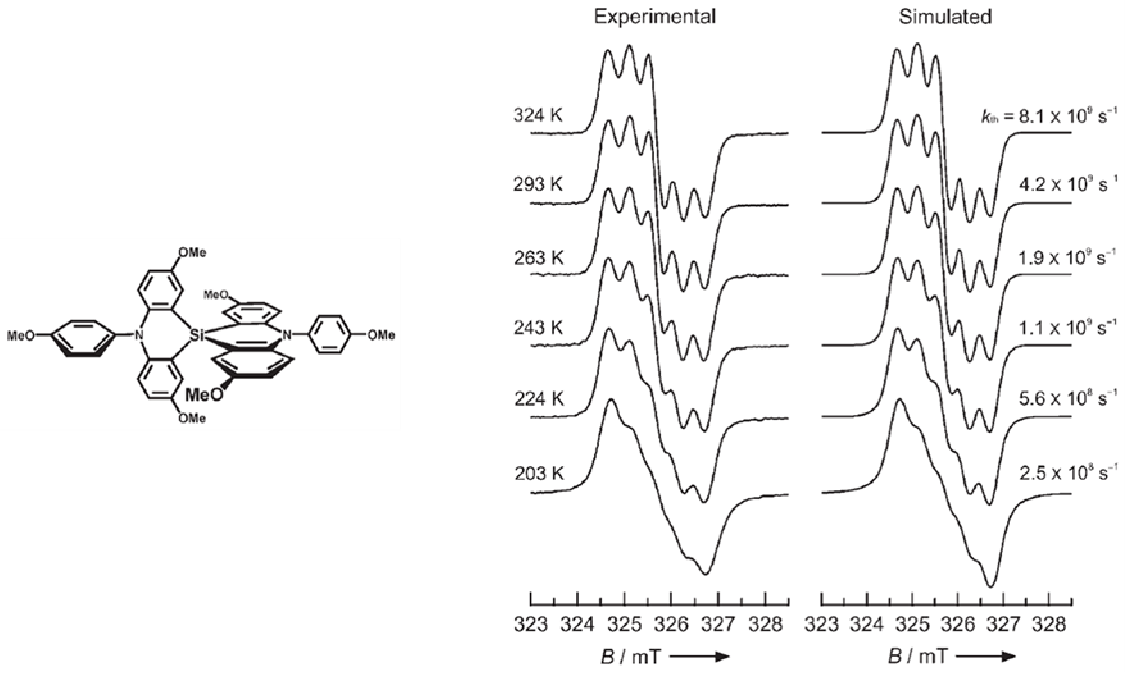

Figure 2.11 Structure of **9** and variable-temperature ESR spectra of its monocation[25]

The thermal electron transfer rates were determined by simulation of the ESR spectra using the ESR-EXN program. An Arrhenius plot gave a linear relationship between $\ln(k_{ET})$ and $1/T$, from which the prefactor, A, and activation barrier, ΔG^*, were estimated. The parameters are given in Table 2.4. The electron transfer was assumed to take place nonadiabatically due to the orthogonality of the redox centers.

Table 2.4 Thermal electron transfer parameters for $\mathbf{9}^+$ from an Arrhenius plot[a]

Compound	A (s^{-1})	ΔG^* (cm^{-1})	k_{ET} (s^{-1})[b]	Nature
9	2.7×10^{12}	1300	4.2×10^{9}	Nonadiabatic

[a] From rates reported in Ref. 25. [b] At T = 293 K.

As a corollary, however, no intervalence band was found in the optical spectrum of $\mathbf{9}^+$. The absence of an intervalence band was attributed to the weak coupling between redox centers. Thus, while the magnitude of V allowed measurement of the thermal

electron transfer rate by means of ESR spectroscopy, it prevented the observation of optical electron transfer.

From the two cases considered here, it is clear that it is quite rare to find compounds that allow for comparison of optical and thermal intramolecular transfer. It is also clear that such compounds are needed to provide a test of electron transfer theory. In particular, a comparison of the two pathways could quantify the error introduced in the Hush equations by taking the diabatic electron transfer distance, *R*, as the N–N distance. *The central aim of this thesis is to correlate thermal and optical electron transfer in mixed-valence triarylamines*.

REFERENCES

[1] Marcus, R. A. *J. Chem. Phys.* **1956**, *24*, 966.

[2] Marcus, R. A. *Disc. Faraday Soc.* **1960**, *29*, 21.

[3] Marcus, R. A. *Annu. Rev. Phys. Chem.* **1964**, *15*, 155.

[4] Marcus, R. A.; Sutin N. *Biochim. Biophys. Acta* **1985**, *811*, 265.

[5] Hush, N. S. *Prog. Inorg. Chem.* **1967**, *8*, 391.

[6] Hush, N. S. *Coord. Chem. Rev.* **1985**, *64*, 135.

[7] Sutin, N. *Prog. Inorg. Chem.* **1983**, *30*, 441.

[8] Barone, V. in *Recent Advances in Density Functional Methods* (Part I), edited by D. P. Chong (World Scientific, Singapore, **1995**), p. 287.

[9] Rega, N.; Cossi, M.; Barone, V. *J. Chem. Phys.* **1996**, *105*, 11060.

[10] Hariharan, P. C.; Pople, J. A. *Theor. Chim. Acta* **1973**, *28*, 213.

[11] Seo, E. T.; Nelson, R. F.; Fritsch, J. M.; Marcoux, L. S.; Leedy, D. W.; Adams, R. N. *J. Am. Chem. Soc.* **1966**, *88*, 3498.

[12] Linkletter, S. J. G.; Pearson, G. A.; Walter, R. I. *J. Am. Chem. Soc.* **1977**, *99*, 5269.

[13] Frisch, M. J.; Trucks, G. W.; Schlegel, H. B.; Scuseria, G. E.; Robb, M. A.; Cheeseman, J. R.; J. A. Montgomery, J.; Vreven, T.; Kudin, K. N.; Burant, J. C.; Millam, J. M.; Iyengar, S. S.; Tomasi, J.; Barone, V.; Mennucci, B.; Cossi, M.; Scalmani, G.; Rega, N.; Petersson, G. A.; Nakatsuji, H.; Hada, M.; Ehara, M.; Toyota, K.; Fukuda, R.; Hasegawa, J.; Ishida, M.; Nakajima, T.; Honda, Y.; Kitao, O.; Nakai, H.; Klene, M.; Li, X.; Knox, J. E.; Hratchian, H. P.; Cross, J. B.; Adamo, C.; Jaramillo, J.; Gomperts, R.; Stratmann, R. E.; Yazyev, O.; Austin, A. J.; Cammi, R.; Pomelli, C.; Ochterski, J. W.; Ayala, P. Y.; Morokuma, K.; Voth, G. A.;

Salvador, P.; Dannenberg, J. J.; Zakrzewski, V. G.; Dapprich, S.; Daniels, A. D.; Strain, M. C.; Farkas, O.; Malick, D. K.; Rabuck, A. D.; Raghavachari, K.; Foresman, J. B.; Ortiz, J. V.; Cui, Q.; Baboul, A. G.; Clifford, S.; Cioslowski, J.; Stefanov, B. B.; Liu, G.; Liashenko, A.; Piskorz, P.; Komaromi, I.; Martin, R. L.; Fox, D. J.; Keith, T.; Al-Laham, M. A.; Peng, C. Y.; Nanayakkara, A.; Challacombe, M.; Gill, P. M. W.; Johnson, B.; Chen, W.; Wong, M. W.; Gonzalez, C.; Pople, J. A. *Gaussian 03, Revision B.02*, Gaussian, Inc.: Pittsburgh PA, **2003**.

[14] Hermosilla, L.; Calle, P.; García de la Vega, J. M.; Sieiro, C. *J. Phys. Chem. A* **2006**, *110*, 13600.

[15] Rogowska, A.; Kuhl, S.; Schneider, R.; Walcarius, A.; Champagne, B. *Phys. Chem. Chem. Phys.* **2007**, *9*, 828.

[16] Fessenden, R. W.; Neta, P. *J. Phys. Chem.* **1972**, *76*, 2857.

[17] Duling, D. R. *J. Magn. Reson. Ser. B* **1994**, *104*, 105.

[18] Heinzer, J. *Mol. Phys.* **1971**, *22*, 167.

[19] Heinzer, J. Quantum Chemistry Program Exchange, *No. 209*, **1972**.

[20] Veregin, R. P.; Harbour, J. R. *J. Phys. Chem.* **1990**, *94*, 6231.

[21] Lambert, C.; Nöll, G. *Angew. Chem. Int. Ed.* **1998**, *37*, 2107.

[22] Lambert, C.; Nöll, G. *J. Am. Chem. Soc.* **1999**, *121*, 8434.

[23] Barlow, S.; Risko, C.; Coropceanu, V.; Tucker, N. M.; Jones, S. C.; Levi, Z.; Khrustalev, V. N.; Antipin, M. Y.; Kinnibrugh, T. L.; Timofeeva, T.; Marder, S. R.; Brédas, J.-L. *Chem. Commun.* **2005**, 764.

[24] Lancaster, K.; Odom, S. A.; Jones, S. C.; Thayumanavan, S.; Marder, S. R.; Brédas, J.-L.; Coropceanu, V.; Barlow, S. *J. Am. Chem. Soc.* **2009**, *131*, 1717.

[25] Hirao, Y.; Urabe, M.; Ito, A.; Tanaka, K. *Angew. Chem. Int. Ed.* **2007**, *46*, 3300.

CHAPTER 3

INTRAMOLECULAR ELECTRON TRANSFER IN TWO-CENTER CLASS-III MIXED-VALENCE TRIARYLAMINES

3.1 Two-Center Class-III Triarylamines

In a localized mixed-valence compound with two redox centers – that is, one which belongs to Robin and Day's class-II – the intervalence band is related to electron transfer from one redox center to the other.[1] This terminology is also commonly applied to class-III compounds, since the adiabatic states involved can be considered as arising from the same diabatic surfaces. In both cases, one can estimate the interaction between centers from a Hush analysis of the intervalence band.[2] Here we examine the effect of bridge energy on the electronic coupling in delocalized mixed-valence compounds.

In the first chapter, we saw that adding electron donating groups to a phenylene bridge can increase the electronic coupling in class-II triarylamines. A similar effect is seen when benzene is replaced by the less aromatic and more easily oxidized anthracene; i.e., *V* increases on going from **A** to **B** in Figure 3.1.[3,4] In contrast, the same substitution in a class-III triarylamine (**C** vs. **D**) leads to a decrease in the electronic coupling.[5] This result can be attributed to the increased steric hindrance due to the anthracene moiety, which leads to less overlap between amine- and bridge-based orbitals. It is of interest then to study class-III compounds in which the effect of bridge energy is not masked by steric interactions.

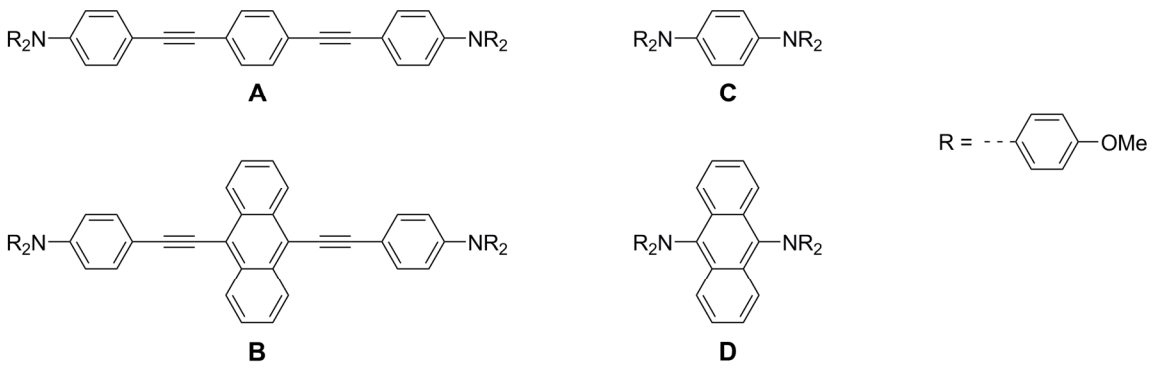

Figure 3.1 Examples of two-center triarylamines with different bridge energies

Here we investigate the extent to which the lower ionization potential of thiophene vs. benzene – 8.9 eV[6] vs. 9.24 eV[7] as measured by photoelectron spectroscopy – can lead to more effective mediation of coupling between two triarylamine redox centers. In particular, we study the class-III cations of the two-center triarylamines in Figure 3.2, where the effects of bridge energy and steric interaction work in concert, rather than in opposition. We show that Hush analyses of the intervalence bands for $\mathbf{1}^+$–$\mathbf{4}^+$ give electronic coupling values larger than those in phenylene-bridged analogues $\mathbf{I}^+$–$\mathbf{II}^+$. The ESR spectra show well-resolved hyperfine coupling, which, in combination with DFT calculations, give insight into the spin distribution and indicate that the increased electronic coupling in the thiophene-based compounds is accompanied by increased bridge character to the oxidation.

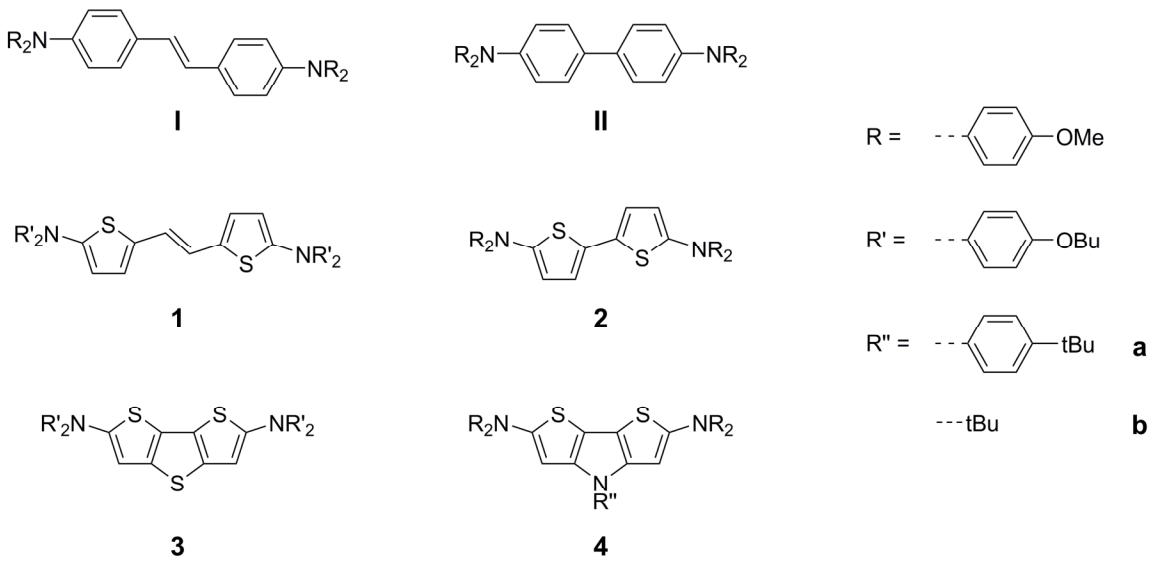

Figure 3.2 Structure of compounds **I–II** and **1–4**

3.2 Electronic Spectra of the Neutral Compounds

The UV-visible absorption spectra of compounds **1–4** in dichloromethane are shown in Figure 3.3. Data for the lowest-energy transitions are collected in Table 3.1, along with that previously reported for **I**.[8] Transition dipole moments, μ_{ge}, were obtained from integration of the spectra. Also included in the table are the absorption maxima and transition dipole moments computed using time-dependent DFT; all calculations were done with butyl groups replaced by methyl groups.

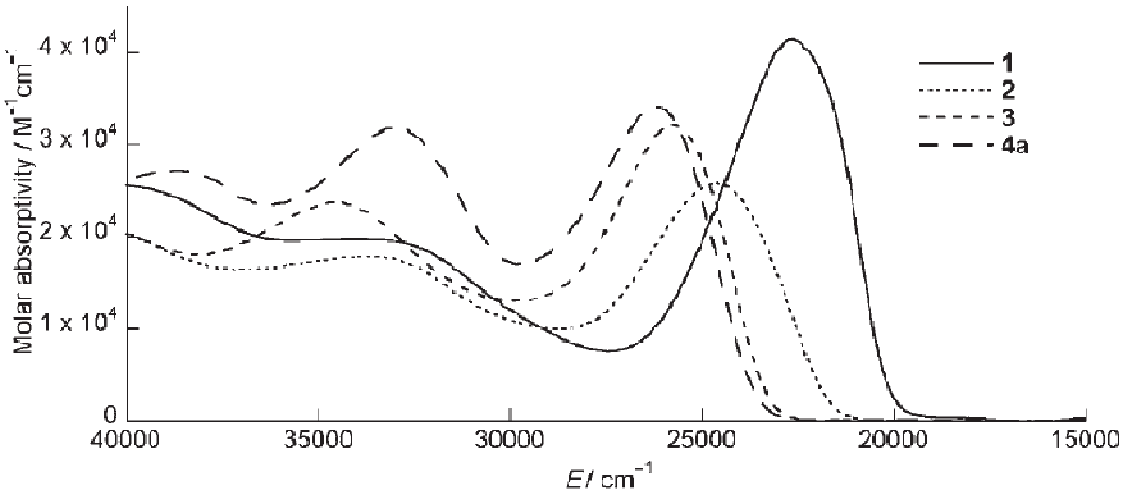

Figure 3.3 UV-visible absorption spectra for **1**–**4** in dichloromethane[9]

The time-dependent DFT calculations show that the lowest-energy transition for each compound is predominately a HOMO to LUMO excitation. The molecular orbitals involved in the transition are shown in Figure 3.4, along with the HOMO–1, which plays a role in the electronic spectra of the monocations. In each case, the HOMO and HOMO–1 are of opposite parity and can be regarded as in- or out-of-phase linear combinations of two amine-based orbitals. The highest-occupied orbital for each compound has significant contributions from the local HOMO of the bridge, while the LUMO is almost entirely bridge-based.

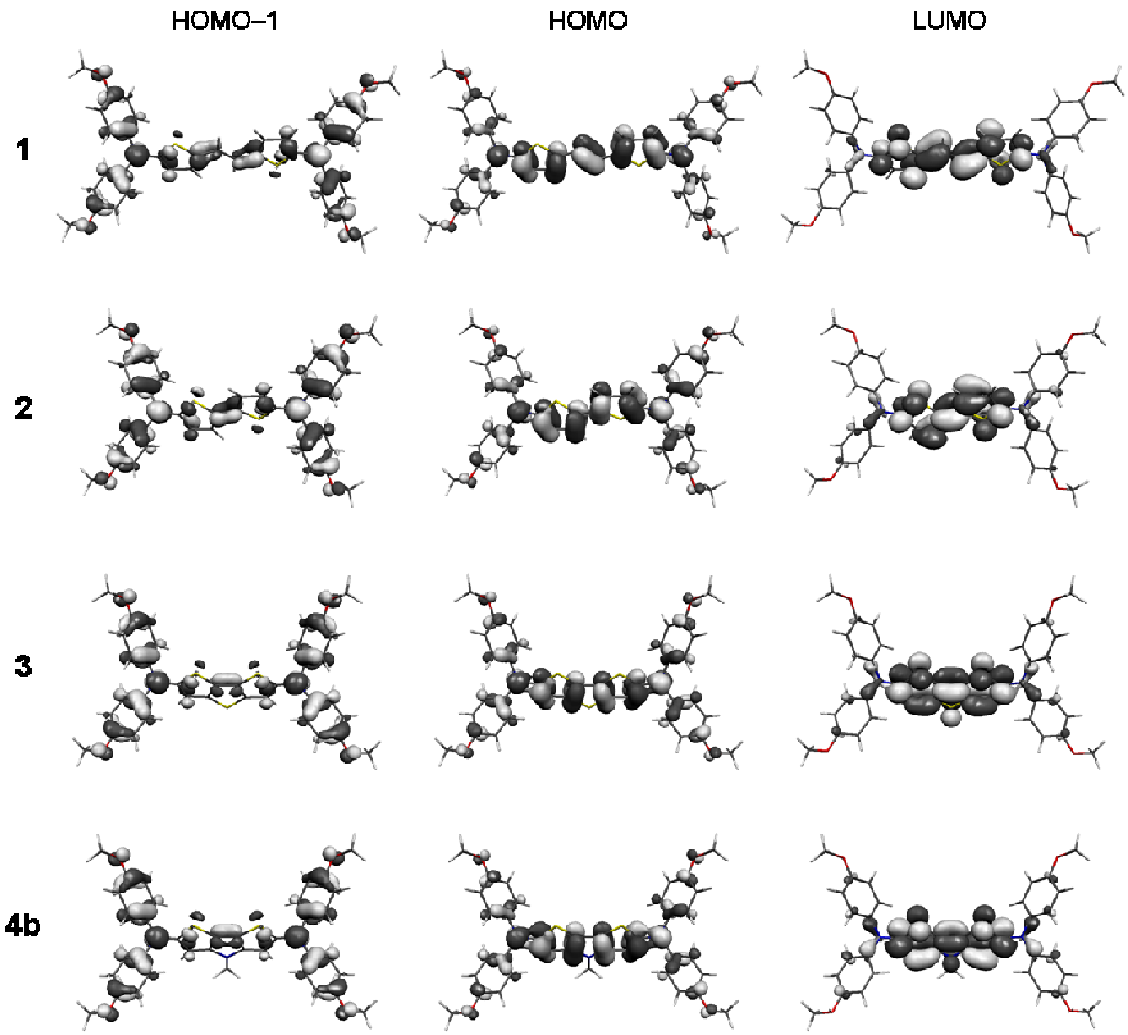

Figure 3.4 Frontier orbitals for **1**–**4** according to DFT calculation

The calculated absorption maxima compare well with those from experiment, although they are systematically underestimated by about 2000 cm^{-1}. The lowest-energy transition is seen for **1**, consistent with its extended conjugation. Compounds **3**–**4** show very similar absorptions, which occur at higher energy than that of **2**; this blue-shift is partly attributable to the destabilizing effect of the central heteroatoms on the LUMOs of **3**–**4**. Both theory and experiment show larger transition dipole moments for the

compounds with longer bridges, consistent with polarization of the transition along the long axis between the two amine groups.

Table 3.1 Data for the lowest-energy absorptions of neutral compounds **I** and **1–4** in dichloromethane with DFT gas phase values[a] in italics

Compound	ν_{max} (cm^{-1})		μ_{ge} (D)	
I[b]	25100	*23200*	10.0	*12.6*
1	22600	*20700*	8.58	*12.3*
2	24600	*22600*	6.57	*9.49*
3	25800	*23800*	7.31	*9.11*
4a	26200	*24300*	7.62	*8.64*

[a] Computed with time-dependent DFT at the B3LYP/6-31G(d,p) level. [b] From Ref. 8.

3.3 Electrochemistry

As shown in Figure 3.5, the cyclic voltammograms of compounds **1–4** show two reversible oxidations. The redox potentials of the thiophene-bridged compounds are given in Table 3.2 along with those for phenylene analogues **I–II**,[8,10] indicating the former to be more readily oxidized than the latter. The dithienopyrrole bridges result in the most electron-rich compounds, with the *N*-alkyl derivative **4b** slightly more electron-rich than its *N*-aryl analogue **4a**. That the compounds with pyrrole-based bridges are more readily oxidized than those based solely on thiophene is consistent with the lower ionization potential of pyrrole relative to thiophene (8.2 eV vs. 8.9 eV)[6].

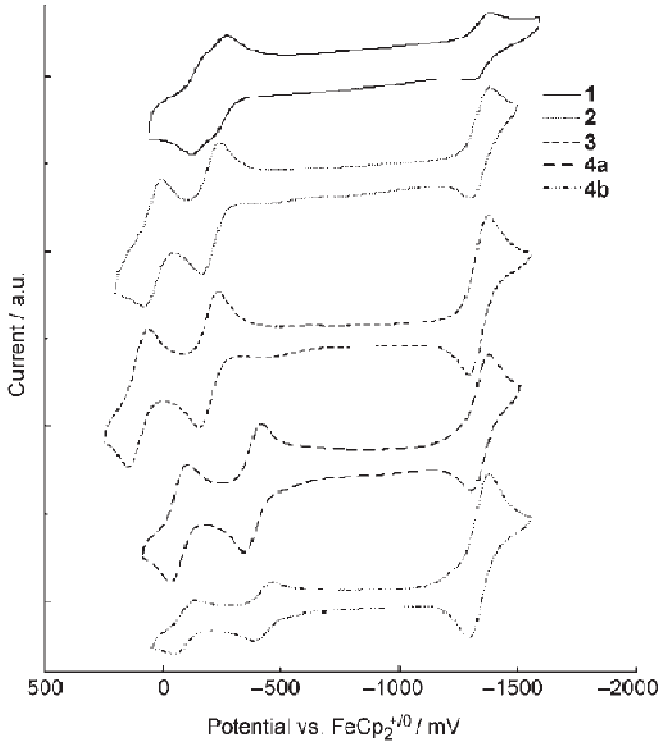

Figure 3.5 Cyclic voltammograms of **1**–**4** in 0.1 M $[Bu_4N]^+[PF_6]^-$ in dichloromethane,[9] shown with $Cp_2Co^{+/0}$ as the internal reference (–1320 mV vs. $Cp_2Fe^{+/0}$)

The separation between the first and second redox potentials, $\Delta E_{½}$, is often used as a measure of the electronic coupling in a mixed-valence compound;[10] this correlation must be used with caution, however, as other factors can also contribute to the splitting. Indeed, the values of $\Delta E_{½}$ in Table 3.2 show no clear correlation with the spectroscopic estimates of V given later in Table 3.8. It is worth noting, however, that the $\Delta E_{½}$ values for thiophene-based compounds **3**–**4** are rather large, indicating that the corresponding radical cations are relatively stable to disproportionation.

Table 3.2 Redox potentials (mV) of **I–II** and **1–4** from cyclic voltammetry

Compound	$E_{½}^{+/0}$	$E_{½}^{2+/+}$	$\Delta E_{½}$
I[a]	+80	+220	140
II[b]	+90	+310	220
1	–230	–140	90
2	–200	–40	160
3	–190	+130	320
4a	–400	–80	320
4b	–430	–100	330

[a] From Ref. 8. [b] From Ref. 10.

3.4 Electronic Spectra of the Monocations

The radical cations of **1–4** were generated in dichloromethane by chemical oxidation using tris(4-bromophenyl)aminium hexachloroantimonate. The byproduct of the electron transfer reaction, shown in Figure 3.6, is diamagnetic and shows no absorption in the visible-NIR region.[11] To minimize contributions to the electronic spectra from dications arising from disproportionation, an excess of the neutral diamine was added to the oxidizing agent.

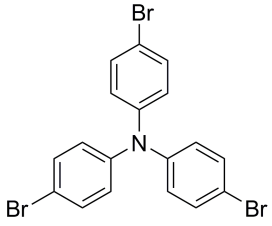

Figure 3.6 Structure of tris(4-bromophenyl)amine

The visible-NIR absorption spectra of the monocations are shown in Figure 3.7, with the exception of that of **4b**$^+$, which is essentially identical to that of **4a**$^+$. The insensitivity of the spectra to the substituent on the pyrrole nitrogen is consistent with the lack of contribution of this substituent to the relevant orbitals in Figure 3.4. Molar

absorptivities were calculated assuming complete electron transfer to the oxidizing agent. The onsets of strong absorption at high energy correspond to absorption by the excess neutral diamines present; the absorptivity scale applies only to the lower energy absorptions attributable to the radical cations.

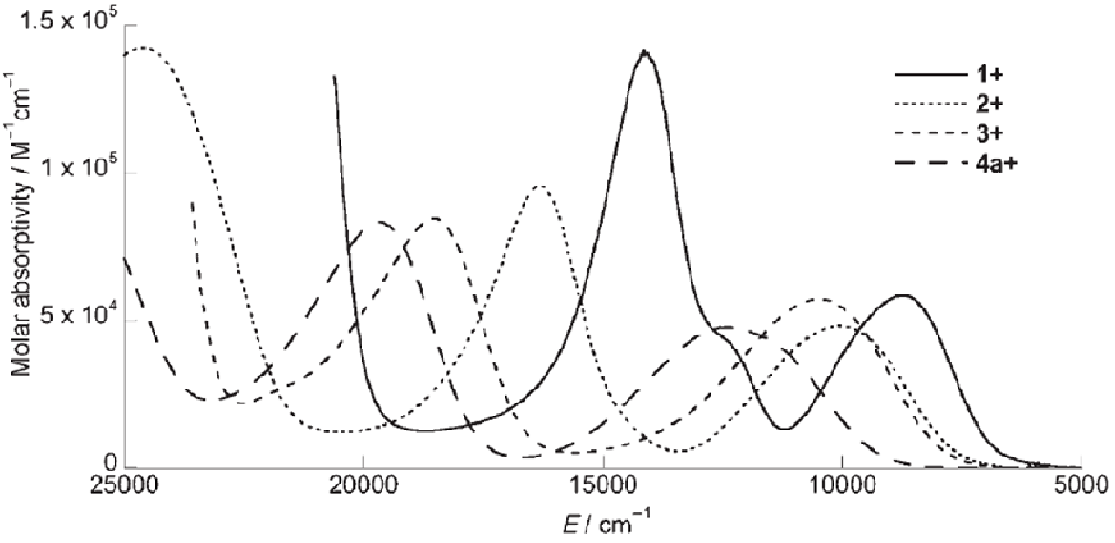

Figure 3.7 Visible-NIR absorption spectra for monocations $\mathbf{1}^+$–$\mathbf{4}^+$ in dichloromethane[9]

Cations $\mathbf{1}^+$–$\mathbf{4}^+$ show intense absorption bands in the near-IR region; as seen in Table 3.3, these are similar in terms of energy and lineshape to those observed for other strongly coupled mixed-valence triarylamines. In particular, the observed bandwidths at half-height, $\nu_{½[obs]}$, are narrower than the width predicted for class-II compounds using the Hush equation:[2]

$$\nu_{½[\mathrm{Hush}]} = \sqrt{(2310 \times \nu_{\max})} \qquad 3.1$$

where both $\nu_{½[\mathrm{Hush}]}$ and $\nu_{\max}$ are in cm^{-1}. For $\mathbf{1}^+$–$\mathbf{3}^+$, the bands are also asymmetric; the asymmetry is quantified in Table 3.3 by the ratio $\nu_{½[high]}/\nu_{½[low]}$, where $\nu_{½[high]}$ and $\nu_{½[low]}$

are defined as twice the bandwidths on the high- and low-energy sides of the absorption band, respectively. These spectral characteristics were originally interpreted in terms of a cut-off on the low-energy side of the band due to thermal population of the electron transfer barrier top;[10,12] according to this model, any compound belonging to class-II but lying close to the class-III borderline will exhibit such lineshapes. We saw in Chapter 1, however, that such lineshapes can also arise from coupling of the electron transfer in class-III compounds to symmetric, two-center vibrations.[13,14] Recent experimental data support the latter of the two interpretations.[15–18] Thus, the characteristics of the low-energy near-IR absorptions support the assignment of $\mathbf{1}^+$–$\mathbf{4}^+$ to class-III.

Table 3.3 Parameters from the intervalence bands for $\mathbf{I}^+$–$\mathbf{II}^+$ and $\mathbf{1}^+$–$\mathbf{4}^+$

Compound	ν_{max} (cm^{-1})	$\nu_{½[obs]}$ (cm^{-1})	$\nu_{½[Hush]}$[a] (cm^{-1})	$\nu_{½[high]}/\nu_{½[low]}$[b]
$\mathbf{I}^+$[c]	6080	2760	3750	1.40
$\mathbf{II}^+$[d]	6360	3170	3830	1.45
$\mathbf{1}^+$	8750	2720	4500	1.37
$\mathbf{2}^+$	10100	3340	4830	1.17
$\mathbf{3}^+$	10500	3640	4920	1.34
$\mathbf{4a}^+$	12500	4260	5370	0.95

[a] Calculated using Eq. 3.1. [b] Ratio of bandwidth on high-energy side to that on low-energy side. [c] From Ref. 8. [d] From Ref. 10.

While conventional DFT is known to over-delocalize an unpaired electron and is, therefore, unsuitable for modeling class-II compounds, it gives good agreement with structural and spectroscopic features when applied to compounds shown experimentally to belong to class-III.[16–18] The spin-unrestricted DFT results in Table 3.4 show that **1**–**4** and **I**–**II** undergo similar geometric changes upon oxidation. Namely, the N–C_{bridge} bonds contract, the N–C_{aryl} bonds lengthen, the bridge bond-length pattern shifts towards, but not fully to, a semi-quinoidal limit, the nonplanar bridges (those of **1**–**2** and **I**–**II**)

planarize, and the angle between the planes defined by the bridging groups and by the N–C_{aryl} bonds decreases. The last change is more dramatic in the thiophene-bridged compounds and gives a smaller final angle, which could lead to better overlap between the amine- and bridge-based orbitals.

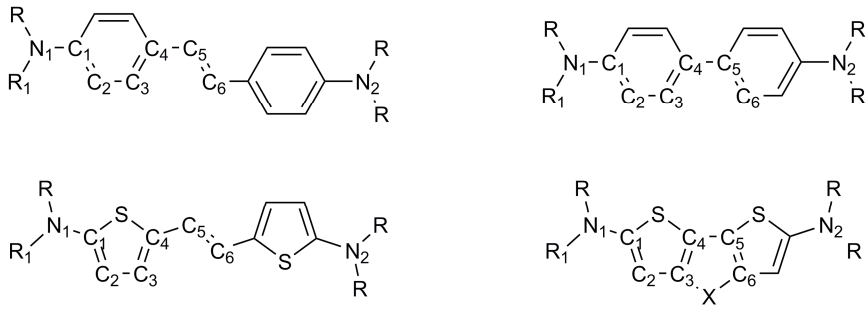

Figure 3.8 Labeling scheme used in Table 3.4

Table 3.4 DFT-computed bond lengths (Å) and dihedral angles for **I**–**II** and **1**–**4** in their neutral and radical cation states[a]

	I	**I**$^+$	Δ	**1**	**1**$^+$	Δ
N_1–N_2	12.347	12.256	*–0.091*	11.626	11.508	*–0.118*
R_1–N_1	1.425	1.429	*0.004*	1.427	1.438	*0.011*
N_1–C_1	1.412	1.388	*–0.024*	1.394	1.360	*–0.034*
C_1–C_2	1.409	1.421	*0.012*	1.379	1.407	*0.028*
C_2–C_3	1.386	1.377	*–0.009*	1.416	1.389	*–0.027*
C_3–C_4	1.410	1.420	*0.010*	1.382	1.406	*0.024*
C_4–C_5	1.461	1.436	*–0.025*	1.444	1.409	*–0.035*
C_5–C_6	1.351	1.370	*0.019*	1.357	1.386	*0.029*
R_1–N_1–C_1–C_2	33.9	26.3	*–7.6*	40.9	16.9	*–24.0*
C_3–C_4–C_5–C_6	2.0	1.5	*–0.5*	6.2	2.5	*–3.7*
	II	**II**$^+$	Δ	**2**	**2**$^+$	Δ
N_1–N_2	10.006	9.951	*–0.055*	9.155	9.058	*–0.097*
R_1–N_1	1.424	1.426	*0.002*	1.427	1.438	*0.011*
N_1–C_1	1.414	1.393	*–0.021*	1.394	1.359	*–0.035*
C_1–C_2	1.406	1.416	*0.010*	1.375	1.404	*0.029*
C_2–C_3	1.390	1.380	*–0.010*	1.420	1.391	*–0.029*
C_3–C_4	1.406	1.416	*0.010*	1.378	1.402	*0.024*
C_4–C_5	1.480	1.459	*–0.021*	1.446	1.410	*–0.036*
R_1–N_1–C_1–C_2	34.4	28.2	*–6.2*	42.6	17.3	*–25.3*
C_3–C_4–C_5–C_6	34.3	24.3	*–10.0*	12.7	0.0	*–12.7*

	3	**3**$^+$	Δ	**4b**	**4b**$^+$	Δ
N_1–N_2	9.136	9.031	*–0.105*	9.145	9.027	*–0.118*
R_1–N_1	1.428	1.437	*0.009*	1.426	1.438	*0.012*
N_1–C_1	1.393	1.360	*–0.033*	1.396	1.361	*–0.035*
C_1–C_2	1.375	1.402	*0.027*	1.376	1.402	*0.026*
C_2–C_3	1.420	1.394	*–0.026*	1.420	1.396	*–0.024*
C_3–C_4	1.393	1.415	*0.022*	1.403	1.426	*0.023*
C_4–C_5	1.419	1.391	*–0.028*	1.413	1.385	*–0.028*
R_1–N_1–C_1–C_2	47.0	18.3	*–28.7*	51.9	17.6	*–34.3*

[a] Computed at the B3LYP/6-31G(d,p) level.

The characteristics of the lowest-energy absorptions for the radical cations computed using time-dependent DFT are collected in Table 3.5. The calculated absorption maxima compare well with those from experiment. Although the differences are smaller than in the case for the corresponding neutral compounds, they are no longer systematic – ν_{max} is slightly over-estimated for **1**$^+$, **I**$^+$ and **II**$^+$ and slightly under-estimated for **2**$^+$, **3**$^+$ and **4**$^+$. The variation in ν_{max} between compounds is, however, well reproduced. The agreement with DFT calculation, which assumes delocalization of the unpaired electron, further supports our assignment of the cations to class-III.

Table 3.5 Data for the lowest-energy absorptions of radical cations **I**$^+$–**II**$^+$ and **1**$^+$–**4**$^+$ in dichloromethane with DFT gas phase values[a] in italics

Compound	ν_{max} (cm^{-1})		μ_{ge} (D)	
I$^+$[b]	6080	*6990*	13.5	*15.7*
II$^+$[c]	6360	*6810*	11.6	*14.7*
1$^+$	8750	*9460*	13.0	*9.51*
2$^+$	10100	*9980*	12.3	*9.84*
3$^+$	10500	*10300*	14.0	*10.5*
4a$^+$	12500	*11600*	12.3	*9.76*

[a] Computed with time-dependent DFT at the B3LYP/6-31G(d,p) level. [b] From Ref. 8. [c] From Ref. 10.

The time-dependent DFT results in Table 3.6 show that the lowest-energy transition of the radical cations is, in the nomenclature of the neutral compounds, HOMO–1 to HOMO in nature, with some contribution from HOMO to LUMO excitation. Thus, the transition is between combinations of amine-based orbitals with opposite parity. This orbital picture closely resembles that previously reported for other delocalized two-center triarylamines.[13,14,16,17]

Table 3.6 Configuration description of the lowest excited state[a]

Compound	Configuration	Weight
$\mathbf{I}^+$	HOMO–1 → HOMO	0.81
	HOMO → LUMO	0.25
$\mathbf{II}^+$	HOMO–1 → HOMO	0.78
	HOMO → LUMO	0.18
$\mathbf{1}^+$	HOMO–1 → HOMO	0.89
	HOMO → LUMO	0.45
$\mathbf{2}^+$	HOMO–1 → HOMO	0.91
	HOMO → LUMO	0.32
$\mathbf{3}^+$	HOMO–1 → HOMO	0.92
	HOMO → LUMO	0.27
$\mathbf{4a}^+/\mathbf{4b}^+$	HOMO–1 → HOMO	0.93
	HOMO → LUMO	0.26

[a] Computed with TD-DFT at the B3LYP/6-31G(d,p) level

The DFT calculations also provide insight into the differences in experimentally observed band shapes. The relaxation energy (L) associated with the lowest excited state of the radical cations was estimated by the symmetry-constraint approach.[14] As shown in Table 3.7, the DFT relaxation energies follow the trend seen in the experimentally measured values of $\nu_{1/2[obs]}$. Thus, the increase in bandwidth on going from $\mathbf{3}^+$ to $\mathbf{4}^+$ could be related to a significant (about 600 cm^{-1}) increase in the corresponding relaxation energy. Large relaxation energies tend to result in Gaussian-like band shapes;[14] this is

consistent with the broader, more symmetric lineshape of the intervalence band of $\mathbf{4}^+$ relative to that of $\mathbf{3}^+$.

Table 3.7 DFT-computed relaxation energies[a] for $\mathbf{1}^+$–$\mathbf{4}^+$

Compound	$\nu_{1/2[obs]}$ (cm^{-1})	L (cm^{-1})
$\mathbf{1}^+$	2720	2830
$\mathbf{2}^+$	3340	3210
$\mathbf{3}^+$	3640	3330
$\mathbf{4a}^+/\mathbf{4b}^+$	4260	3880

[a] Computed at the B3LYP/6-31G(d,p) level.

3.5 Electronic Coupling

According to Hush theory,[2] the electronic coupling, V, between two redox centers in a mixed-valence compound can be obtained from the transition dipole moment, μ_{ge}, and the absorption maximum, ν_{max}, of the intervalence band:

$$V = \frac{\mu_{ge}\nu_{max}}{eR} \qquad 3.2$$

In this equation, e is the electronic charge and R is the diabatic electron-transfer distance; that is, the distance between redox centers in the absence of electronic coupling.[19,20] In the case of class-III mixed-valence compounds, we saw previously that V can also be obtained directly from the absorption maximum:

$$V = \frac{\nu_{max}}{2} \qquad 3.3$$

Estimates of V from Equation 3.2, obtained using the experimentally determined values of μ_{ge} and ν_{max} and taking R as the geometric N–N distance, are given in Table 3.8, along with values from Equation 3.3.

Table 3.8 Hush estimates of the electronic coupling in $\mathbf{I}^+$–$\mathbf{II}^+$ and $\mathbf{1}^+$–$\mathbf{4}^+$

Compound	$V_{[Eq.3.2]}$ (cm^{-1})	$V_{[Eq.3.3]}$ (cm^{-1})
$\mathbf{I}^{+[a]}$	1400	3040
$\mathbf{II}^{+[b]}$	1540	3180
$\mathbf{1}^+$	2060	4380
$\mathbf{2}^+$	2860	5050
$\mathbf{3}^+$	3390	5250
$\mathbf{4a}^+$	3550	6250

[a] From Ref. 8. [b] From Ref. 10.

According to either estimate, cations $\mathbf{1}^+$–$\mathbf{4}^+$ show large electronic couplings, as anticipated from the electron-rich character of the thiophene-based bridges. Comparison of the dithienylethene and stilbene compounds, $\mathbf{1}^+$ and $\mathbf{I}^+$, or of the bithiophene and biphenyl compounds, $\mathbf{2}^+$ and $\mathbf{II}^+$, shows that replacement of benzene with thiophene leads to increased electronic coupling. We note that a value of $V_{[Eq.3.3]}$ = 5550 cm^{-1} can be deduced from the published spectrum of $\mathbf{2a}^+$,[21] the structure of which is shown in Figure 3.9. The increase in coupling relative to that of $\mathbf{2}^+$ emphasizes the importance of the *relative* electron-richness of the bridge and amine groups; that is, one can enhance V by increasing the energy of the bridge, or by reducing the energy of the end groups. The electronic coupling suggested by Equation 3.3 in the dithienopyrrole compound $\mathbf{4}^+$ is the strongest yet reported for a two-center mixed-valence triarylamine.

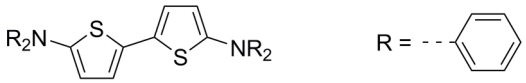

2a

Figure 3.9 Structure of a two-center triarylamine with unsubstituted aryl groups

For all of the compounds in Table 3.8, the electronic coupling values estimated from Equation 3.2 are much smaller than those obtained from Equation 3.3. This discrepancy is attributable to the N–N separation being larger then the true diabatic electron-transfer distance; that is, the redox centers cannot be regarded as centered on the N atoms, but are displaced somewhat into the bridge. The appropriate values of *R* appear to be approximately half of the geometric N–N separation. In view of the reduced diabatic electron-transfer distances, it is interesting to ask to what extent $\mathbf{1}^+$–$\mathbf{4}^+$ can still be regarded as mixed-valence triarylamines, rather than being "bridge-oxidized." To address this question, we turn next to the ESR spectra of the monocations.

3.6 Electron Spin Resonance Spectra of the Monocations

The room-temperature ESR spectra of the radical cations in dichloromethane are shown in Figure 3.10 along with the previously reported spectrum of $\mathbf{I}^+$;[18] the spectra of $\mathbf{1}^+$–$\mathbf{4}^+$ show more resolvable coupling than that in the phenylene analogue. We note that the ESR spectra for the thiophene-bridged compounds are similar to that previously reported for $\mathbf{2a}^+$,[21] in which coupling constants to the amino ^{14}N nuclei and the ^{1}H nuclei of the bridging ligand were of comparable magnitude.

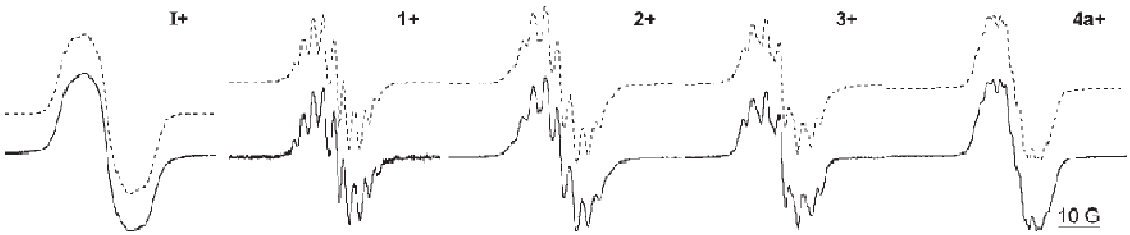

Figure 3.10 Room-temperature ESR spectra of $\mathbf{I}^+$ and $\mathbf{1}^+$–$\mathbf{4}^+$ in dichloromethane (lower, solid lines) with simulations (upper, dotted lines) used to obtain coupling constants[9]

In all cases, the spectra were simulated by assuming hyperfine coupling to two equivalent ^{14}N (I = 1) nuclei and to varying numbers of pairs of ^{1}H (I = ½) nuclei – that is, with the unpaired electron assumed to be delocalized on the ESR timescale. The coupling constants obtained from the simulations are given in Tables 3.9 and 3.10; values obtained from DFT calculations, also included in the tables, are in good agreement with the experimental data and allow us to assign the resolvable ^{1}H splitting, as indicated in Figures 3.11 and 3.12. The agreement suggests that DFT accurately describes the spin distribution in the radical cations, and thus that we can use DFT spin densities to assess the degree to which the oxidation can be regarded as amine-based.

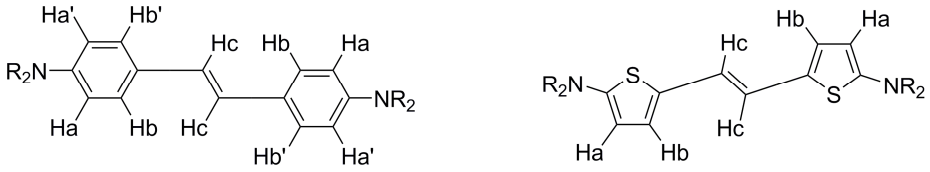

Figure 3.11 Magnetic nuclei for which coupling constants are given in Table 3.9

Table 3.9 Hyperfine coupling constants (G) for $\mathbf{I}^+$ and $\mathbf{1}^+$ obtained from simulation of the room-temperature ESR spectra with DFT gas phase values[a] in italics

	$\mathbf{I}^+$		$\mathbf{1}^+$	
a_N	3.80	*3.63*	2.68	*2.89*
a_{Ha}	[b]	*–0.76, –0.83*[c]	2.00	*–1.88*
a_{Hb}	[b]	*–0.28, –0.33*[c]	2.28	*–2.10*
a_{Hc}	[b]	*–1.51*	1.90	*–1.81*

[a] Computed with spin-unrestricted DFT at the B3LYP/6-31G(d,p) level. [b] Not resolvable in the experimental spectrum. [c] a_{Ha}, $a_{Ha'}$ or a_{Hb}, $a_{Hb'}$, respectively.

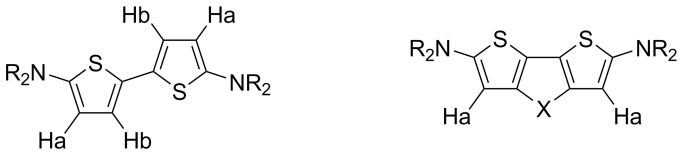

Figure 3.12 Magnetic nuclei for which coupling constants are given in Table 3.10

Table 3.10 Hyperfine coupling constants (G) for $\mathbf{2}^+$–$\mathbf{4}^+$ obtained from simulation of the room-temperature ESR spectra with DFT gas phase values[a] in italics

	$\mathbf{2}^+$		$\mathbf{3}^+$		$\mathbf{4a}^+$	
$a_{N(amine)}$	3.20	*3.30*	3.44	*3.42*	3.17	*3.13, 3.16*
a_{Ha}	2.70	*–2.49*	2.15	*–1.85*	1.24	*–1.15, –1.19*
a_{Hb}	2.20	*–2.15*	–	–	–	–
$a_{N(pyrrole)}$	–	–	–	–	1.61	*–1.23*

[a] Computed with spin-unrestricted DFT at the B3LYP/6-31G(d,p) level

In the previous chapter, we saw that a value of $a_N \approx 9.0$ G was reported for the monocation of tri(anisyl)amine;[22] a delocalized mixed-valence compound consisting of two such redox centers would thus be expected to show $a_N \approx 4.5$ G. The a_N values for $\mathbf{1}^+$–$\mathbf{4}^+$ are significantly lower, suggesting that the spin density on the bridge is increased at the expense of that on the redox centers. This is consistent with the shift of the diabatic states into the bridge suggested by near-IR data. DFT-computed spin densities are also consistent with this picture. As shown in Table 3.11, there is considerably more spin

density on the bridge, with a concomitant reduction in spin density on the amine N atoms. While the bridge character of the oxidation is increased in $\mathbf{1}^+$–$\mathbf{4}^+$ relative to that in analogues such as $\mathbf{I}^+$, the calculations indicate that the N atoms bear almost one-third of the spin density. Thus, the redox centers still play a dominant role in the oxidation process; i.e., the cations can still be regarded as mixed-valence triarylamines, albeit with an appreciable bridge-based character.

Table 3.11 DFT-computed spin densities[a] for different portions of $\mathbf{I}^+$ and $\mathbf{1}^+$–$\mathbf{4}^+$

	$\mathbf{I}^+$	$\mathbf{1}^+$	$\mathbf{2}^+$	$\mathbf{3}^+$	$\mathbf{4a}^+/\mathbf{4b}^+$
Terminal aryl	0.27	0.12	0.15	0.17	0.13
Amino N atoms	0.31	0.24	0.28	0.29	0.27
Bridging group	0.42	0.63	0.57	0.54	0.60

[a] Computed with spin-unrestricted DFT at the B3LYP/6-31G(d,p) level

In this chapter, we saw that two-center triarylamines with thiophene-based bridges undergo facile oxidation. The near-IR spectra of the monocations show absorptions characteristic of delocalized class-III compounds; analysis of the absorptions in the framework of Hush theory indicates strong coupling between the two redox centers, stronger than that observed in compounds with phenylene-based bridges of comparable length. The strong coupling can be attributed to high-lying orbitals of the thiophene-based bridges, as well as to favorable steric interactions. ESR spectroscopy indicates that the hyperfine coupling to nitrogen is reduced relative to that in a stilbene-bridged analogue. DFT-computed ESR parameters are in good agreement with experiment, while calculated spin densities suggest increased bridge character to the oxidation relative to that in comparable compounds with phenylene-based bridges.

REFERENCES

[1] Robin, M. B.; Day, P. *Adv. Inorg. Chem. Radiochem.* **1967**, *10*, 247.

[2] Hush, N. S. *Prog. Inorg. Chem.* **1967**, *8*, 391.

[3] Lambert, C.; Nöll, G.; Schelter, J. *Nat. Mater.* **2002**, *1*, 69.

[4] Lambert, C.; Amthor, S.; Schelter. J. *J. Phys. Chem. A* **2004**, *108*, 6474.

[5] Lambert, C.; Risko, C.; Coropceanu, V.; Schelter, J.; Amthor, S.; Gruhn, N. E.; Durivage, J. C.; Brédas, J. L. *J. Am. Chem. Soc.* **2005**, *127*, 8508.

[6] Sell, J. A.; Kuppermann, A. *Chem. Phys. Lett.* **1979**, *61*, 355.

[7] Åsbrink, L.; Lindholm, E.; Edqvist, O. *Chem. Phys. Lett.* **1970**, *5*, 609.

[8] Barlow, S.; Risko, C.; Chung, S.-J.; Tucker, N. M.; Coropceanu, V.; Jones, S. C.; Levi, Z.; Brédas, J.-L.; Marder, S. R. *J. Am. Chem. Soc.* **2005**, *127*, 16900.

[9] Odom, S. A.; Lancaster, K.; Beverina, L.; Lefler, K. M.; Thompson, N. J.; Coropceanu, V.; Brédas, J.-L.; Marder, S. R.; Barlow, S. *Chem. Eur. J.* **2007**, *13*, 9637.

[10] Lambert, C.; Nöll, G. *J. Am. Chem. Soc.* **1999**, *121*, 8434.

[11] Connelly, N. G.; Geiger, W. E. *Chem. Rev.* **1996**, *96*, 877.

[12] Nelsen, S. F. *Chem. Eur. J.* **2000**, *6*, 581.

[13] Coropceanu, V.; Malagoli, M.; André, J. M.; Brédas, J.-L. *J. Chem. Phys.* **2001**, *115*, 10409.

[14] Coropceanu, V.; Malagoli, M.; André, J. M.; Brédas, J.-L. *J. Am. Chem. Soc.* **2002**, *124*, 10519.

[15] Coropceanu, V.; Lambert, C.; Nöll, G.; Brédas, J.-L. *Chem. Phys. Lett.* **2003**, *373*, 153.

[16] Szeghalmi, A. V.; Erdmann, M.; Engel, V.; Schmitt, M.; Amthor, S.; Kriegisch, V.; Nöll, G.; Stahl, R.; Lambert, C.; Leusser, D.; Stalke, D.; Zabel, M.; Popp, J. *J. Am. Chem. Soc.* **2004**, *126*, 7834.

[17] Low, P. J.; Paterson, M. A. J.; Puschmann, H.; Goeta, A. E.; Howard, J. A. K.; Lambert, C.; Cherryman, J. C.; Tackley, D. R.; Leeming, S.; Brown, B. *Chem. Eur. J.* **2004**, *10*, 83.

[18] Barlow, S.; Risko, C.; Coropceanu, V.; Tucker, N. M.; Jones, S. C.; Levi, Z.; Khrustalev, V. N.; Antipin, M. Y.; Kinnibrugh, T. L.; Timofeeva, T.; Marder, S. R.; Brédas, J.-L. *Chem. Commun.* **2005**, 764.

[19] Creutz, C.; Newton, M. D.; Sutin, N. *J. Photochem. Photobiol. A: Chem.* **1994**, *82*, 47.

[20] Cave, R. J.; Newton, M. D. *Chem. Phys. Lett.* **1996**, *249*, 15.

[21] Rohde, D.; Dunsch, L.; Tabet, A.; Hartmann, H.; Fabian, J. *J. Phys. Chem. B* **2006**, *110*, 8223.

[22] Seo, E. T.; Nelson, R. F.; Fritsch, J. M.; Marcoux, L. S.; Leedy, D. W.; Adams, R. N. *J. Am. Chem. Soc.* **1966**, *88*, 3498.

CHAPTER 4

INTRAMOLECULAR ELECTRON TRANSFER IN TWO-CENTER CLASS-II MIXED-VALENCE TRIARYLAMINES

4.1 Two-Center Class-II Triarylamines

Mixed-valence compounds that contain only two redox centers are among the simplest model systems for the study of electron transfer phenomena. The interplay between the electronic coupling (V) and the reorganization energy (λ) in such a compound determines whether it belongs to Robin and Day's class-II (i.e., is valence-localized) or class-III (valence-delocalized) and, in the former case, influences the rate of intramolecular electron transfer.[1] Both V and λ can be obtained from a Hush analysis of the intervalence band associated with *optical* intramolecular electron transfer.[2] In the semi-classical formalism:

$$\lambda = \nu_{max} \tag{4.1}$$

where ν_{max} is the energy of the intervalence band maximum, while V is given by:

$$V = \frac{\mu_{ge}\nu_{max}}{eR} \tag{4.2}$$

where μ_{ge} is the transition dipole moment of the intervalence band and R is the diabatic electron transfer distance.[3] While μ_{ge} and ν_{max} are accessible from optical measurements, R can only be obtained indirectly,[4] and is often simply equated to the geometric distance between redox centers. In the previous chapter, we saw that estimates of V from Equation 4.2 are particularly problematic for organic mixed-valence

compounds where, in addition to the possibility of delocalization of the diabatic states into the bridge, the centers of multi-atom redox sites are themselves difficult to define.

At the same time, determination of the activation barrier (ΔG^*) associated with *thermal* intramolecular electron transfer can also afford insight into the microscopic parameters:[5]

$$\Delta G^* = \frac{(\lambda - 2V)^2}{4\lambda} \qquad 4.3$$

The barrier can be obtained from variable-temperature measurements of the electron transfer rate. The appropriate spectroscopic tool depends on the magnitude of the rates and the chemical nature of the system in question. Variable-temperature ESR spectroscopy, in particular, is widely used for measuring electron transfer rates and activation barriers in organic mixed-valence compounds.[6–17]

An important subset of organic mixed-valence compounds are those with triarylamine redox centers, due in part to the role played by two-center triarylamines as hole-transport materials in organic electronic applications.[18] Although optical electron transfer is often studied in such compounds,[19–38] we are aware of only one determination of *thermal* electron transfer rates in mixed-valence triarylamines: as we saw in Chapter 2, variable-temperature ESR was used to measure electron transfer rates for an example with a spiro Si linkage, but the absence of an intervalence band in the expected near-IR region precluded comparison with optical estimates of V and λ.[39] The same technique was also employed to study *inter*molecular electron transfer in solutions containing TPD and its class-III radical cation.[40] Most ESR studies of mixed-valence triarylamines, however, are restricted to room-temperature spectra of species that appear delocalized on

the ESR timescale; i.e., those in which the unpaired electron shows equivalent coupling to both nitrogen centers due to either static delocalization in class-III compounds or rapid intramolecular electron transfer in class-II compounds.[29–31,35,36]

Here we report an ESR study of the triarylamine monocations $\mathbf{1}^+$–$\mathbf{3}^+$ and $\mathbf{5}^+$–$\mathbf{7}^+$, the structures of which are shown in Figure 4.1, while an additional model compound, $\mathbf{4}^+$, is studied only computationally. In particular, the magnitudes of V, λ and the hyperfine interactions in $\mathbf{3}^+$ and $\mathbf{7}^+$ allow one to observe transitions from slow to fast electron transfer regimes on the ESR timescale as a function of temperature. The well-resolved intervalence bands of $\mathbf{3}^+$ and $\mathbf{7}^+$ also permit estimates of the microscopic parameters using Equations 4.1 and 4.2, thus allowing the *first comparison of thermal and optical electron transfer in mixed-valence triarylamines*.

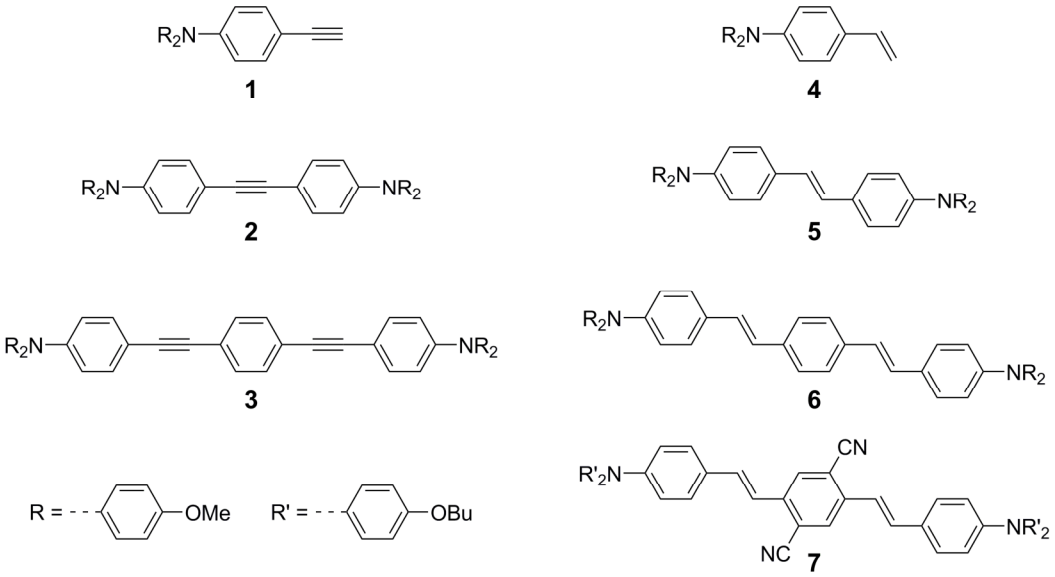

Figure 4.1 Structure of compounds **1**–**7**

4.2 Electron Spin Resonance Spectra

The radical cations of **1–3** and **5–7** were generated in dichloromethane by chemical oxidation using tris(*p*-bromophenyl)aminium hexachloroantimonate. To minimize contributions to the optical and ESR spectra from dications arising from disproportionation, a ca. 10-fold excess of the neutral amine derivative was added to a known concentration of the oxidant. For ESR spectra recorded at room temperature (those shown in Figure 4.2), the solutions were ca. 3×10^{-4} M in monocation and were recorded from samples in 4 mm ESR tubes. Consistent with a previous study of solutions containing TPD and its radical cation at similar concentrations,[40] the room temperature ESR spectra appear to be unaffected by *inter*molecular electron transfer between neutral and cationic species.

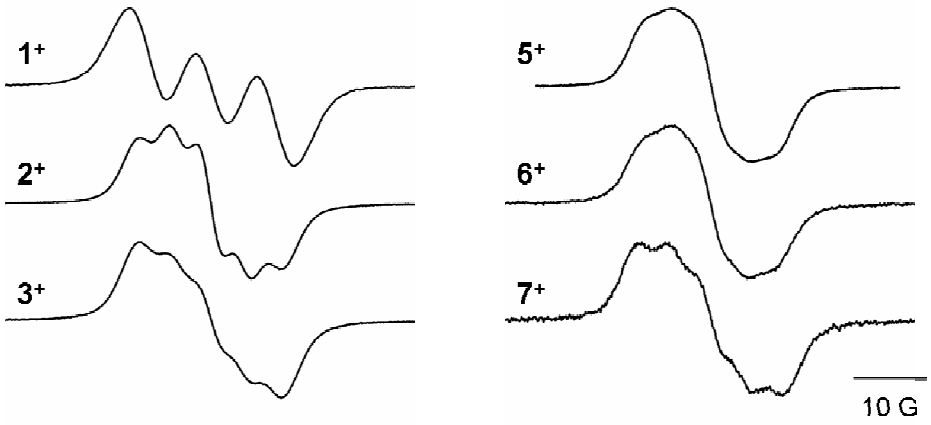

Figure 4.2 Room-temperature ESR spectra of $\mathbf{1}^+$–$\mathbf{3}^+$ and $\mathbf{5}^+$–$\mathbf{7}^+$ obtained upon chemical oxidation in dichloromethane[41]

For ESR spectra recorded at variable temperatures (those shown in Figures 4.3, 4.4 and 4.5), smaller tubes and, therefore, higher concentrations were required for technical reasons. Solutions were ca. 3×10^{-3} M in radical cation and were obtained

from samples in 2 mm ESR tubes. The ESR spectra of $\mathbf{3}^+$ and $\mathbf{7}^+$ show significant temperature dependence, while the low-temperature (ca. 180 K) spectra of $\mathbf{2}^+$ and $\mathbf{6}^+$ are essentially the same as the respective room-temperature spectra in Figure 4.2. In the case of $\mathbf{3}^+$ and $\mathbf{7}^+$, the high-concentration room-temperature spectra are very similar to those obtained at lower concentration, indicating that the effect of intermolecular exchange can be neglected. In the case of $\mathbf{2}^+$ and $\mathbf{6}^+$, however, the room-temperature spectra at higher concentration are narrowed and show less well-resolved coupling relative to the low concentration sample, presumably indicating some influence from intermolecular exchange. As we saw in Chapter 2, *inter*molecular electron transfer is expected to lead to a narrow Lorentzian lineshape and loss of hyperfine coupling.[40]

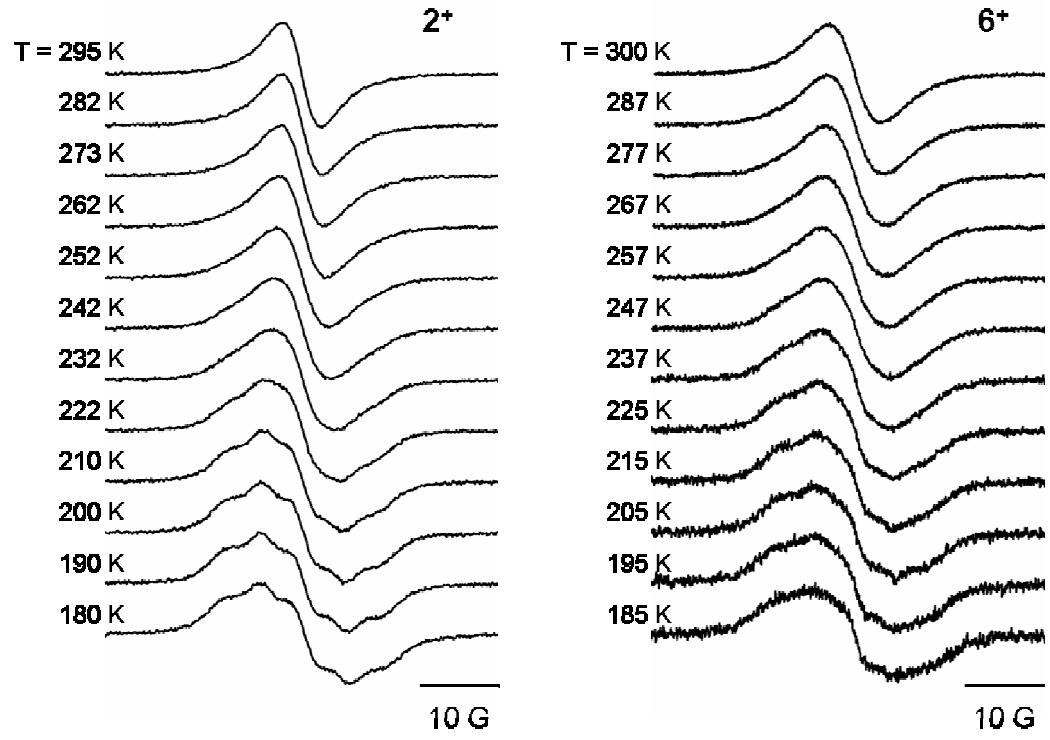

Figure 4.3 Variable-temperature ESR spectra for $\mathbf{2}^+$ and $\mathbf{6}^+$ obtained upon chemical oxidation in dichloromethane[41]

As shown in Figure 4.4, the low-temperature three-line ESR spectrum of $\mathbf{3}^+$ is nearly identical to the room-temperature spectrum of $\mathbf{1}^+$ in Figure 4.2, consistent with coupling of the unpaired electron to a single ^{14}N (I = 1) nucleus, i.e., with slow intramolecular electron transfer on the ESR timescale. As the temperature is increased, a transition to a five-line pattern is observed, consistent with an increase in the rate of thermal intramolecular electron transfer. The same pattern emerges for $\mathbf{7}^+$ in Figure 4.5, although the three-line low-temperature ESR spectrum is still affected by intramolecular exchange and so does not correspond to the slow limit.

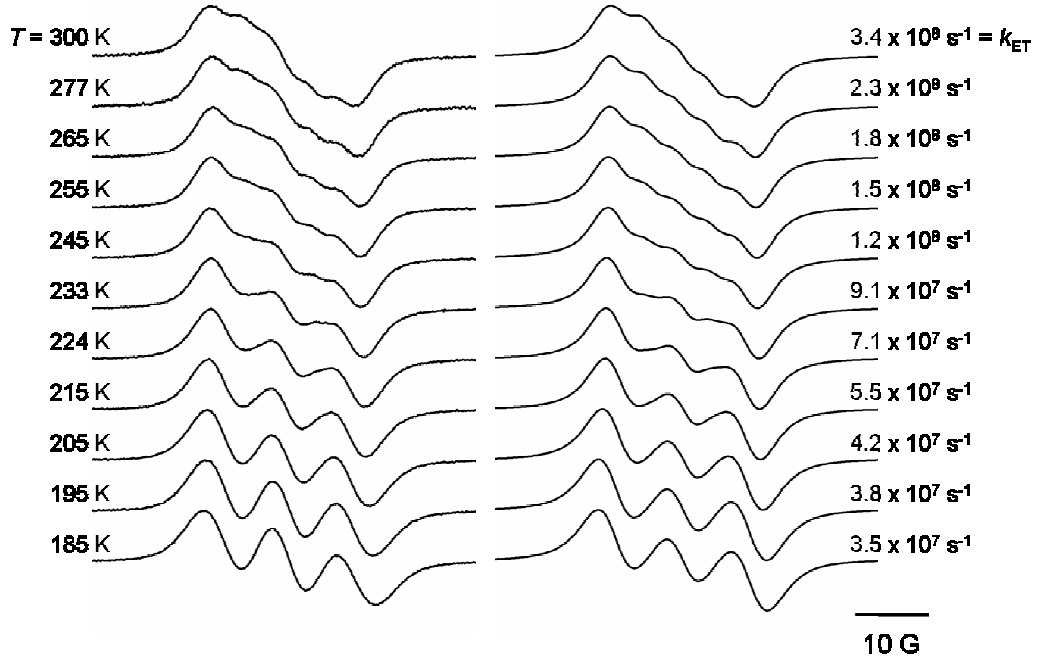

Figure 4.4 Variable-temperature ESR spectra for $\mathbf{3}^+$ obtained upon chemical oxidation in dichloromethane (left) and simulated spectra with derived exchange rates (right)[41]

Table 4.1 Parameters used in the simulation of the VT-ESR spectra for $\mathbf{3}^+$

T (K)	a_N (G)	a_{H1} (G)[a]	a_{H2} (G)[b]	ΔB (G)	k_{ET} (s^{-1})
185	9.2	1.9	1.4	2.3	3.5×10^7
195	9.2	1.9	1.4	2.2	3.8×10^7
205	8.8	1.9	1.4	2.1	4.2×10^7
215	8.6	1.9	1.4	2.0	5.5×10^7
224	8.6	1.9	1.4	2.0	7.1×10^7
233	8.6	1.9	1.4	2.1	9.1×10^7
245	8.5	1.9	1.4	2.2	1.2×10^8
255	8.5	1.9	1.4	2.3	1.5×10^8
265	8.4	1.9	1.4	2.3	1.8×10^8
277	8.4	1.9	1.4	2.3	2.3×10^8
300	8.4	1.9	1.4	2.5	3.4×10^8

[a] Coupling to four equivalent ^{1}H nuclei. [b] Coupling to two equivalent ^{1}H nuclei.

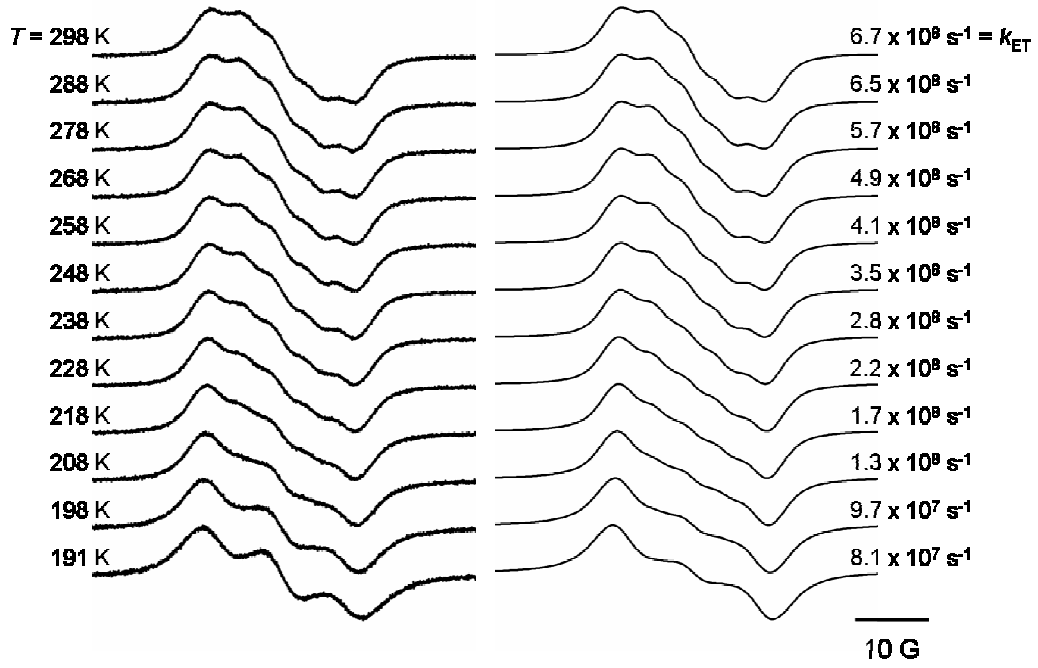

Figure 4.5 Variable-temperature ESR spectra for $\mathbf{7}^+$ obtained upon chemical oxidation in dichloromethane (left) and simulated spectra with derived exchange rates (right)[41]

Table 4.2 Parameters used in the simulation of the VT-ESR spectra for $\mathbf{7}^+$

T (K)	a_N (G)	a_{H1} (G)[a]	a_{H2} (G)[b]	a_{H3} (G)[c]	ΔB (G)	k_{ET} (s^{-1})
191	8.9	1.9	1.4	2.4	2.4	8.1×10^7
198	8.7	1.9	1.4	2.4	2.2	9.7×10^7
208	8.6	1.9	1.4	2.4	1.9	1.3×10^8
218	8.5	1.9	1.4	2.4	1.8	1.7×10^8
228	8.5	1.9	1.4	2.4	1.8	2.2×10^8
238	8.4	1.9	1.4	2.4	1.8	2.8×10^8
248	8.4	1.9	1.4	2.4	1.8	3.5×10^8
258	8.4	1.9	1.4	2.4	1.8	4.1×10^8
268	8.4	1.9	1.4	2.4	1.8	4.9×10^8
278	8.4	1.9	1.4	2.4	1.9	5.7×10^8
288	8.4	1.9	1.4	2.4	1.9	6.5×10^8
298	8.4	1.9	1.4	2.4	1.9	6.7×10^8

[a] Coupling to four equivalent ^{1}H nuclei. [b] Coupling to two equivalent ^{1}H nuclei. [c] Coupling to one ^{1}H nucleus.

The variable-temperature ESR spectra for $\mathbf{3}^+$ and $\mathbf{7}^+$ were simulated using Heinzer's ESR-EXN program to obtain intramolecular exchange rates.[42,43] Hyperfine coupling constants for $\mathbf{1}^+$ and $\mathbf{4}^+$ were computed with spin-unrestricted DFT at the B3LYP/6-31G(d,p) level to model the instantaneous localization of charge on one triarylamine. As we saw in Chapter 3, this level of computation gives hyperfine coupling values in good agreement with those obtained from ESR spectra for class-III mixed-valence triarylamines.[36] The values computed for $\mathbf{1}^+$ and $\mathbf{4}^+$ were taken as initial inputs in the simulations for $\mathbf{3}^+$ and $\mathbf{7}^+$, respectively, and then adjusted, along with the linewidth and exchange rate, to obtain the best fit to each experimental spectrum. Based on the DFT calculations, hyperfine interactions with one ^{14}N (I = 1) nucleus and six (or seven) ^{1}H (I = ½) nuclei were included for $\mathbf{3}^+$ (or $\mathbf{7}^+$). The DFT values are given in Table 4.3, while the parameters used in the simulations are given in Tables 4.1 and 4.2.

The simulations yield exchange rates, k_{ET}, that range from ca. 10^7 s^{-1} at low temperature to ca. 10^8 s^{-1} at high temperature. The a_N values obtained are comparable to a value of 8.97 G previously reported for the tris(*p*-methoxyphenyl)aminium ion in acetonitrile.[44] Although the room-temperature ESR spectra for $\mathbf{3}^+$ and $\mathbf{7}^+$ exhibit five lines, the lineshapes do not correspond to those for the fast-exchange limit in which the triarylamine centers are equivalent on the ESR timescale; simulations with $k_{ET} > 10^{10}$ s^{-1} indicate that in this case the height of the second peak in the ESR spectrum would exceed that of the first.

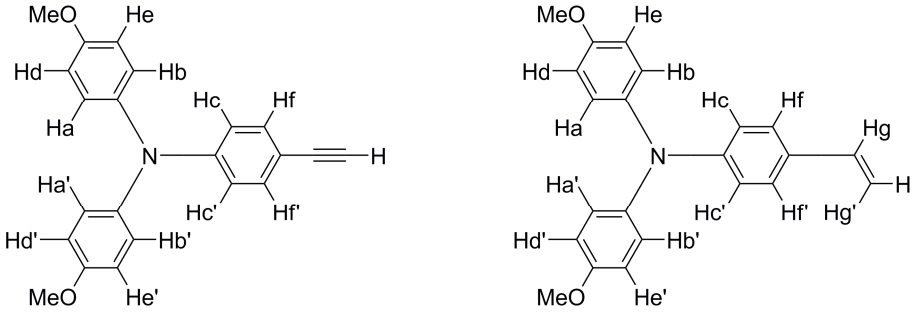

Figure 4.6 Magnetic nuclei for which coupling constants are given in Table 4.3

Table 4.3 Atomic spin densities (ρ_N) and hyperfine coupling constants (a_X) from spin-unrestricted DFT calculation[a]

a_X (G)	$\mathbf{1}^+$	$\mathbf{4}^+$	a_X (G)	$\mathbf{1}^+$	$\mathbf{4}^+$
ρ_N	0.31	0.31	a_{Hd}	0.57	0.56
a_N	7.29	7.27	$a_{Hd'}$	0.57	0.58
a_{Ha}	–1.97	–1.93	a_{He}	0.45	0.52
$a_{Ha'}$	–1.97	–1.93	$a_{He'}$	0.45	0.51
a_{Hb}	–1.42	–1.38	a_{Hf}	1.24	1.21
$a_{Hb'}$	–1.42	–1.40	$a_{Hf'}$	1.24	1.23
a_{Hc}	–1.89	–2.05	a_{Hg}	–	1.00
$a_{Hc'}$	–1.89	–1.84	$a_{Hg'}$	–	–2.80

[a] Computed with the B3LYP functional and the 6-31G(d,p) basis set.

As shown in Figure 4.7, the room-temperature ESR spectra of $\mathbf{2}^+$, $\mathbf{5}^+$ and $\mathbf{6}^+$ are quite similar to one another, although those of $\mathbf{5}^+$ and $\mathbf{6}^+$ are somewhat less well-resolved than that of $\mathbf{2}^+$ due to hyperfine coupling to the additional ^{1}H nuclei of the vinylene groups. In contrast to the room-temperature ESR spectra of $\mathbf{3}^+$ and $\mathbf{7}^+$, where the outer peaks are the most intense, the second peaks are more intense in the spectra of $\mathbf{2}^+$, $\mathbf{5}^+$ and $\mathbf{6}^+$, consistent with electron transfer in the fast limit on the ESR timescale. These spectra can be simulated equally well assuming either rapid intramolecular exchange between two nitrogen centers with $a(1N) \approx 8$ G and $k_{ET} > 10^{10}$ s^{-1} or a static delocalization with $a(2N) \approx 4$ G, as shown in Table 4.4.

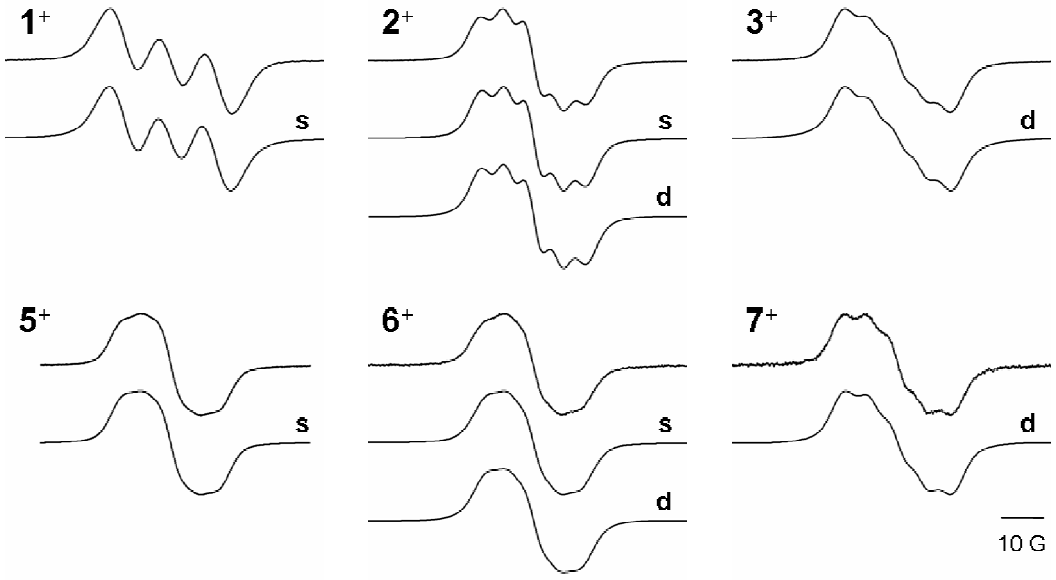

Figure 4.7 Room-temperature ESR spectra and static (**s**) or dynamic (**d**) simulation[41]

Table 4.4 Parameters used in the simulation of the room-temperature ESR spectra[a]

	$\mathbf{1}^+$	$\mathbf{2}^+$		$\mathbf{3}^+$	$\mathbf{5}^+$	$\mathbf{6}^+$		$\mathbf{7}^+$
a_X (G)	*stat*	*stat*	*dyn*	*dyn*	*stat*	*stat*	*dyn*	*dyn*
a_N	8.2 (1)	4.1 (2)	8.2 (1)	8.4 (1)	3.7 (2)	3.7 (2)	7.4 (1)	8.4 (1)
a_{H1}	1.9 (4)	0.9 (8)	1.9 (4)	1.9 (4)	0.8 (8)	0.7 (8)	1.9 (4)	1.9 (4)
a_{H2}	1.4 (2)	0.6 (4)	1.4 (2)	1.4 (2)	0.6 (4)	0.5 (4)	1.4 (2)	1.4 (2)
a_{H3}	–	–	–	–	1.5 (2)	1.1 (2)	2.4 (1)	2.4 (1)
ΔB (G)	2.7	1.9	2.0	2.5	1.7	2.4	2.0	1.9
k_{ET} (s^{-1})	–	–	10^{10}	3.4×10^8	–	–	10^{10}	6.7×10^8

[a] Number in parentheses indicates the number of nuclei corresponding to each coupling constant.

4.3 Comparison of Optical and Thermal ET Parameters

We saw in the first chapter that the microscopic parameters, V and λ, depend on the nature of the bridge connecting the redox centers. In particular, Hush analyses of the intervalence bands for two-center mixed-valence triarylamines showed that the bridge length, saturation, and energy influence the interaction between centers. The ESR behavior of the compounds studied here is fully consistent with this optical analysis. That electron transfer is more rapid in $\mathbf{6}^+$ compared to $\mathbf{3}^+$ is consistent with the stronger electronic coupling (V) and lower reorganization energy (λ) in the vinylene-bridged compound than in its ethynylene analogue as determined by Hush analysis.[22,31] The fast-limit ESR spectra of the shorter compounds $\mathbf{2}^+$ and $\mathbf{5}^+$ are also consistent with the larger V (and, in the case of $\mathbf{2}^+$ vs. $\mathbf{3}^+$, lower λ) values previously estimated from optical data; indeed, the lineshape and solvatochromism of its intervalence band suggest that $\mathbf{5}^+$ is statically delocalized, i.e., that it belongs to Robin and Day's class-III.[21,22,30] The differences in ESR behavior between $\mathbf{6}^+$ and $\mathbf{7}^+$, which have bridges of the same length, are again consistent with the trends in electronic coupling and reorganization energy implied by their intervalence bands.[31] The reduced V in $\mathbf{7}^+$ can be attributed to a bridge

energy effect; that is, the electron-withdrawing cyano substituents lower the energy of the bridge-based orbitals that mediate the coupling between the triarylamine-based orbitals. The intervalence bands for $\mathbf{3}^+$ and $\mathbf{7}^+$ are shown in Figure 4.8.

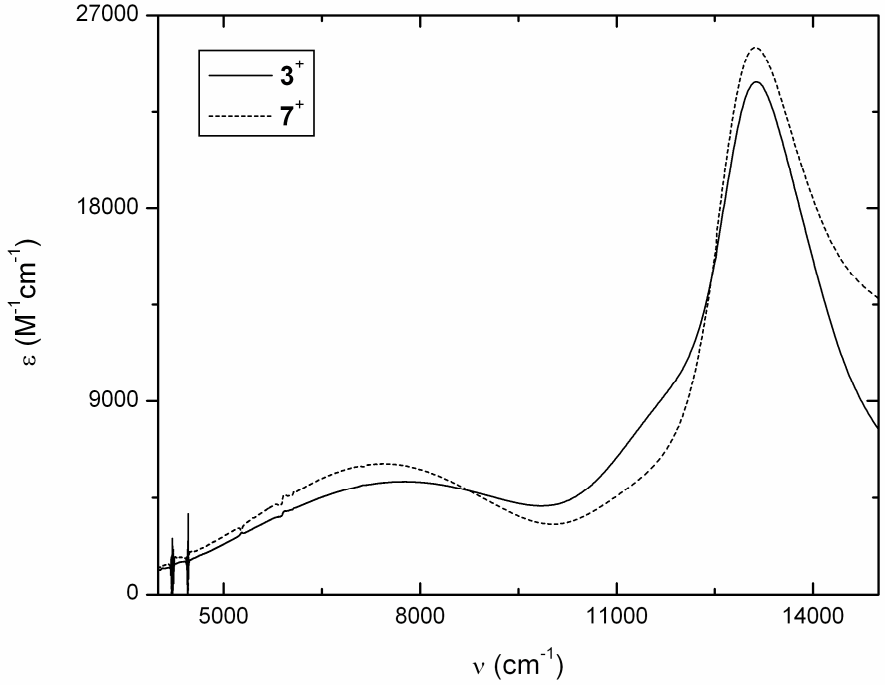

Figure 4.8 Visible-NIR absorption spectra for $\mathbf{3}^+$ and $\mathbf{7}^+$ obtained upon chemical oxidation in dichloromethane, the low-energy bands of which are assigned as intervalence bands[41]

As shown in Figure 4.9, plots of $\ln(k_{ET})$ versus $1/T$ for $\mathbf{3}^+$ and $\mathbf{7}^+$ are linear; this behavior is consistent with an Arrhenius-type temperature dependence of the electron transfer rate:

$$k_{ET} = A\exp\left(\frac{-\Delta G^*}{k_B T}\right) \qquad 4.4$$

where k_B denotes the Boltzmann constant. Rates represented by open symbols in Figure 4.9 were excluded from the linear fits since simulations of the ESR spectra approaching

either the slow or fast limit (low- and high-temperature data for $\mathbf{3}^+$ and $\mathbf{7}^+$, respectively) are rather insensitive to k_{ET}. The activation barriers extracted from the Arrhenius plots, ΔG^*_{ESR}, are given in Table 4.5 along with barriers, ΔG^*_{NN}, estimated from Equation 4.3 using the microscopic parameters obtained from Hush analyses of the intervalence bands. Here, the electronic coupling, V_{NN}, was obtained from Equation 4.2 by taking the diabatic electron transfer distance, R, as the N–N separation, R_{NN}. As shown in Table 4.5, the barriers estimated from optical data are considerably larger than those obtained from ESR data; a similar discrepancy was found for a two-center triarylmethyl radical anion isoelectronic with $\mathbf{7}^+$.[7]

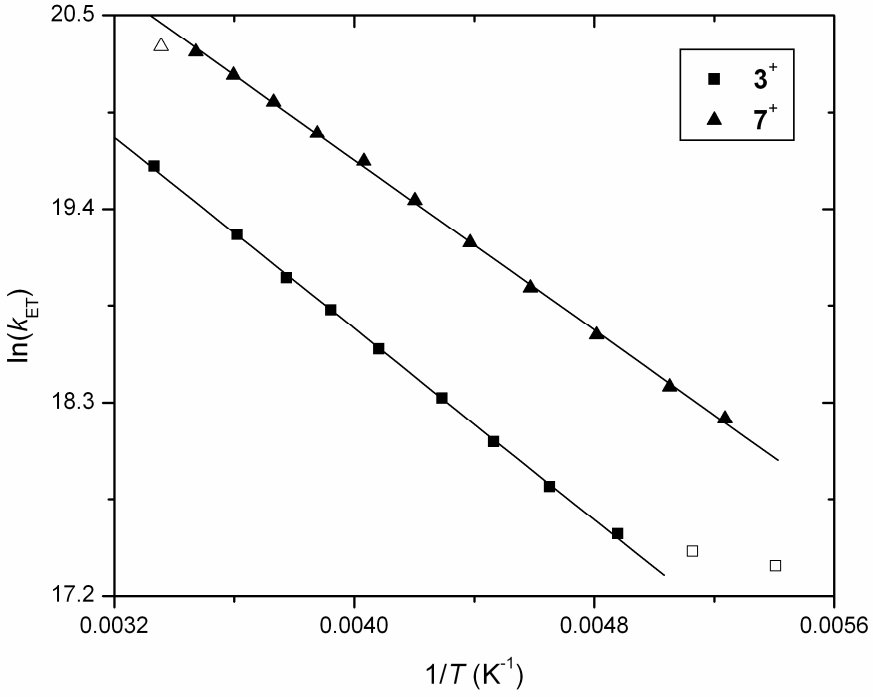

Figure 4.9 Arrhenius plots of the thermal exchange rates from Figures 4.4 and 4.5

From the ESR barriers, ΔG^*_{ESR}, and the optical values of λ, one can obtain ESR estimates of the electronic coupling, V_{ESR}, using Equation 4.3. From these values of

V_{ESR}, along with the optical values of μ_{ge} and ν_{max}, the diabatic electron transfer distance, R_{ESR}, can be obtained using Equation 4.2; as shown in Table 4.5, these values imply that R in $\mathbf{3}^+$ and $\mathbf{7}^+$ is less than half the N–N distance. Previous studies of class-III compounds, for which an alternative optical estimate of V (namely, $V = \nu_{max}/2$) can be compared with that from Equation 4.2, also indicate that the N–N distance is a poor approximation of R for two-center triarylamines with conjugated bridging groups;[30,31,36] this implies that the diabatic states cannot be regarded as purely localized on the triarylamines. Quantum-chemical estimates of R for class-II and -III compounds, including $\mathbf{5}^+$ and $\mathbf{6}^+$, also suggest R to be less than the N–N separation.[31] Our results for $\mathbf{3}^+$ and $\mathbf{7}^+$, however, represent the first *experimental* demonstration that $R < R_{NN}$ for localized class-II mixed-valence triarylamines.

Table 4.5 Comparison of optical and thermal electron transfer parameters for $\mathbf{3}^+$ and $\mathbf{7}^+$

Vis-NIR	$\mathbf{3}^+$	$\mathbf{7}^+$	ESR	$\mathbf{3}^+$	$\mathbf{7}^+$
λ (cm^{-1})[a]	7780	7450	k_{ET} (s^{-1})[f]	3.4×10^8	6.7×10^8
μ_{ge} (D)[b]	5.85	5.78	A_{ESR} (s^{-1})[g]	3.1×10^{10}	4.4×10^{10}
R_{NN} (Å)[c]	19.45	19.03	R_{ESR} (Å)[h]	8.0	7.4
V_{NN} (cm^{-1})[d]	490	470	V_{ESR} (cm^{-1})[i]	1180	1220
ΔG^*_{NN} (cm^{-1})[e]	1490	1420	ΔG^*_{ESR} (cm^{-1})[g]	940	840

Obtained from: [a] Eq. 4.1; [b] Gaussian fits of the intervalence bands; [c] DFT optimization of the neutral compounds at the B3LYP/6-31G(d,p) level; [d] Eq. 4.2 using ν_{max}, μ_{ge} and R_{NN}; [e] Eq. 4.3 using λ and V_{NN}; [f] Table 4.4; [g] Fits of the ESR rate data to Eq. 4.4; [h] Eq. 4.2 using V_{ESR}, μ_{ge} and ν_{max}; [i] Eq. 4.3 using ΔG^*_{ESR} and λ.

We turn now to the nature of the thermal intramolecular electron transfer processes in $\mathbf{3}^+$ and $\mathbf{7}^+$. In Chapter 2 we saw that, depending on the interplay between the nuclear and electronic frequencies, electron transfer reactions are categorized as adiabatic

or nonadiabatic; the two regimes differ in the prefactor, A, which is determined in limiting cases by the dynamic properties of the slower subsystems.[5] In a nonadiabatic electron transfer reaction, the electronic motion is slower than the vibrational motion, and the prefactor is a function of the electronic coupling:

$$A = V^2 \sqrt{\frac{4\pi^3}{h^2 \lambda k_B T}} \qquad 4.5$$

where h is Planck's constant. In the adiabatic regime, the vibrational motion is slower than the electronic motion and the prefactor is given by:

$$A = \nu_n \qquad 4.6$$

where ν_n is the nuclear frequency of crossing the electron transfer barrier. ESR estimates of the prefactors, A_{ESR}, for $\mathbf{3}^+$ and $\mathbf{7}^+$, obtained from the fits of the rate data to Equation 4.4, are included in Table 4.5. While the prefactors are somewhat low compared to the range of expected values for solvent reorientation frequencies ($\nu_n \approx 10^{11}$–10^{12} s^{-1}),[5] they are much lower than those obtained by inserting the values of V_{NN} (or V_{ESR}) and λ into Equation 4.5 (10^{13}–10^{14} s^{-1}), indicating that the intramolecular electron transfer in mixed-valence triarylamines of this type occurs in the adiabatic regime, as expected from classical electron transfer theory.

It is worth noting, however, that the values of A_{ESR} are smaller than at first anticipated since high-frequency intramolecular vibrations could also contribute to ν_n. Indeed, prefactors obtained from Arrhenius fits to published ESR rate data for a variety of organic mixed-valence compounds generally fall in the range of 10^{11}–10^{12} s^{-1}.[6,10–16,39] Still, there are precedents for prefactors of the magnitude found for $\mathbf{3}^+$ and $\mathbf{7}^+$; in

particular, a very similar value of 3×10^{10} s^{-1} can be derived for a two-center triarylmethyl radical anion in dichloromethane,[7] a compound which, as shown in Figure 4.10, is structurally analogous to $\mathbf{7}^{+}$.

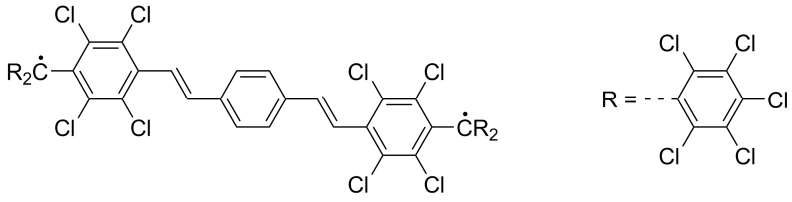

Figure 4.10 Structure of a two-center triarylmethyl diradical, the radical anion of which is isoelectronic with $\mathbf{7}^{+}$

In this chapter, we saw that the intramolecular electron transfer rates in mixed-valence triarylamines depend on the length of the bridging group, linkage by ethynylene vs. vinylene groups, and substitution of bridging phenylene groups, as was expected from electronic couplings and reorganization energies obtained from optical data. Compounds $\mathbf{3}^{+}$ and $\mathbf{7}^{+}$ are the first mixed-valence triarylamines for which ESR spectra were found to exhibit a temperature-dependent transition from the slow to fast regime and in which optical and thermal electron transfer could be observed and correlated. Comparison of the activation barriers obtained from ESR measurements with those estimated from optical data indicates that the diabatic electron transfer distance in class-II mixed-valence triarylamines with conjugated bridging groups is considerably less than the N–N separation, while the variable-temperature ESR data also indicate that the electron transfer in these compounds is adiabatic.

REFERENCES

[1] Robin, M. B.; Day, P. *Adv. Inorg. Chem. Radiochem.* **1967**, *10*, 247.

[2] Hush, N. S. *Prog. Inorg. Chem.* **1967**, *8*, 391.

[3] Creutz, C.; Newton, M. D.; Sutin, N. *J. Photochem. Photobiol. A: Chem.* **1994**, *82*, 47.

[4] Cave, R. J.; Newton, M. D. *Chem. Phys. Lett.* **1996**, *249*, 15.

[5] Sutin, N. *Prog. Inorg. Chem.* **1983**, *30*, 441.

[6] Rak, S. F.; Miller, L. L. *J. Am. Chem. Soc.* **1992**, *114*, 1388.

[7] Bonvoisin, J.; Launay, J.-P.; Rovira, C.; Veciana, J. *Angew. Chem. Int. Ed. Engl.* **1994**, *33*, 2106.

[8] Nelsen, S. F.; Adamus, J.; Wolff, J. J. *J. Am. Chem. Soc.* **1994**, *116*, 1589.

[9] Nelsen, S. F.; Ramm, M. T.; Wolff, J. J.; Powell, D. R. *J. Am. Chem. Soc.* **1997**, *119*, 6863.

[10] Nelsen, S. F.; Trieber, D. A.; Wolff, J. J.; Powell, D. R.; Rogers-Crowley, S. *J. Am. Chem. Soc.* **1997**, *119*, 6873.

[11] Nelsen, S. F.; Ismagilov, R. F.; Powell, D. R. *J. Am. Chem. Soc.* **1997**, *119*, 10213.

[12] Nelsen, S. F.; Ismagilov, R. F.; Trieber, D. A. *Science* **1997**, *278*, 846.

[13] Nelsen, S. F.; Ismagilov, R. F.; Powell, D. R. *J. Am. Chem. Soc.* **1998**, *120*, 1924.

[14] Lindeman, S. V.; Rosokha, S. V.; Sun, D.; Kochi, J. K. *J. Am. Chem. Soc.* **2002**, *124*, 843.

[15] Rosokha, S. V.; Sun, D.-L.; Kochi, J. K. *J. Phys. Chem. A* **2002**, *106*, 2283.

[16] Sun, D.-L.; Rosokha, S. V.; Lindeman, S. V.; Kochi, J. K. *J. Am. Chem. Soc.* **2003**, *125*, 15950.

[17] Sun, D.; Rosokha, S. V.; Kochi, J. K. *J. Am. Chem. Soc.* **2004**, *126*, 1388.

[18] Tang, C. W.; Van Slyke, S. A.; *Appl. Phys. Lett.* **1987**, *51*, 913.

[19] Bonvoisin, J.; Launay, J.-P.; Van der Auweraer, M.; De Schryver, F. C. *J. Phys. Chem.* **1994**, *98*, 5052; correction, *J. Phys. Chem.* **1996**, *100*, 18006.

[20] Bonvoisin, J.; Launay, J.-P.; Verbouwe, W.; Van der Auweraer, M.; De Schryver, F. C. *J. Phys. Chem.* **1996**, *100*, 17079.

[21] Lambert, C.; Nöll, G. *Angew. Chem. Int. Ed.* **1998**, *37*, 2107.

[22] Lambert, C.; Nöll, G. *J. Am. Chem. Soc.* **1999**, *121*, 8434.

[23] Coropceanu, V.; Malagoli, M.; André, J. M.; Brédas, J.-L. *J. Chem. Phys.* **2001**, *115*, 10409.

[24] Coropceanu, V.; Malagoli, M.; André, J. M.; Brédas, J.-L. *J. Am. Chem. Soc.* **2002**, *124*, 10519.

[25] Lambert, C.; Nöll, G.; Schelter, J. *Nat. Mater.* **2002**, *1*, 69.

[26] Lambert, C.; Amthor, S.; Schelter, J. *J. Phys. Chem. A* **2004**, *108*, 6474.

[27] Low, P. J.; Paterson, M. A. J.; Puschmann, H.; Goeta, A. E.; Howard, J. A. K.; Lambert, C.; Cherryman, J. C.; Tackley, D. R.; Leeming, S.; Brown, B. *Chem. Eur. J.* **2004**, *10*, 83.

[28] Szeghalmi, A. V.; Erdmann, M.; Engel, V.; Schmitt, M.; Amthor, S.; Kriegisch, V.; Nöll, G.; Stahl, R.; Lambert, C.; Leusser, D.; Stalke, D.; Zabel, M.; Popp, J. *J. Am. Chem. Soc.* **2004**, *126*, 7834.

[29] Jones, S. C.; Coropceanu, V.; Barlow, S.; Kinnibrugh, T.; Timofeeva, T.; Brédas, J.-L.; Marder, S. R. *J. Am. Chem. Soc.* **2004**, *126*, 11782.

[30] Barlow, S.; Risko, C.; Coropceanu, V.; Tucker, N. M.; Jones, S. C.; Levi, Z.; Khrustalev, V. N.; Antipin, M. Y.; Kinnibrugh, T. L.; Timofeeva, T.; Marder, S. R.; Brédas, J.-L. *Chem. Commun.* **2005**, 764.

[31] Barlow, S.; Risko, C.; Chung, S.-J.; Tucker, N. M.; Coropceanu, V.; Jones, S. C.; Levi, Z.; Brédas, J. L.; Marder, S. R. *J. Am. Chem. Soc.* **2005**, *127*, 16900.

[32] Lambert, C.; Risko, C.; Coropceanu, V.; Schelter, J.; Amthor, S.; Gruhn, N. E.; Durivage, J. C.; Brédas, J. L. *J. Am. Chem. Soc.* **2005**, *127*, 8508.

[33] Amthor, S.; Lambert, C. *J. Phys. Chem. A* **2006**, *110*, 1177.

[34] Amthor, S.; Lambert, C. *J. Phys. Chem. A* **2006**, *110*, 3495.

[35] Rohde, D.; Dunsch, L.; Tabet, A.; Hartmann, H.; Fabian, J. *J. Phys. Chem. B* **2006**, *110*, 8223.

[36] Odom, S. A.; Lancaster, K.; Beverina, L.; Lefler, K. M.; Thompson, N. J.; Coropceanu, V.; Brédas, J.-L.; Marder, S. R.; Barlow, S. *Chem. Eur. J.* **2007**, *13*, 9637.

[37] Nöll, G.; Avola, M.; Lynch, M.; Daub, J. *J. Phys. Chem. C* **2007**, *111*, 3197.

[38] Nöll, G.; Amthor, S.; Avola, M.; Lambert, C.; Daubl, J. *J. Phys. Chem. C* **2007**, *111*, 3512.

[39] Hirao, Y.; Urabe, M.; Ito, A.; Tanaka, K. *Angew. Chem. Int. Ed.* **2007**, *46*, 3300.

[40] Veregin, R. P.; Harbour, J. R. *J. Phys. Chem.* **1990**, *94*, 6231.

[41] Lancaster, K.; Odom, S. A.; Jones, S. C.; Thayumanavan, S.; Marder, S. R.; Brédas, J.-L.; Coropceanu, V.; Barlow, S. *J. Am. Chem. Soc.* **2009**, *131*, 1717.

[42] Heinzer, J. *Mol. Phys.* **1971**, *22*, 167.

[43] Heinzer, J. *Quantum Chemistry Program Exchange* **1972**, *No. 209.*

[44] Seo, E. T.; Nelson, R. F.; Fritsch, J. M.; Marcoux, L. S.; Leedy, D. W.; Adams, R. N. *J. Am. Chem. Soc.* **1966**, *88*, 3498.

CHAPTER 5

INTRAMOLECULAR ELECTRON TRANSFER IN THREE-CENTER CLASS-II MIXED-VALENCE TRIARYLAMINES

5.1 Three-Center Class-II Triarylamines

While mixed-valence compounds with two redox centers are model systems for the study of electron transfer reactions, those with three centers are more realistic models, for they allow more than one pathway of electron transfer. As we saw in Chapter 1, the intramolecular electron transfer processes in mixed-valence compounds depend on the interplay between the electronic (V) and the vibronic (λ) coupling.[1] One can obtain both parameters from a Hush analysis of the intervalence band that arises upon *optical* electron transfer if the band is intense and well-separated from other bands.[2] This is often the case for two-center triarylamines in which the centers are connected through *para*-substituted phenylene bridges, and as such, the intervalence bands in these species are extensively studied.[3–22] When the centers are connected through *meta*-substituted phenylene bridges, however, as for the three-center triarylamine in Figure 5.1, the electronic coupling is weak and the intervalence band is difficult to analyze.[23,24]

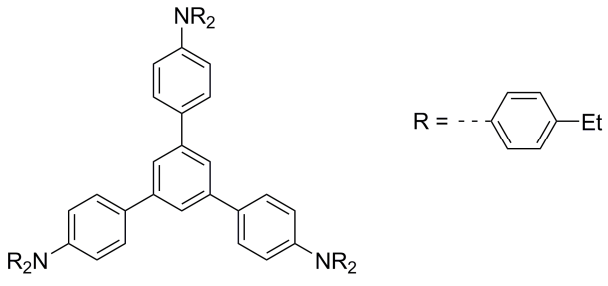

Figure 5.1 Example of a *meta*-connected, three-center triarylamine

It is of interest then to create three-center triarylamines with larger V and thus more intense intervalence bands. In Chapter 3, we saw that replacement of a bridging phenylene group with a more electron-rich thienylene group can increase the electronic coupling in two-center triarylamines.[25] Here we study the monocations of **1**–**4** in Figure 5.2 to determine if one can increase V in the same way for three-center triarylamines.

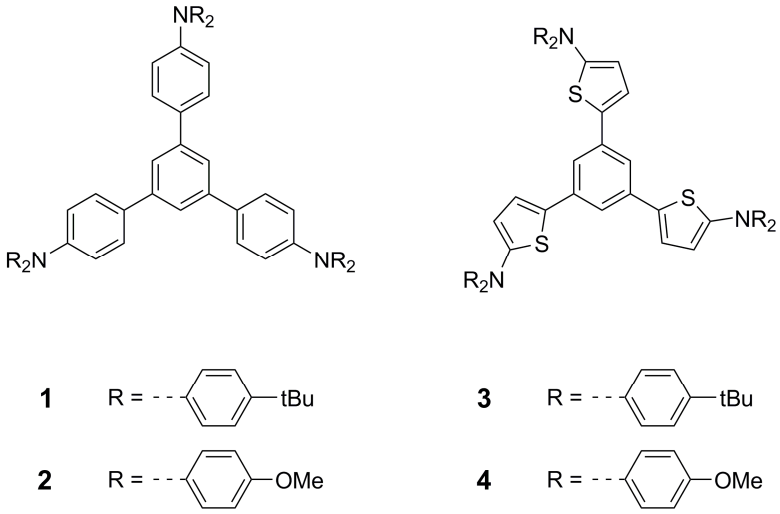

Figure 5.2 Structures of compounds **1**–**4**

The activation barrier to *thermal* electron transfer in a class-II compound is also related to the parameters V and λ.[26] Thus, if one can capture the rate of electron transfer at multiple temperatures, then two experimental methods exist by which to extract V and λ. One technique that is widely used for organic mixed-valence compounds is variable-temperature ESR spectroscopy.[27–37] We saw in Chapter 2, however, that this method is only rarely used to measure electron transfer rates in mixed-valence triarylamines,[38] as the thermal electron transfer in most of the *para*-connected class-II compounds is too fast to observe on the ESR timescale.[13–15] Likewise, the ESR spectra of $\mathbf{A}^+$ and $\mathbf{B}^+$ at 195 K in Figure 5.3 show hyperfine patterns indicative of equal spin density on each amine

center.[39,40] The *meta*-connected compounds thus also show averaged coupling constants, even at low temperature.

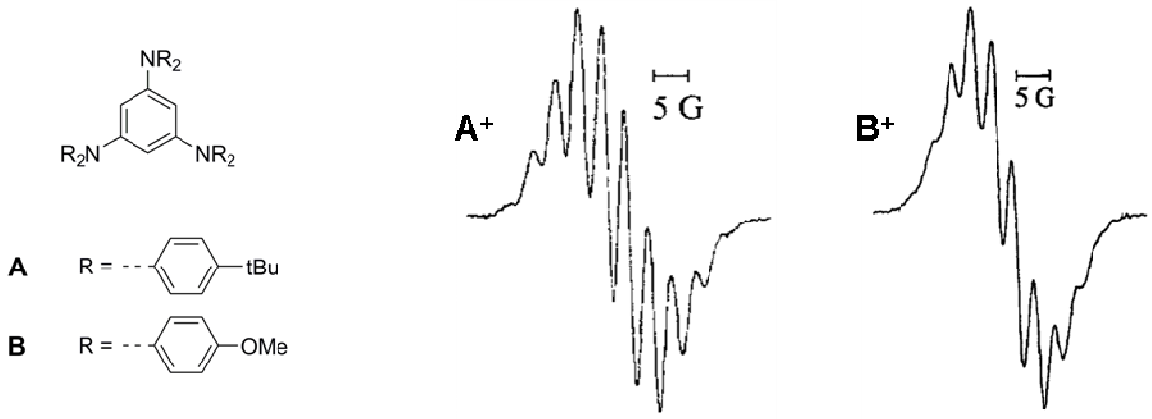

Figure 5.3 Structures of **A** and **B** and ESR spectra of the monocations at 195 K[39,40]

In Chapter 4, we saw that one can reduce the electronic coupling and thus the electron transfer rate by lowering the energy of the bridging group. In this way, we observed the first localized-to-delocalized ESR transition with temperature in mixed-valence triarylamines.[41] Here we show that the larger distance between redox centers in **1** vs. **A** reduces *V* such that one can again observe electron transfer on the ESR timescale. In contrast to the *para*-connected compounds, for which we found adiabatic electron transfer, simulation of variable-temperature ESR spectra based on DFT calculation and comparison with optical data suggests that the thermal electron transfer in the *meta*-connected compounds occurs in the nonadiabatic regime.

In addition to the three-center triarylamines, the two- and one-center compounds in Figure 5.4, **5** and **6**, are studied as controls, and, in the case of **6**, to model the instantaneous localization of charge on one triarylamine.

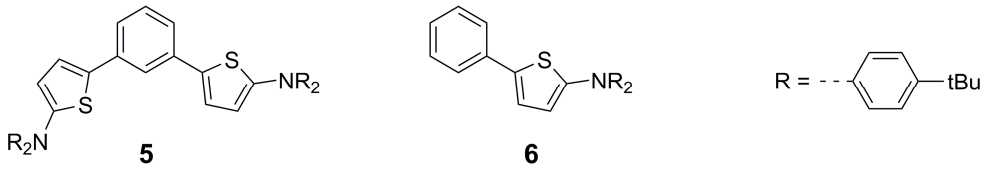

Figure 5.4 Structures of compounds **5** and **6**

5.2 Electrochemistry

Compounds **1**–**6** were analyzed by cyclic voltammetry (CV) to determine oxidation potentials; the two- and three-center compounds were also analyzed by differential pulse voltammetry (DPV) to determine differences in potential between successive oxidations. Representative CV and DPV data for compounds **1** and **3** are shown in Figure 5.5.

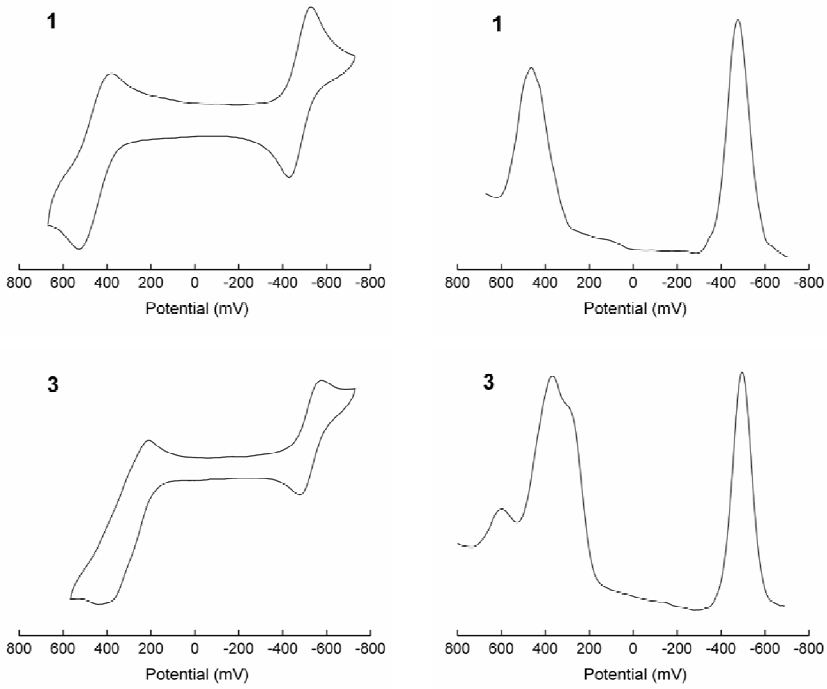

Figure 5.5 Cyclic voltammograms (left) and differential pulse voltammograms (right) of compounds **1** and **3** in 0.1 M $^{n}Bu_4NPF_6$ in dichloromethane, shown with $Cp^*_2Fe^{+/0}$ as the internal reference (–0.55 V vs. $Cp_2Fe^{+/0}$ at 0 V)

The cyclic voltammograms of compounds **1** and **2** are consistent with three overlapping, unresolved one-electron oxidations of the triarylamine centers. DPV experiments show no separation of the multiple oxidations. The fact that multiple oxidations occur at the same potential suggests that the oxidation of one redox center has little effect on the other centers, or that electronic coupling between the centers is weak. The oxidation of **2** ($E_{1/2}^{+/0}$ = +0.27 V) occurs at lower potential than that of **1** ($E_{1/2}^{+/0}$ = +0.42 V), which is consistent with the more electron-rich end groups in **2**.

The cyclic voltammogram of compound **3** shows multiple oxidations at different potentials, although it is not possible to determine the positions of each oxidation from CV without simulation. The three oxidations are separated in the DPV experiments. As expected, **3** is considerably easier to oxidize ($E_{1/2}^{+/0}$ = +0.22 V) than **1** ($E_{1/2}^{+/0}$ = +0.42 V) because of the lower ionization potential of thiophene relative to benzene.[42,43] The fact that the oxidations are separable in **3** could imply that the electronic coupling between redox centers is stronger in **3** than in **1**. On the other hand, the shorter nitrogen-nitrogen distance in **3** might lead to greater electrostatic contributions to the difference in oxidation potentials. The oxidations in compound **4** are also somewhat separated in the CV experiment and better resolved in the DPV experiment. The first oxidation of **4** occurs at lower potential ($E_{1/2}^{+/0}$ = +0.20 V) than that of **3** ($E_{1/2}^{+/0}$ = +0.22 V), which is again consistent with the more electron-rich end groups in **4**.

The CV and DPV data for the two-center compound (**5**) show two reversible oxidations with a separation of ca. 0.09 V. The separation in oxidation potentials suggests that – as is the case for the three-center compound (**3**) – the oxidation of one triarylamine affects the oxidation of a second triarylamine. The first oxidation potential

of **5** ($E_{1/2}^{+/0}$ = +0.22 V) is equivalent to that of **3**, which is consistent with the relatively weak coupling expected from *meta*-substitution around the central benzene ring. Likewise, CV of the one-center compound (**6**) shows one reversible oxidation at the same potential ($E_{1/2}^{+/0}$ = +0.22 V) as the two- (**5**) and three-center (**3**) analogs. The oxidation potentials of compounds **1**–**6** are collected in Table 5.1.

Table 5.1 Half-wave oxidation potentials (V) of compounds **1**–**6**[a]

Compound	+/0	2+/+	3+/2+
1	+0.42[b]		
2	+0.27[b]		
3	+0.22	+0.30	+0.52
4	+0.20	+0.28	+0.40
5	+0.22	+0.31	–
6	+0.22	–	–

[a] In 0.1 M $^{n}Bu_4NPF_6$ in dichloromethane, referenced to $Cp_2Fe^{+/0}$ at 0 V. [b] Separation between first, second and third oxidations not resolvable.

5.3 Electronic Spectra of the Monocations

The mixed-valence monocations of **1**–**4** were generated in dichloromethane by addition of tris(4-bromophenyl)aminium hexachloroantimonate to an excess of the neutral amine derivative. Visible-NIR absorption spectra of $\mathbf{1}^+$ and $\mathbf{3}^+$ are shown in Figure 5.6. All spectra exhibit an intense band in the visible region that is attributed to a triarylaminium transition. In addition to this strong transition, a weak, broad band in the near-IR region is resolvable for $\mathbf{1}^+$, $\mathbf{3}^+$ and $\mathbf{4}^+$ and is assigned as an intervalence band; the band in $\mathbf{2}^+$ is masked by the triarylaminium absorption.

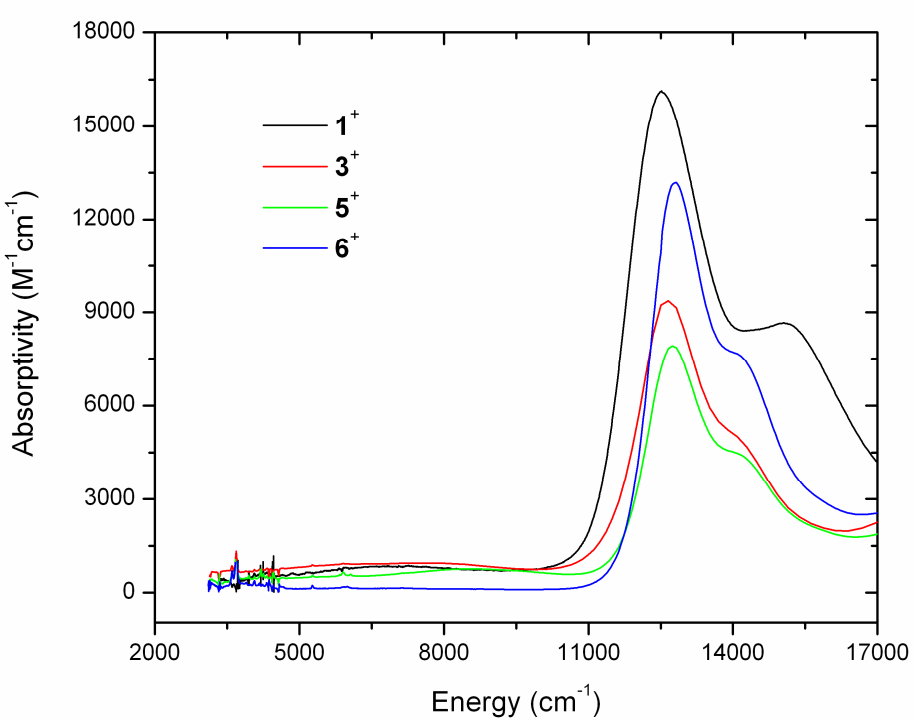

Figure 5.6 Visible-NIR absorption spectra of monocations $\mathbf{1}^+$, $\mathbf{3}^+$, $\mathbf{5}^+$ and $\mathbf{6}^+$ in dichloromethane

The absorptivities of the resolvable intervalence bands, determined assuming complete electron transfer to the oxidizing agent and no disproportionation, are similar for all monocations. In contrast, those of the triarylaminium bands are lower for $\mathbf{3}^+$ than for $\mathbf{1}^+$, which could imply a smaller fraction of fully-oxidized triarylamine centers in the thiophene-based compounds. To test this theory, we calculated the lowest electronic transition for model monocations $\mathbf{I}^+$ (Figure 5.7) and $\mathbf{6}^+$ using time-dependent DFT. As shown in Table 5.2, the energy and oscillator strength of the calculated absorption agrees well with the position and intensity of the experimental absorption. The intensity difference is thus not a mixed-valence effect but is instead due to the properties of the individual redox centers. The absence of a calculated electronic transition in the near-IR

region for the one-center cations also supports the assignment of the near-IR absorption in the three-center cations as an intervalence band.

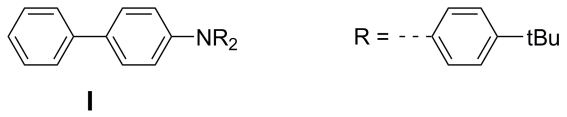

I

Figure 5.7 Structure of compound **I**

Table 5.2 Characteristics of the lowest-energy absorption for model cations $\mathbf{I}^+$ and $\mathbf{6}^+$ according to DFT calculation[a]

Compound	ν_{calc} (cm^{-1})	f_{calc}	Compound	ν_{calc} (cm^{-1})	f_{calc}
$\mathbf{I}^+$	12206	0.3404	$\mathbf{6}^+$	13557	0.2778

[a] Computed with time-dependent DFT at the B3LYP/6-31G(d,p) level.

Monocations of the two-center (**5**) and one-center (**6**) model compounds were generated in the same way as for the three-center compounds. Visible-NIR absorption spectra of $\mathbf{5}^+$ and $\mathbf{6}^+$ are shown in Figure 5.6. The spectrum of $\mathbf{5}^+$ exhibits a weak transition in the near-IR region that is assigned as an intervalence band. The shape of the band is not reliable, however, because of an impurity peak that varies in intensity with the concentration of the monocation. Even so, it is clear that the intervalence band for $\mathbf{5}^+$ occurs at similar energy and intensity as that for $\mathbf{3}^+$. As expected, $\mathbf{6}^+$ has no intervalence band and shows a triarylaminium absorption similar to that observed in $\mathbf{3}^+$ and $\mathbf{5}^+$, which further supports the assignment of the near-IR absorption in $\mathbf{3}^+$ as an intervalence band.

5.4 Electronic Coupling

Due to the overlap of the optical bands, we decomposed the visible-NIR spectra into two Gaussians: one for the triarylaminium absorption and one for the intervalence absorption. The Gaussian used to fit the intervalence band was used for the Hush

analysis of monocations $\mathbf{1}^+$, $\mathbf{3}^+$ and $\mathbf{4}^+$; the lack of a distinct intervalence band precluded such an analysis for $\mathbf{2}^+$ and $\mathbf{5}^+$. Characteristics of the resolvable intervalence bands are collected in Table 5.3. The full width at half maximum predicted by Hush theory ($\nu_{½[Hush]}$) was calculated using Equation 5.1, where ν_{max} is the absorption maximum.[4] The lowest energy features in the spectra of $\mathbf{1}^+$, $\mathbf{3}^+$ and $\mathbf{4}^+$ are broader than the Hush prediction and are symmetric in shape, both of which support the assignment of the bands to the intervalence transitions of class-II compounds.

$$\nu_{1/2[\mathrm{Hush}]} = \sqrt{2310 \times \nu_{\max}} \qquad 5.1$$

Table 5.3 Characteristics of the intervalence bands for $\mathbf{1}^+$, $\mathbf{3}^+$ and $\mathbf{4}^+$

Compound	ν_{max} (cm^{-1})	μ_{ge} (D)	ε_{max} ($M^{-1}cm^{-1}$)	$\nu_{1/2}$ (cm^{-1})	$\nu_{1/2[Hush]}$ (cm^{-1})
$\mathbf{1}^+$	7400	2.8	830	10300	4130
$\mathbf{3}^+$	7100	3.3	910	13000	4050
$\mathbf{4}^+$	6700	3.0	840	10600	3930

The electronic coupling (V) in a mixed-valence compound is related to the intervalence band characteristics through Equation 5.2.[44] In this expression, μ_{ge} is the transition dipole moment, e is the electronic charge and R is the diabatic electron transfer distance. The factor $\sqrt{2}$ is a modification of the original Hush equation that takes into account the three-center nature of the compounds.[23] While we saw before that R is typically smaller than the N–N distance in two-center triarylamines due to delocalization of the charge away from the nitrogen center and into the bridge,[3–25,41] the N–N distance is already shorter than the through-bond distance in the three-center compounds. R was thus taken as R_{NN} in what follows. The electronic coupling values obtained from Hush

analyses of the intervalence bands are collected in Table 5.4. As expected from the lower ionization potential of thiophene relative to benzene, the values of V obtained for $\mathbf{3}^+$ and $\mathbf{4}^+$ are somewhat larger than that found for $\mathbf{1}^+$. However, the electronic coupling differences are smaller than those expected based on our Hush analysis of two-center triarylamines in Chapter 3, where V doubled upon replacing a bridging benzene with thiophene.[25] It is possible that R_{NN} is a poorer approximation of R for $\mathbf{3}^+$ and $\mathbf{4}^+$ than for $\mathbf{1}^+$ because the thiophene-based compounds are likely to have more bridge character. It is also possible that the weak intervalence bands preclude an accurate Hush analysis.

$$V = \frac{\nu_{max}\mu_{ge}}{\sqrt{2}eR} \qquad 5.2$$

Table 5.4 Electronic coupling obtained from Hush analysis and DFT calculation for $\mathbf{1}^+$–$\mathbf{5}^+$

Compound	$R = R_{NN}$ (Å)[a]	V (cm^{-1})[b]	V_{calc} (cm^{-1})[c]
$\mathbf{1}^+$	12.40	250	112
$\mathbf{2}^+$	12.40	–[d]	98
$\mathbf{3}^+$	11.55	300	207
$\mathbf{4}^+$	11.55	260	176
$\mathbf{5}^+$	12.54	–[d]	255

[a] Computed with DFT at the B3LYP/6-31G(d,p) level. [b] From Eq. 5.2. [c] From orbital energy splitting. [d] Intervalence band not resolvable.

Another way to estimate the electronic coupling in a mixed-valence compound is from the energy splitting of orbitals in the corresponding neutral compound, as illustrated in Figure 5.8. For a three-center mixed-valence compound, V is equal to one-third of the energy difference between the HOMO and third-highest occupied orbital (HOMO–2).[45] The electronic coupling estimated in this way from the DFT-computed electronic structure for compounds **1**–**5** is given in Table 5.4. In this case, V_{calc} is indeed twice as

large for $\mathbf{3}^+$ and $\mathbf{4}^+$ than for $\mathbf{1}^+$ and $\mathbf{2}^+$. Both methods of computing *V* indicate that replacement of a bridging phenylene group with a more electron-rich thienylene group increases the electronic coupling between amine centers.

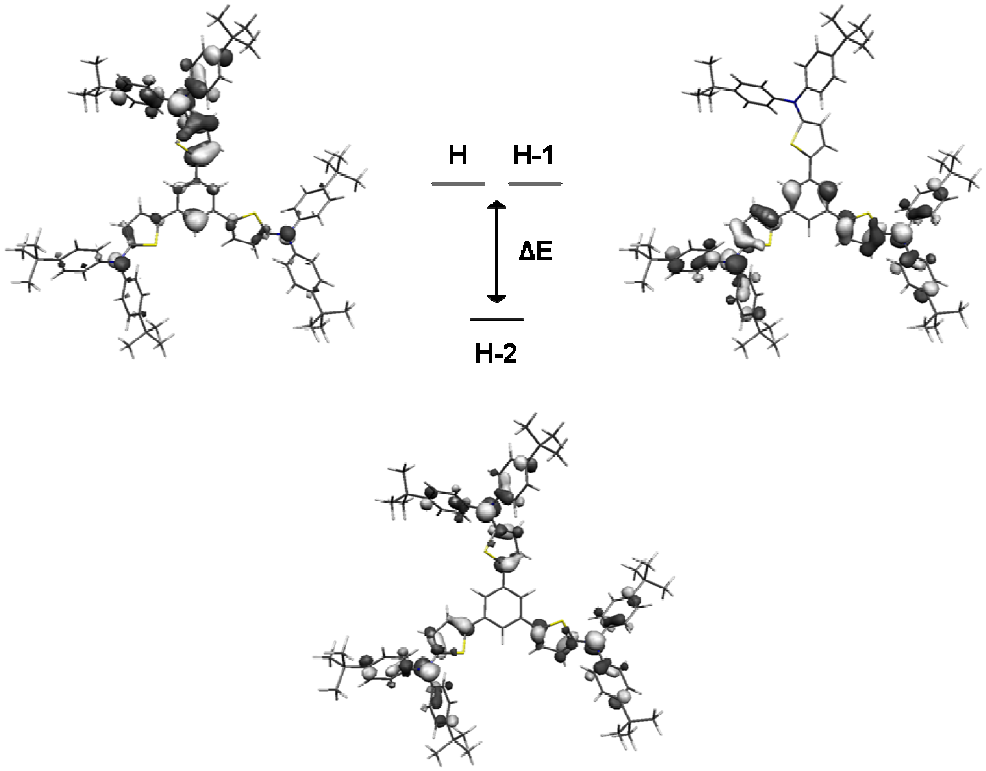

Figure 5.8 Orbital energy splitting in **3** computed using DFT

5.5 Geometry

The neutral geometries of compounds **1**–**6**, as optimized using DFT, reveal another source of the larger electronic coupling in the thienylene-based compounds. While the propeller-like arrangement of aryl groups around the amine center is similar in both types of compounds, the angle between the thiophene unit and the central benzene unit is ca. 10° smaller than the analogous angle for the phenylene-based compounds; this is likely a steric effect of the hydrogen atoms on adjacent benzene rings. One might

predict then that an excess charge localized on a triarylamine can more readily move into the bridging unit in the thiophene compounds. Spin-unrestricted DFT calculations of model cations $\mathbf{I}^+$ and $\mathbf{6}^+$, the results of which are shown in Table 5.5, provide more evidence. While the angle referred to above contracts for both types of compounds upon loss of one electron, an uneven contraction results in an angle ca. 20° smaller in the thienylene-based monocations. The angle between the thiophene unit and the diarylamine is also ca. 10° smaller than the analogous angle in the phenylene-based monocations. The total effect is that the excess charge is more displaced into the bridge in the thiophene monocations.

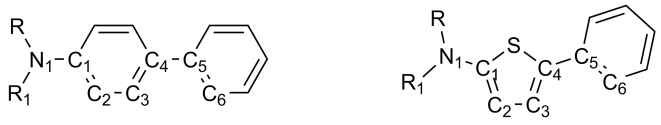

Figure 5.9 Labeling scheme used in Table 5.5

Table 5.5 DFT-computed bond lengths (Å) and dihedral angles for **I** and **6** in their neutral and radical cation states[a]

	I	$\mathbf{I}^+$	Δ	**6**	$\mathbf{6}^+$	Δ
N_1–C_1	1.417	1.403	*–0.014*	1.398	1.359	*–0.039*
C_1–C_2	1.405	1.413	*0.008*	1.374	1.408	*0.034*
C_2–C_3	1.390	1.382	*–0.008*	1.421	1.390	*–0.031*
C_3–C_4	1.405	1.415	*0.010*	1.377	1.402	*0.025*
C_4–C_5	1.483	1.471	*–0.012*	1.467	1.448	*–0.019*
R_1–N_1–C_1–C_2	38.6	34.6	*–4.0*	50.0	20.4	*–29.6*
C_3–C_4–C_5–C_6	36.1	30.3	*–5.8*	27.1	13.1	*–14.0*

[a] Computed at the B3LYP/6-31G(d,p) level.

In the geometry optimization of compound **5**, we opted for a symmetric arrangement of triarylamine centers rather than the one obtained from cutting one arm of the parent compound (**3**). To justify this choice, we compared the total energy of

different configurations: those in which the sulfur atoms of the thiophene groups point in the same or in opposite directions, and those in which the sulfur atoms reside on the same or on opposite sides of the plane formed by the central benzene ring. Rotation had little effect on the energy of **5**, which re-confirms the weak electronic coupling between amine centers in this *meta*-connected compound.

5.6 Electron Spin Resonance Spectra of the Monocations

The ESR spectra of monocations $\mathbf{1}^+$–$\mathbf{6}^+$ were recorded at room temperature in dichloromethane; representative spectra are shown in Figure 5.10. The spectra of $\mathbf{1}^+$ and $\mathbf{2}^+$ are nearly identical in shape and show no resolvable hyperfine splitting. One possibility for the lack of fine structure is *inter*molecular electron transfer: in the fast limit, this is expected to lead to a narrow Lorentzian lineshape and loss of hyperfine coupling.[46] The integrated peaks of the ESR spectra for $\mathbf{1}^+$ and $\mathbf{2}^+$ are Gaussian in shape, however, which rules out this mechanism as the source of broadening. It is possible that no hyperfine splitting is observed because of disproportionation, or because of coupling to a large number of inequivalent ^{1}H nuclei. The room-temperature ESR spectra of $\mathbf{3}^+$ and $\mathbf{4}^+$ differ according to the aryl substituent. While that of $\mathbf{4}^+$ shows no hyperfine splitting, the spectrum of $\mathbf{3}^+$ shows a rich splitting, similar to that seen for an unsubstituted analogue.[47] The integrated peak of the ESR spectrum of $\mathbf{4}^+$ is Gaussian in shape, which again rules out the possibility of intermolecular electron transfer. The ESR spectra of the two-center and one-center monocations, $\mathbf{5}^+$ and $\mathbf{6}^+$, like that of three-center analogue $\mathbf{3}^+$, exhibit multiple resolvable peaks.

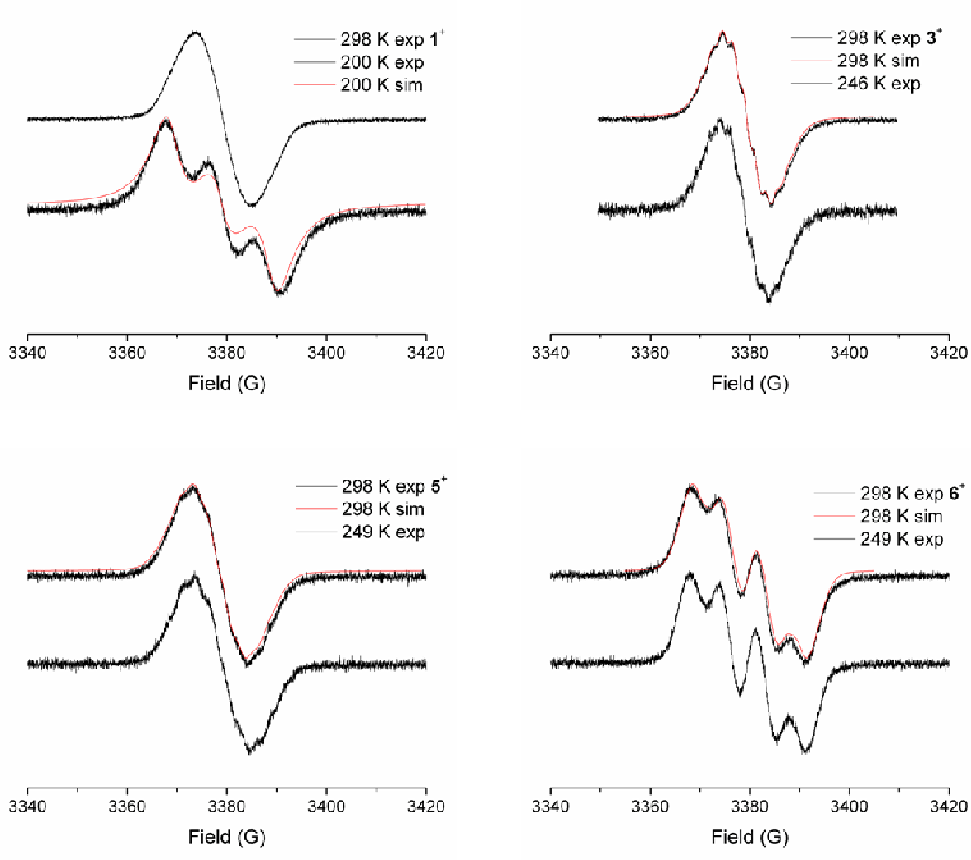

Figure 5.10 Variable-temperature ESR spectra of monocations $\mathbf{1}^+$, $\mathbf{3}^+$, $\mathbf{5}^+$ and $\mathbf{6}^+$ in dichloromethane (black) along with simulations (red)

Variable-temperature ESR spectra of monocations $\mathbf{1}^+$, $\mathbf{3}^+$, $\mathbf{5}^+$ and $\mathbf{6}^+$ were also recorded in dichloromethane. The low temperature spectra are shown in Figure 5.10. When cooled to 200 K, the ESR spectrum of $\mathbf{1}^+$ shows a three-line pattern suggestive of coupling to one nitrogen nucleus; at this temperature, the rate of intramolecular electron transfer is slow on the ESR timescale. The ESR spectra of $\mathbf{3}^+$, however, show no such change in shape. The intensity of the ESR signal diminishes upon cooling – possibly due to decomposition of the monocation over the time required to record the spectra at multiple temperatures – but retains the same shape until below 240 K, where the splitting pattern is lost. This invariance with temperature suggests that the intramolecular electron

transfer is in either a fast or slow limit on the ESR timescale. The ESR spectra of $\mathbf{5}^+$ and $\mathbf{6}^+$ also show little change in shape upon cooling.

The resolvable ESR spectra of $\mathbf{1}^+$, $\mathbf{3}^+$, $\mathbf{5}^+$ and $\mathbf{6}^+$ were simulated in one of two ways to obtain hyperfine coupling values: in *static* simulations,[48–49] the charge was assumed to be either completely localized or completely delocalized; in *dynamic* simulations,[50–51] we assumed that an electron localized on one amine transfers to another amine upon thermal activation. In both cases, spin-unrestricted DFT was used to compute preliminary hyperfine coupling values; the values for model cations $\mathbf{I}^+$ and $\mathbf{6}^+$ are given in Table 5.6.

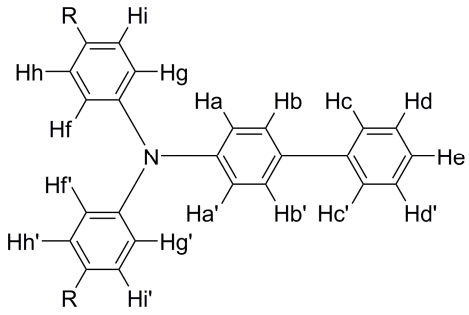

Figure 5.11 Magnetic nuclei for which coupling constants are given in Table 5.6

Table 5.6 Hyperfine coupling constants (G) for $\mathbf{I}^+$ and $\mathbf{6}^+$ obtained from DFT calculations[a]

	$\mathbf{I}^+$	$\mathbf{6}^+$		$\mathbf{I}^+$	$\mathbf{6}^+$
a_N	7.64	6.13	a_{He}	–1.46	–2.88
a_{Ha}	–2.04	–4.63	a_{Hf}	–1.75	–1.06, –1.11
a_{Hb}	0.95	–0.13	a_{Hg}	–1.97	–1.19, –0.99
a_{Hc}	–1.06	–2.20, –2.25[b]	a_{Hh}	1.08	0.70, 0.63
a_{Hd}	0.46	0.91, 0.97	a_{Hi}	1.17	0.84, 0.97

[a] Computed with spin-unrestricted DFT at the B3LYP/6-31G(d,p) level. [b] a_X and $a_{X'}$, respectively.

The three-line ESR spectrum of $\mathbf{1}^+$ at low temperature was initially simulated assuming a static coupling to one ^{14}N (I = 1) nucleus; this, however, gave only a fair fit. A better fit was obtained from a dynamic simulation with a_N = 9.8 G and a thermal exchange rate of 5×10^7 s^{-1}, shown in Table 5.7, indicating that the charge in $\mathbf{1}^+$ is not completely localized on the ESR timescale. The hyperfine splitting is similar to that reported for the tri(*p*-tolyl)amine monocation in acetonitrile (a_N = 9.45 G),[52] but is much larger than that computed by DFT (a_N = 7.64 G) for model cation $\mathbf{I}^+$. The DFT value is likely lowered by over-delocalization of the unpaired electron into the aryl groups.

Table 5.7 Hyperfine coupling constants from simulation of the ESR spectra

		a_N (G)	a_{H1} (G)	a_{H2} (G)	a_{H3} (G)	k_{ET} (s^{-1})
$\mathbf{1}^{+}$[a]	Dynamic	9.8 (1)[b]	–	–	–	5×10^7
	DFT ($\mathbf{I}^+$)	7.64 (1)	–	–	–	–
$\mathbf{3}^+$	Static	1.8 (3)	2.7 (3)	2.3 (3)	–	–
	Dynamic	5.4 (1)	8.1 (1)	6.9 (1)	–	$> 1 \times 10^{10}$
$\mathbf{5}^+$	Static	3.1 (2)	3.6 (2)	2.2 (2)	1.8 (1)	–
	DFT	3.15 (2)	–3.80 (2)	–2.27 (2)	1.36 (1)	–
$\mathbf{6}^+$	Static	6.49 (1)	5.22 (1)	2.44 (1)	–	–
	DFT	6.13 (1)	–4.63 (1)	–2.88 (1)	–	–

[a] From spectra recorded at 200 K; all other spectra at room temperature. [b] Number in parentheses indicates the number of nuclei corresponding to each coupling constant.

The ESR spectra of $\mathbf{6}^+$ illustrate the effect of replacing benzene with the more electron-rich thiophene. The DFT results in Table 5.8 show that such a replacement pulls spin density away from the amine and into the bridge; this results in smaller a_N / larger a_H values for $\mathbf{6}^+$ in comparison to $\mathbf{I}^+$. Indeed, the spin density on the bridging unit in $\mathbf{6}^+$ is so large that hyperfine coupling to hydrogen is comparable to that to nitrogen, and the three-line signature of coupling to one amine is no longer evident. The shape of the room-temperature spectrum for $\mathbf{6}^+$ is reproduced assuming a static coupling to one ^{14}N nucleus

(a_N = 6.49 G) and to two ^{1}H nuclei (a_{H1} = 5.22 G, a_{H2} = 2.44 G). The value of a_N from simulation is again somewhat smaller than that predicted by DFT (a_N = 6.13 G). The large hyperfine coupling to a ^{1}H nucleus is shown by DFT calculation to be the hydrogen atom at the 3-position of the thiophene ring.

Table 5.8 DFT-computed spin densities[a] for different portions of $\mathbf{I}^+$ and $\mathbf{6}^+$

	$\mathbf{I}^+$	$\mathbf{6}^+$
Terminal aryl	0.37	0.19
Amino N atoms	0.32	0.26
Bridging group	0.31	0.56

[a] Computed with spin-unrestricted DFT at the B3LYP/6-31G(d,p) level.

The room-temperature ESR spectrum of $\mathbf{5}^+$ can be simulated assuming a static coupling to two equivalent ^{14}N nuclei (a_N = 3.1 G), two pairs of equivalent ^{1}H nuclei (a_{H1} = 3.6 G, a_{H2} = 2.2 G), and one additional ^{1}H nucleus (a_{H3} = 1.8 G). The charge thus appears delocalized over both amines, which could indicate: 1) that $\mathbf{5}^+$ is a class-III compound; or 2) that the monocation is a localized class-II compound with an exchange rate faster than the ESR timescale. The hyperfine coupling to nitrogen is approximately 1/2 of that obtained from the simulation of $\mathbf{6}^+$; the value of a_N is also consistent with that predicted by DFT calculation (a_N = 3.15 G), which assumes a delocalized charge. Likewise, the room-temperature ESR spectrum of $\mathbf{3}^+$ is well-simulated assuming a static coupling to one set of three equivalent ^{14}N nuclei (a_N = 1.8 G) and two sets of three equivalent ^{1}H nuclei (a_{H1} = 2.7 G, a_{H2} = 2.3 G). The value of a_N is approximately 1/3 of that obtained from the simulation of $\mathbf{6}^+$. As shown in Table 5.7, a dynamic simulation with $k_{ET} > 1 \times 10^{10}$ s^{-1} also gives a good fit to the spectrum when the number of equivalent nuclei is cut by three and the hyperfine coupling values are tripled. This,

combined with the invariance of the variable-temperature ESR spectra, indicates that both $\mathbf{3}^+$ and $\mathbf{5}^+$ are in the fast limit of thermal electron transfer on the ESR timescale.

5.7 Comparison of Electron Transfer Parameters

Because $\mathbf{1}^+$ and $\mathbf{3}^+$ exhibit resolvable intervalence bands and resolvable ESR spectra, two experimental methods exist by which to extract the thermal electron transfer rates in the three-center triarylamines. Comparison of the rates in turn reveals the nature of the intramolecular electron transfer process. We saw in Chapter 2 that, depending on the interplay between the nuclear and electronic frequencies, electron transfer reactions are categorized as adiabatic or nonadiabatic; these two regimes differ in the prefactor, A, which is determined in limiting cases by the dynamic properties of the slower subsystems.[26] In a nonadiabatic electron transfer reaction, the electronic motion is slower than the vibrational motion and the prefactor is a function of the electronic (V) and vibronic (λ) coupling, as shown in Equation 5.3. In the adiabatic regime, the vibrational motion is slower than the electronic motion, and A is given by Equation 5.4, where ν_n is the nuclear frequency of crossing the electron transfer barrier.

$$A = V^2 \sqrt{\frac{4\pi^3}{h^2 \lambda k_B T}} \qquad 5.3$$

$$A = \nu_n \qquad 5.4$$

Our study of *para*-connected two-center triarylamines in Chapter 4 showed that the thermal electron transfer in such systems occurs in the adiabatic regime.[41] This was as expected from classical electron transfer theory due to the strong electronic coupling ($V >> 200$ cm^{-1}) between the redox centers. The magnitude of V in the *meta*-connected

three-center triarylamines is, however, on the order of this threshold value, and as such, one might no longer predict adiabatic electron transfer. As shown in Table 5.9, the electron transfer rates obtained by inserting the Hush values of V and λ into Equation 5.3 compare well with those obtained from the dynamic ESR simulations of $\mathbf{1}^+$ and $\mathbf{3}^+$. Even better agreement is achieved by using the DFT-computed electronic coupling values. While Equation 5.4 precludes such a substitution, we note that the nonadiabatic prefactors ($A \approx 10^{13}$ s^{-1}), which match experiment well, exceed the range of expected values for solvent reorientation frequencies ($\nu_n \approx 10^{11}$–10^{12} s^{-1}).[26] It appears then that the weak electronic coupling in the *meta*-connected compounds pushes the thermal electron transfer into the nonadiabatic regime, in contrast to the adiabatic electron transfer seen for *para*-connected analogues. This study is the first to suggest that, by changing the relative position of redox centers around a central benzene unit, one can alter the mechanism of intramolecular electron transfer in mixed-valence triarylamines.

Table 5.9 Rate constants obtained from intervalence band analysis and ESR simulation

Compound	T (K)	ΔG^* (cm^{-1})[a]	A (s^{-1})[b]	k_{ET} (s^{-1})[c]	k_{ET} (s^{-1})[d]
$\mathbf{1}^+$	200	1610[e] 1740	2.1×10^{13} 4.1×10^{12}	1.9×10^{8} 1.5×10^{7}	5×10^{7}
$\mathbf{3}^+$	298	1490 1570	2.5×10^{13} 1.2×10^{13}	1.9×10^{10} 5.9×10^{9}	$> 1 \times 10^{10}$

[a] From Eq. 2.2. [b] From Eq. 5.3. [c] From Eq. 2.1. [d] From dynamic ESR simulation. [e] Top value is computed with V from Hush analysis; bottom is computed using V_{calc}.

REFERENCES

[1] Robin, M. B.; Day, P. *Adv. Inorg. Chem. Radiochem.* **1967**, *10*, 247.

[2] Hush, N. S. *Prog. Inorg Chem.* **1967**, *8*, 391.

[3] Lambert, C.; Nöll, G. *Angew. Chem. Int. Ed.* **1998**, *37*, 2107.

[4] Lambert, C.; Nöll, G. *J. Am. Chem. Soc.* **1999**, *121*, 8434.

[5] Coropceanu, V.; Malagoli, M.; André, J. M.; Brédas, J.-L. *J. Chem. Phys.* **2001**, *115*, 10409.

[6] Coropceanu, V.; Malagoli, M.; André, J. M.; Brédas, J.-L. *J. Am. Chem. Soc.* **2002**, *124*, 10519.

[7] Lambert, C.; Nöll, G.; Schelter, J. *Nat. Mater.* **2002**, *1*, 69.

[8] Coropceanu, V.; Lambert, C.; Nöll, G.; Brédas, J.-L. *Chem. Phys. Lett.* **2003**, *373*, 153.

[9] Coropceanu, V.; André, J. M.; Malagoli, M.; Brédas, J.-L. *Theor. Chem. Acc.* **2003**, *110*, 59.

[10] Lambert, C.; Amthor, S.; Schelter, J. *J. Phys. Chem. A* **2004**, *108*, 6474.

[11] Low, P. J.; Paterson, M. A. J.; Puschmann, H.; Goeta, A. E.; Howard, J. A. K.; Lambert, C.; Cherryman, J. C.; Tackley, D. R.; Leeming, S.; Brown, B. *Chem. Eur. J.* **2004**, *10*, 83.

[12] Szeghalmi, A. V.; Erdmann, M.; Engel, V.; Schmitt, M.; Amthor, S.; Kriegisch, V.; Nöll, G.; Stahl, R.; Lambert, C.; Leusser, D.; Stalke, D.; Zabel, M.; Popp, J. *J. Am. Chem. Soc.* **2004**, *126*, 7834.

[13] Jones, S. C.; Coropceanu, V.; Barlow, S.; Kinnibrugh, T.; Timofeeva, T.; Brédas, J.-L.; Marder, S. R. *J. Am. Chem. Soc.* **2004**, *126*, 11782.

[14] Barlow, S.; Risko, C.; Coropceanu, V.; Tucker, N. M.; Jones, S. C.; Levi, Z.; Khrustalev, V. N.; Antipin, M. Y.; Kinnibrugh, T. L.; Timofeeva, T.; Marder, S. R.; Brédas, J.-L. *Chem. Commun.* **2005**, 764.

[15] Barlow, S.; Risko, C.; Chung, S.-J.; Tucker, N. M.; Coropceanu, V.; Jones, S. C.; Levi, Z.; Brédas, J. L.; Marder, S. R. *J. Am. Chem. Soc.* **2005**, *127*, 16900.

[16] Lambert, C.; Risko, C.; Coropceanu, V.; Schelter, J.; Amthor, S.; Gruhn, N. E.; Durivage, J. C.; Brédas, J. L. *J. Am. Chem. Soc.* **2005**, *127*, 8508.

[17] Coropceanu, V.; Boldyrev, S. I.; Risko, C.; Brédas, J.-L. *Chem. Phys.* **2006**, *326*, 107.

[18] Amthor, S.; Lambert, C. *J. Phys. Chem. A* **2006**, *110*, 1177.

[19] Amthor, S.; Lambert, C. *J. Phys. Chem. A* **2006**, *110*, 3495.

[20] Rohde, D.; Dunsch, L.; Tabet, A.; Hartmann, H.; Fabian, J. *J. Phys. Chem. B* **2006**, *110*, 8223.

[21] Nöll, G.; Avola, M.; Lynch, M.; Daub, J. *J. Phys. Chem. C* **2007**, *111*, 3197.

[22] Nöll, G.; Amthor, S.; Avola, M.; Lambert, C.; Daubl, J. *J. Phys. Chem. C* **2007**, *111*, 3512.

[23] Bonvoisin, J.; Launay, J.-P.; Van der Auweraer, M.; De Schryver, F. C. *J. Phys. Chem.* **1994**, *98*, 5052; correction, *J. Phys. Chem.* **1996**, *100*, 18006.

[24] Bonvoisin, J.; Launay, J.-P.; Verbouwe, W.; Van der Auweraer, M.; De Schryver, F. C. *J. Phys. Chem.* **1996**, *100*, 17079.

[25] Odom, S. A.; Lancaster, K.; Beverina, L.; Lefler, K. M.; Thompson, N. J.; Coropceanu, V.; Brédas, J.-L.; Marder, S. R.; Barlow, S. *Chem. Eur. J.* **2007**, *13*, 9637.

[26] Sutin, N. *Prog. Inorg. Chem.* **1983**, *30*, 441.

[27] Rak, S. F.; Miller, L. L. *J. Am. Chem. Soc.* **1992**, *114*, 1388.

[28] Bonvoisin, J.; Launay, J.-P.; Rovira, C.; Veciana, J. *Angew. Chem. Int. Ed. Engl.* **1994**, *33*, 2106.

[29] Nelsen, S. F.; Ramm, M. T.; Wolff, J. J.; Powell, D. R. *J. Am. Chem. Soc.* **1997**, *119*, 6863.

[30] Nelsen, S. F.; Trieber, D. A.; Wolff, J. J.; Powell, D. R.; Rogers-Crowley, S. *J. Am. Chem. Soc.* **1997**, *119*, 6873.

[31] Nelsen, S. F.; Ismagilov, R. F.; Powell, D. R. *J. Am. Chem. Soc.* **1997**, *119*, 10213.

[32] Nelsen, S. F.; Ismagilov, R. F.; Trieber, D. A. *Science* **1997**, *278*, 846.

[33] Rovira, C; Ruiz-Molina, D.; Elsner, O.; Vidal-Gancedo, J.; Bonvoisin, J.; Launay, J.-P.; Veciana, J. *Chem. Eur. J.* **2001**, *7*, 240.

[34] Lindeman, S. V.; Rosokha, S. V.; Sun, D.; Kochi, J. K. *J. Am. Chem. Soc.* **2002**, *124*, 843.

[35] Rosokha, S. V.; Sun, D.-L.; Kochi, J. K. *J. Phys. Chem. A* **2002**, *106*, 2283.

[36] Sun, D.-L.; Rosokha, S. V.; Lindeman, S. V.; Kochi, J. K. *J. Am. Chem. Soc.* **2003**, *125*, 15950.

[37] Sun, D.; Rosokha, S. V.; Kochi, J. K. *J. Am. Chem. Soc.* **2004**, *126*, 1388.

[38] Hirao, Y.; Urabe, M.; Ito, A.; K. Tanaka, 46, 3300 *Angew. Chem. Int. Ed.* **2007**, *46*, 3300.

[39] Stickley, K. R.; Blackstock, S. C. *J. Am. Chem. Soc.* **1994**, *116*, 11576.

[40] Stickley, K. R.; Blackstock, S. C. *Tetrahedron Lett.* **1995**, *36*, 1585.

[41] Lancaster, K.; Odom, S. A.; Jones, S. C.; Thayumanavan, S.; Marder, S. R.; Brédas, J.-L.; Coropceanu, V.; Barlow, S. *J. Am. Chem. Soc.* **2009**, *131*, 1717.

[42] Åsbrink, L.; Lindholm, E.; Edqvist, O. *Chem. Phys. Lett.* **1970**, *5*, 609.

[43] Sell, J. A.; Kuppermann, A. *Chem. Phys. Lett.* **1979**, *61*, 355.

[44] Creutz, C.; Newton, M. D.; Sutin, N. *J. Photochem. Photobiol. A: Chem.* **1994**, *82*, 47.

[45] Launay, J. P.; Babonneau, F. *Chem. Phys.* **1982**, *67*, 295.

[46] Veregin, R. P.; Harbour, J. R. *J. Phys. Chem.* **1990**, *94*, 6231.

[47] Rapta, P.; Tabet, A.; Hartmann, H.; Dunsch, L. *J. Mater. Chem.* **2007**, *17*, 4998.

[48] Duling, D. R. *J. Magn. Reson. Ser. B* **1994**, *104*, 105.

[49] http://www.niehs.nih.gov/research/resources/software/tools/index.cfm.

[50] Heinzer, J. *Mol. Phys.* **1971**, *22*, 167.

[51] Heinzer, J. *Quantum Chemistry Program Exchange* **1972**, *No. 209.*

[52] Seo, E. T.; Nelson, R. F.; Fritsch, J. M.; Marcoux, L. S.; Leedy, D. W.; Adams, R. N. *J. Am. Chem. Soc.* **1966**, *88*, 3498.

CHAPTER 6

INTRAMOLECULAR ELECTRON TRANSFER IN FOUR-CENTER CLASS-II+III MIXED-VALENCE TRIARYLAMINES

6.1 Organic High-Spin Compounds

The focus of the previous chapter was on mixed-valence triarylamines in which the centers are connected through *meta*-substituted phenylene bridges. The fully-oxidized forms of the *meta*-connected triarylamines are also of interest as organic high-spin materials,[1,2] for they are isoelectronic with non-Kekulé hydrocarbons.[3] To understand why compounds such as those in Figure 6.1 are high-spin, we outline two qualitative methods for predicting the ground spin states of diradicals below.

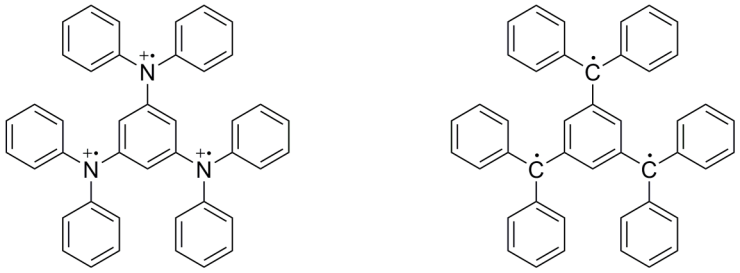

Figure 6.1 A non-Kekulé hydrocarbon (right) and its triarylamine analogue (left)

The first method is that of Ovchinnikov.[4] In this valence bond approach, the ground state is the one which gives the maximum number of π bonds. To determine this number, the conjugated atoms are alternately labeled n^* and n such that no two atoms of the same label are directly linked and $n^* > n$. Ovchinnikov proved that the ground state of such an alternant hydrocarbon has a total spin quantum number $S = (n^* - n)/2$. Thus, the *meta*-connected diradical in Figure 6.2 is predicted to be a ground state triplet.

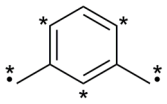

Figure 6.2 Example of the valence bond approach

The other method is based on molecular orbital theory.[5] In this approach, the ground state of a diradical depends on the nature of its singly-occupied orbitals. In a "disjoint" diradical, the singly-occupied orbitals are spatially distinct. There is no direct communication between the spins and thus the singlet and triplet states are degenerate. In a "non-disjoint" diradical, the singly-occupied orbitals overlap in their spatial distributions. There is then a strong exchange interaction which stabilizes the triplet over the singlet state. As shown in Figure 6.3, the singly-occupied orbitals of the *meta*-connected compound are non-disjoint; the molecular orbital approach thus also predicts a triplet ground state for the diradical.

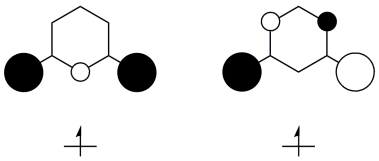

Figure 6.3 Example of the molecular orbital approach

In contrast to the *para*-connected compounds of earlier chapters, the *meta*-connected compounds are relatively unstable at room temperature. One way to stabilize the compound is to replace the amine centers with mixed-valence triarylamines. The resultant delocalization of charge in the centers stabilizes the system without affecting the spin alignment. Many compounds with the motif shown in Figure 6.4 are synthesized, and the optical electron transfer in the oxidized species can be analyzed using Hush

theory.[6] In so doing, however, one must recognize that the monocation is a weakly coupled (class-II) mixed-valence system in which the centers are strongly coupled (class-III) mixed-valence systems.[7] The optical electron transfer is thus a combination of intervalence transitions *between* the amine centers as well as *within* the amine centers. The former are expected to be quite weak, while the latter are expected to dominate.

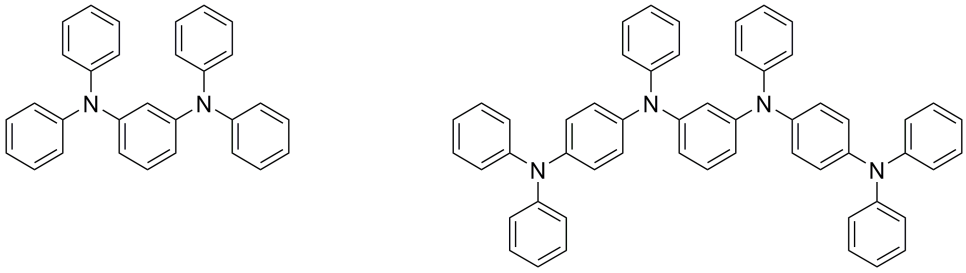

Figure 6.4 A two-center triarylamine (left) and its four-center counterpart (right)

6.2 Four-Center Class-II+III Triarylamines

Compounds that contain two *p*-phenylenediamine units connected by a *m*-phenylene unit give high spin states upon oxidation. Delocalization of the unpaired electron within each *p*-phenylenediamine unit affords chemical stability, while the topology of the connecting *m*-phenylene rings affords ferromagnetic spin alignment between the *p*-phenylenediamine units. While the compounds are mainly of interest for their doubly-oxidized, high-spin states, we focus on the singly-oxidized, mixed-valence state in what follows.

6.2.1 Effect of Meta Connection

Before we move on to four-center triarylamines, we first examine the effect of connectivity on mixed-valence compounds with only two redox centers. In particular, we compare the ESR spectra of cations $\mathbf{A}^+$ and $\mathbf{B}^+$, the structures of which are shown in

Figure 6.5. In one case, the amine centers are connected through a *para*-substituted biphenyl bridge,[8] while in the other case, the centers are *meta*-connected.[9]

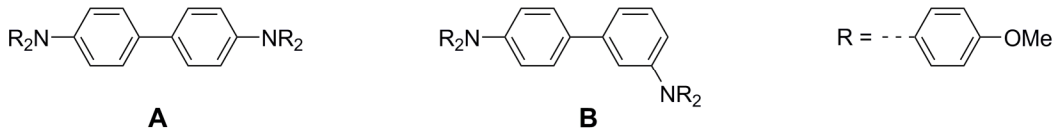

Figure 6.5 Structure of compounds **A** and **B**

In the first chapter, we saw that the mixed-valence cation of **A** belongs to Robin and Day's class-III; that is, the unpaired electron is delocalized over both redox centers.[10] One would thus expect the ESR spectrum of $\mathbf{A}^+$ to show hyperfine coupling to two equivalent ^{14}N nuclei at all temperatures. In contrast, the ESR spectrum of $\mathbf{B}^+$ in Figure 6.6 shows a splitting to a single ^{14}N nucleus with a_N = 9.1 G together with many small splittings ($a_H \approx 0.5$ G) due to the aromatic hydrogens.[9] The unpaired electron in $\mathbf{B}^+$ is thus localized on one triarylamine center on the ESR timescale. The different ESR behaviors of $\mathbf{A}^+$ and $\mathbf{B}^+$, which differ only in the placement of redox centers about a biphenyl bridge, is consistent with the non-resonant nature of *meta*-connections.

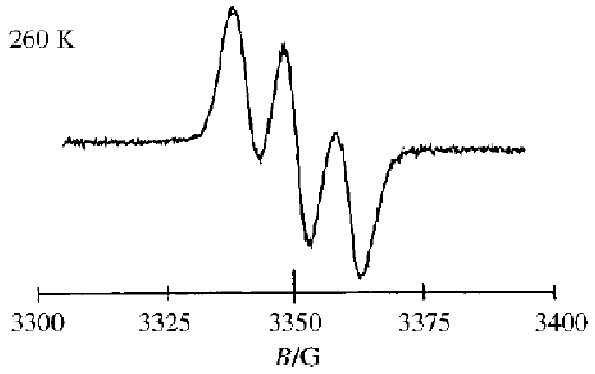

Figure 6.6 ESR spectrum for $\mathbf{B}^+$ at 260 K obtained upon chemical oxidation in dichloromethane[9]

6.2.2 Effect of Phenyl vs. Naphthyl Connection

We return now to the four-center class-II+III triarylamines. The first compound with such a motif was synthesized by Wienk and Janssen.[11,12] The goal was to observe a stable triplet diradical dication, but some work was also done on the intermediate oxidation state. The structure of **1** is shown in Figure 6.7.

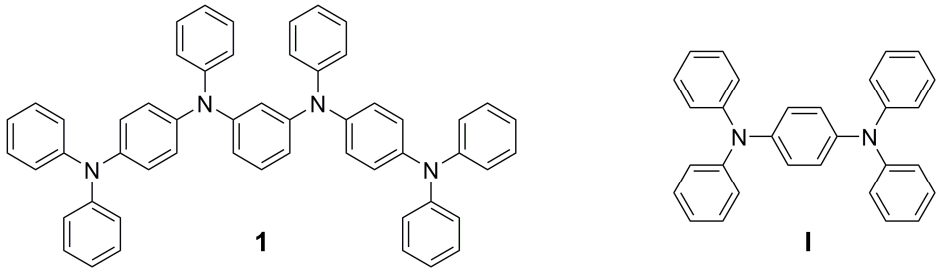

Figure 6.7 Structure of compounds **1** and **I**

The ESR spectrum of $\mathbf{1}^+$ was recorded at room temperature after chemical oxidation in dichloromethane. As shown in Figure 6.8, this gave a poorly resolved nine-line spectrum due to hyperfine coupling to four ^{14}N nuclei with $a_N \approx 3$ G.[12] This pattern suggests that a fast intramolecular electron transfer occurs between the neutral and singly-oxidized *p*-phenylenediamine units. The electron transfer can be suppressed by lowering the temperature or by addition of acid. The latter results in a five-line ESR spectrum due to hyperfine coupling to only two ^{14}N nuclei with $a_N = 5.7$ G,[12] similar to the value of 5.8 G reported for the radical cation of **I** in acetonitrile.[13] The interaction with two ^{14}N nuclei suggests that the unpaired electron is localized on only one of the phenylenediamine units. When the acidified sample is heated, the nine-line pattern reappears,[12] indicating that the electron transfer is a thermally activated process.

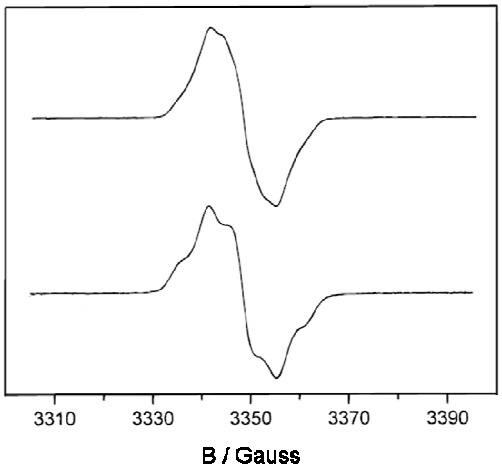

Figure 6.8 Room-temperature ESR spectra for $\mathbf{1}^{+}$ obtained upon chemical oxidation in dichloromethane (top) or by addition of acid (bottom)[12]

The absorption spectrum of **1** was also recorded upon chemical oxidation in dichloromethane. As shown in Figure 6.9, a new band appears at 11600 cm^{-1} (1.44 eV), similar to the intervalence band seen for the class-III mixed-valence cation of **I**.[14] This band reaches maximum intensity after two equivalents of oxidant are added.[12] Another band appears in the near-IR region around 7000 cm^{-1} (0.9 eV) and is attributed to an intervalence transition between the neutral and singly-oxidized *p*-phenylenediamine units. This band reaches maximum intensity after one equivalent of oxidant is added.[12] Unfortunately, a Hush analysis is not possible due to the low intensity and partial overlap with the much stronger intervalence absorption of the *p*-phenylenediamine unit.

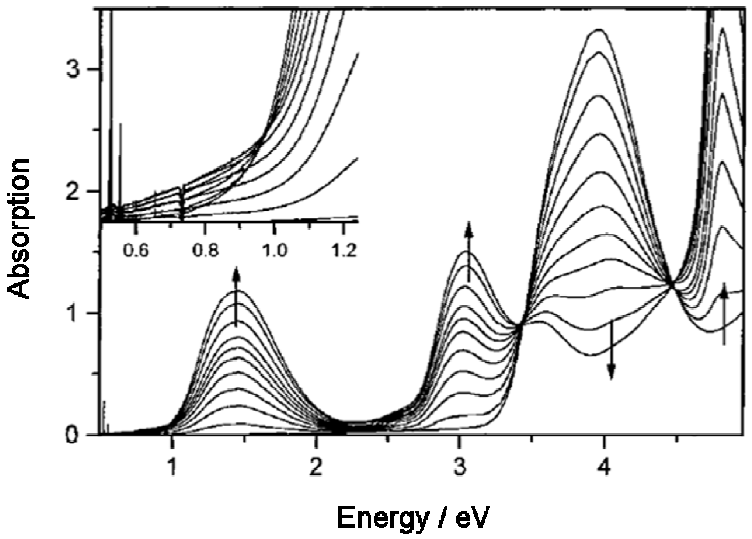

Figure 6.9 UV-visible-NIR absorption spectra of the stepwise oxidation of **1** in dichloromethane at 295 K; inset shows enlarged near-IR region[12]

Not long after the work of Wienk and Janssen, Selby and Blackstock made a similar compound in which the amine centers were connected through a *meta*-substituted naphthyl bridge.[15] The goal, again, was to observe the triplet diradical dication, but some work was also done on the monocation. The structure of **2** is shown in Figure 6.10, along with that of two-center analogue **II**.

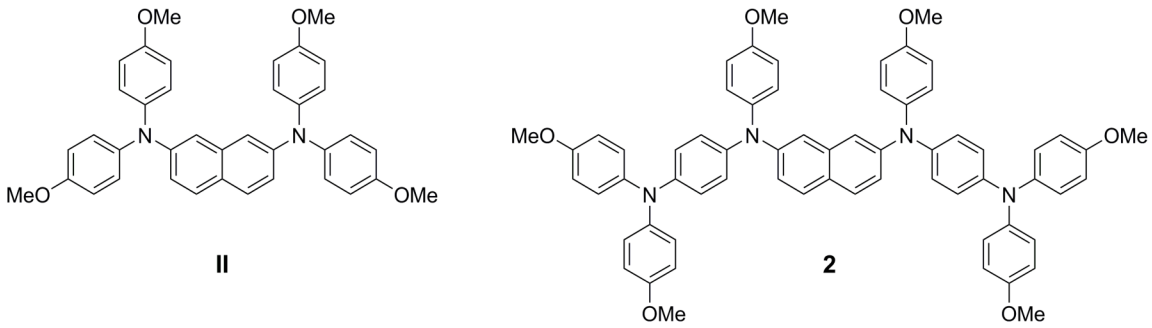

Figure 6.10 Structure of compounds **II** and **2**

The radical cations of **2** and **II** were generated by chemical oxidation in dichloromethane. The ESR spectrum of $\mathbf{II}^+$ was recorded at room temperature and showed a broad five-line pattern (Figure 6.11). The authors attributed this pattern to hyperfine coupling to two equivalent ^{14}N nuclei with a_N = 4.6 G.[15] Then again, the spectrum of $\mathbf{II}^+$ is reminiscent of that expected for a two-center triarylamine with an electron transfer rate comparable to the ESR timescale; i.e., the first peak of the five-line spectrum is higher than the second. The anomalous hyperfine pattern of $\mathbf{II}^+$ suggests that the unpaired electron is in fact localized on one triarylamine, and thus that the mixed-valence monocation belongs to Robin and Day's class-II.

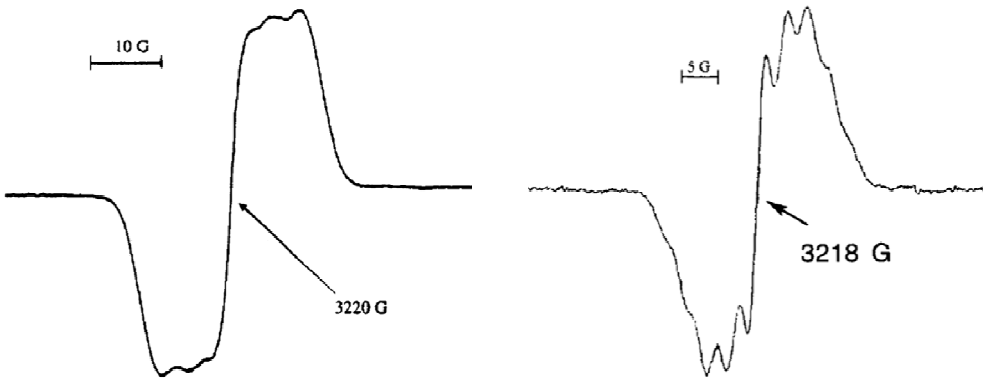

Figure 6.11 Room-temperature ESR spectra for $\mathbf{II}^+$ and $\mathbf{2}^+$ obtained upon chemical oxidation in dichloromethane[15]

The ESR spectrum of $\mathbf{2}^+$ was also recorded at room temperature and showed a broad nine-line pattern (Figure 6.11), consistent with nearly equal spin density on all four ^{14}N nuclei.[15] This ESR signature could arise from either: 1) delocalization of the unpaired electron, or 2) fast intramolecular electron transfer between the neutral and singly-oxidized *p*-phenylenediamine units. Indeed, we find that the spectrum can be simulated equally well assuming the former with $a(4N) \approx 3$ G, or the latter with $a(2N) \approx$

6 G and $k_{ET} > 10^{10}$ s^{-1}. Given that the ESR spectrum of $\mathbf{II}^+$ shows thermally activated electron transfer, the latter interpretation seems more likely.

6.2.3 Effect of End Groups

In the previous section, we saw that *meta*-connections around both phenyl and naphthyl bridges afford weakly coupled mixed-valence compounds with thermal electron transfer rates faster than the ESR timescale. The intervalence bands, however, are either too weak for Hush analysis or, as in the case of $\mathbf{2}^+$, not reported. One thus cannot compare the electronic coupling through phenyl vs. naphthyl bridges. The electron-richness of the end groups could also effect the interaction between centers; we examine this effect here. In particular, we study an analogue of **1** in which the phenyl end groups are replaced by methyl groups,[16] giving compound **3** in Figure 6.12.

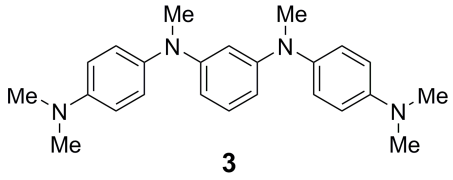

3

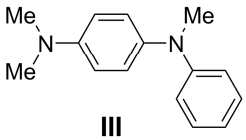

III

Figure 6.12 Structure of compounds **3** and **III**

The ESR spectrum of $\mathbf{3}^+$ was recorded at 123 K after chemical oxidation in butyronitrile; the spectrum shows a poorly resolved six-line pattern due to interaction with the ^{14}N and ^{1}H nuclei of the *N*-methyl groups.[16] Although isotropic hyperfine coupling constants cannot be determined in frozen solution, the unpaired spin in $\mathbf{3}^+$ appears to be localized on only one of the phenylenediamine units because the same ESR spectrum is obtained upon one-electron oxidation of **III**.[16] The thermal electron transfer

in $\mathbf{3}^+$ is thus slow on the ESR timescale at low temperature, while its analogue $\mathbf{1}^+$ is in the fast regime at room temperature.

Like many of the other class-II+III triarylamines, the absorption spectrum of $\mathbf{3}^+$ was not recorded. One might expect the intervalence band associated with optical electron transfer *between* the *p*-phenylenediamine units to overlap with the much stronger intervalence absorption *within* the *p*-phenylenediamine units, as was the case for $\mathbf{1}^+$; however, one must also take into account the effect of the different end groups. As shown in Figure 6.13, the intervalence transition in *p*-phenylenediamine occurs at much higher energy when anisyl end groups[8] are replaced by methyl groups[17]. This blue-shift could prevent overlap of the class-III transition with the class-II transition in $\mathbf{3}^+$, and thus allow one to perform a Hush analysis on the latter.

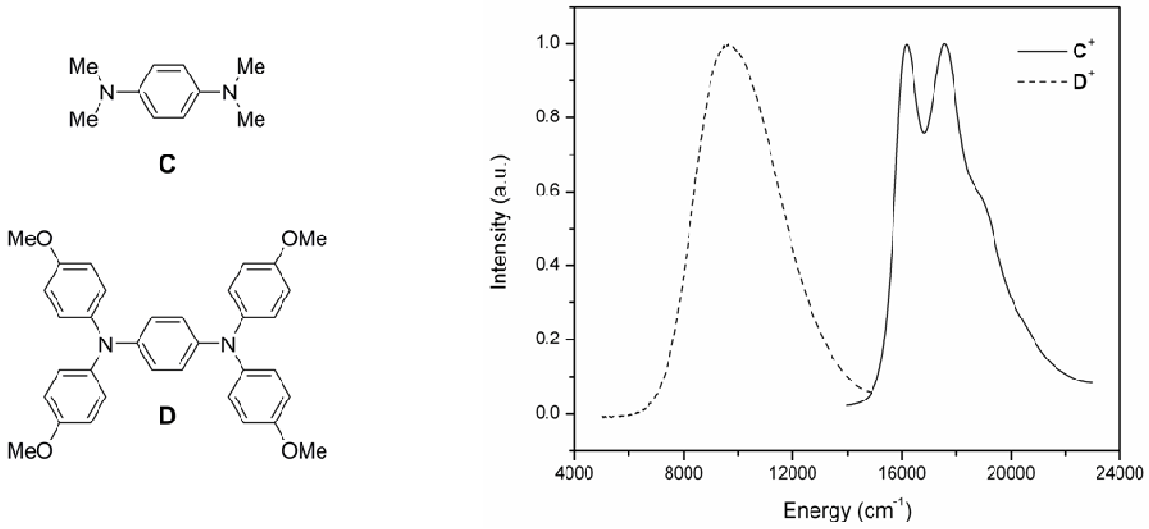

Figure 6.13 Structure of compounds **C** and **D** and normalized visible-NIR absorption spectra of the corresponding monocations[8,17]

6.2.4 Effect of Double Connection

The four-center class-II+III triarylamines seen thus far can exist as a mixture of conformers due to the flexibility about the *m*-phenylene bridge. This situation may cause an overlap of the ESR spectra, leading to no definite fine structure. One way to limit conformational freedom is by cyclization;[18–20] examples of such compounds are shown in Figure 6.14. In this section, we examine the effect of this double connection on the corresponding monocations.

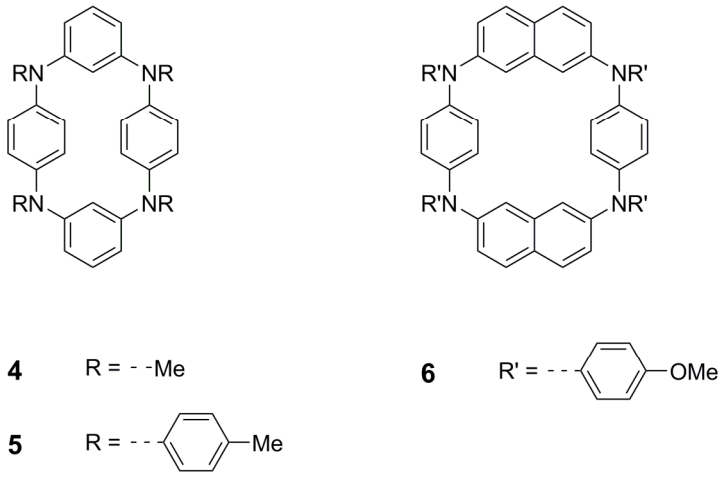

Figure 6.14 Examples of doubly-connected four-center triarylamines

The radical cations of **4**–**6** were generated by chemical oxidation. Because the goal of each study was to determine the ground spin state of the dication, all ESR spectra were obtained in frozen solution. Thus, it was not possible to determine isotropic hyperfine coupling constants for the monocations. The ESR spectrum of $\mathbf{4}^{+}$ was obtained at 116 K in butyronitrile and showed a poorly resolved hyperfine structure resulting from ^{14}N and ^{1}H nuclei at the *N*-methyl groups.[18] The *g* value suggested fairly large spin densities at the *p*-phenylene units. No fine structure was observed in the ESR spectrum

of $\mathbf{6}^+$ in dichloromethane over a large concentration and temperature range,[19] but the ESR spectrum of $\mathbf{5}^+$ obtained at 20 K in the same solvent displayed nitrogen hyperfine splittings.[20] It is clearly of interest to record the ESR spectra of the radical cations in fluid solution to evaluate the spin distribution in the mixed-valence state.

The absorption spectrum of **5** was also recorded upon chemical oxidation in dichloromethane.[20] As shown in Figure 6.15, a new band appears in the near-IR region with a maximum greater than 800 nm. This band can be attributed to the class-III intervalence transition of the *p*-phenylenediamine cation. The class-II intervalence transition between the neutral and singly-oxidized *p*-phenylenediamine units was not observed, due to overlap with the class-III transition or to a maximum at longer wavelengths than that recorded.

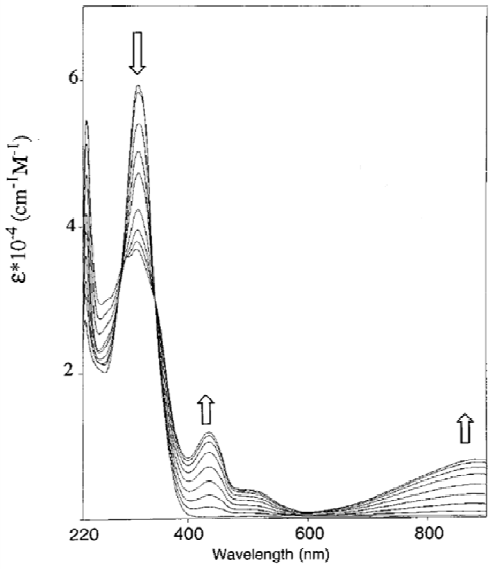

Figure 6.15 UV-visible-NIR absorption spectra of the stepwise oxidation of **5** in dichloromethane[20]

A similar study was done by Yan et al. on a longer analogue of **5**.[21] As shown in Figure 6.16, chemical oxidation of "ladder" compound **IV** generated an absorption band at 1050 nm. This band reached maximum intensity after the addition of two equivalents of oxidant, corresponding to one-electron oxidation of the outer rungs of the ladder.[21] The authors, however, attributed the absorption at long wavelengths to an intervalence transition *between* neutral and singly-oxidized *p*-phenylenediamine units rather than the well-known intervalence transition *within p*-phenylenediamine cations. Indeed, as shown in Table 6.1, the characteristics of the intervalence band for $\mathbf{IV}^+$ are strikingly similar to those of $\mathbf{D}^+$.[8] This erroneous assignment led Yan et al. to conclude that the electronic coupling between rungs is comparable to that within rungs.[21]

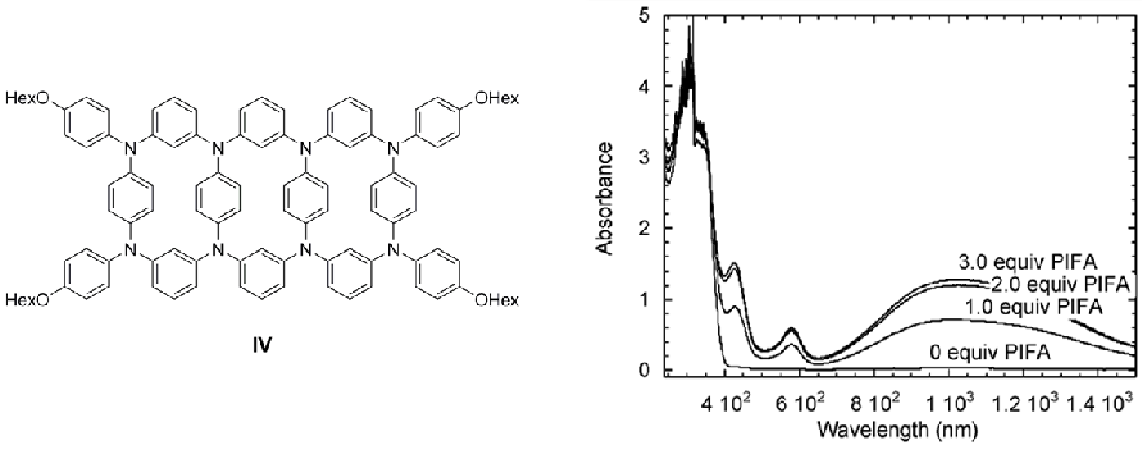

Figure 6.16 UV-visible-NIR absorption spectra of the stepwise oxidation of **IV** in dichloromethane using phenyliodine(III) bis(trifluoroacetate), or PIFA[21]

Table 6.1 Characteristics of the intervalence bands for $\mathbf{D}^+$ and $\mathbf{IV}^+$

Compound	ν_{max} (cm^{-1})	$\Delta\nu_{½}$ (cm^{-1})
$\mathbf{D}^{+[a]}$	9530	4680
$\mathbf{IV}^{+[b]}$	9520	4700

From: [a] Ref. 8; [b] Ref. 21.

More evidence is provided by the visible-NIR absorption spectra of $\mathbf{7}^{+}$,[22] shown in Figure 6.17. In this example, the *p*-phenylenediamine units are connected through a saturated, trimethylene bridge. The band near 16000 cm^{-1} in the spectrum of $\mathbf{7}^{+}$ is similar to that seen for $\mathbf{C}^{+}$ in Figure 6.13; this band can be attributed to the excitation within a singly-oxidized *p*-phenylenediamine unit.[17] The blue-shift of this class-III transition reveals the much weaker class-II transition between the neutral and singly-oxidized *p*-phenylenediamine units at 5800 cm^{-1}. The dication $\mathbf{7}^{2+}$ shows no such intervalence band, as expected.

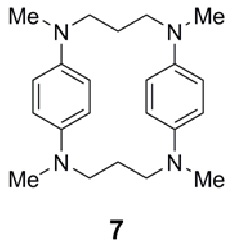

7

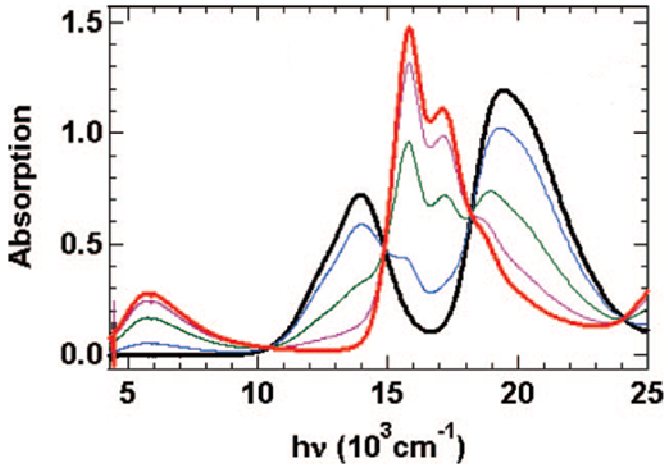

Figure 6.17 Visible-NIR absorption spectra of the stepwise oxidation of $\mathbf{7}^{+}$ (red) in dichloromethane to $\mathbf{7}^{2+}$ (black)[22]

6.3 Updates and Outlook

This chapter is largely a treatise on what we envision as the future of mixed-valence chemistry. In that regard, we now revisit the results of earlier chapters from the viewpoint of recent studies that corroborate our conclusions, or have the potential to extend our work.

6.3.1 Two-Center Class-III Triarylamines

In Chapter 3, we saw how the energy of the bridge affects electron delocalization in a mixed-valence compound. By replacing a bridging benzene with a less aromatic and more easily oxidized heterocycle, we increased both the electronic coupling between redox centers and the spin density on the bridge.[23] In work that is soon to be published, Barlow et al. find the same effect for the two-center triarylamines in Figure 6.18.

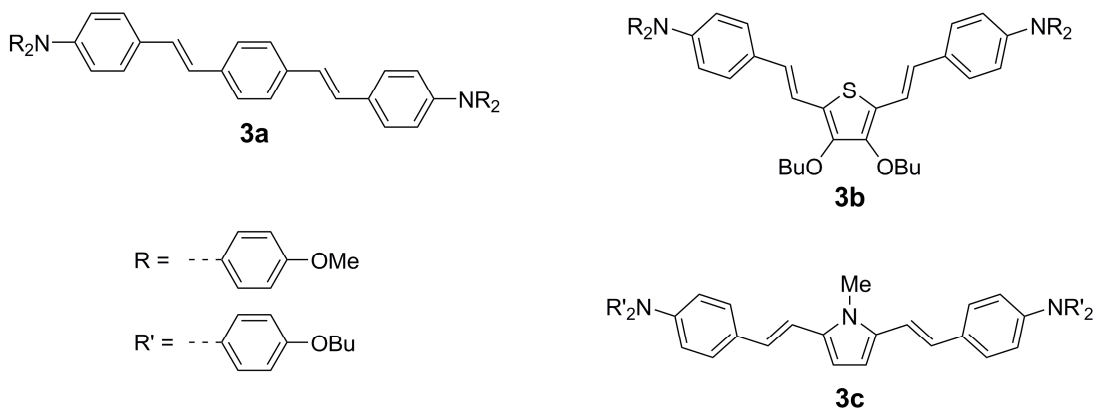

Figure 6.18 Examples of two-center triarylamines with different bridge energies

The monocations of **3a**–**3c** show an intense absorption in the near-IR region that can be attributed to optical electron transfer. A Hush analysis of the intervalence bands, shown in Table 6.2, indicates that the electronic coupling increases with bridge energy when the diabatic electron transfer distance, *R*, is equated to the N–N separation. Indeed, $\mathbf{3a}^+$ belongs to class-II,[24] whereas the intervalence bands for $\mathbf{3b}^+$–$\mathbf{3c}^+$ are characteristic of class-III compounds. The alternative optical estimate of *V* available for the latter suggests that *R* is much less than the N–N separation. More evidence for the stronger coupling in the heterocycle compounds is provided by ESR spectra of the dications: $\mathbf{3b}^{2+}$ is a singlet,[25] whereas $\mathbf{3a}^{2+}$ is paramagnetic.[24] Work is underway in the

same group to determine the effect of *relative* electron-richness of the terminal aryl rings and of the aromatic bridge.

Table 6.2 Hush analysis of the intervalence bands for **3a**$^+$–**3c**$^+$

Compound	ν_{max} (cm^{-1})	V_{II} (cm^{-1})[a]	V_{III} (cm^{-1})[b]	Class
3a$^+$[c]	6130	700	–	II
3b$^+$	5660	960	2830	III
3c$^+$	7630	920	3820	III

Obtained from: [a] Eq. 1.3 taking *R* as the N–N separation; [b] Eq. 1.8; [c] Ref. 24.

6.3.2 Two-Center Class-II Triarylamines

The effect of bridge energy was also central to Chapter 4. The thermal electron transfer in most class-II triarylamines is too fast to observe on the ESR timescale. By lowering the energy of the bridge, however, we observed a localized-to-delocalized ESR transition with temperature; this allowed the first comparison of thermal and optical electron transfer in mixed-valence triarylamines.[26] *This is no longer the only such study.* As shown in Figure 6.19, the radical cation of **4b**, in which the central benzene unit of **4a** is replaced by a paracyclophane unit, also shows temperature-dependent ESR spectra[27] along with a weak intervalence band amenable to Hush analysis.[28]

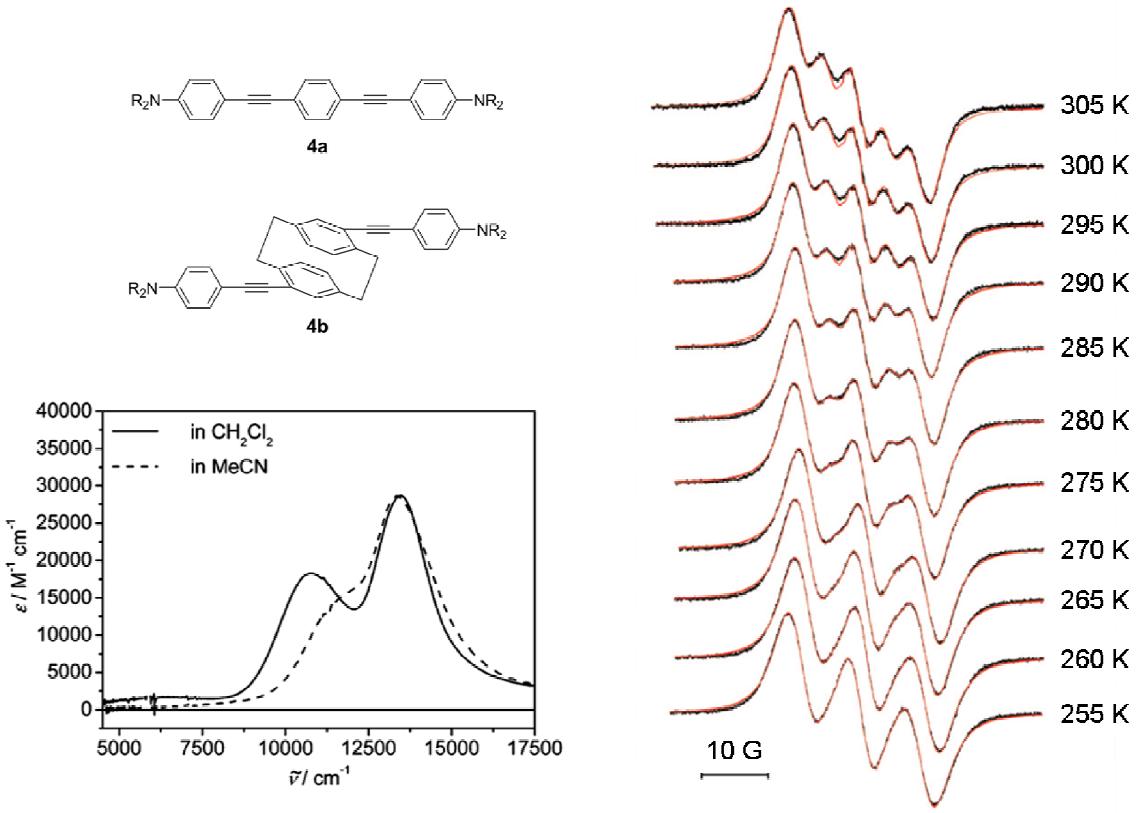

Figure 6.19 Structures of **4a** and **4b**, visible-NIR spectra of **4b**$^+$ in the indicated solvent,[28] and variable-temperature ESR spectra of **4b**$^+$ in *ortho*-dichlorobenzene (black) along with simulation (red)[27]

The thermal electron transfer rates in **4b**$^+$ were determined by simulation of the ESR spectra. An Arrhenius plot gives a linear relationship between ln(k_{ET}) and 1/T, from which the prefactor, A, and activation barrier, ΔG^*, can be estimated. The parameters are given in Table 6.3. By the same rational as in Chapter 4, the electron transfer in **4b**$^+$ was assumed to take place in the adiabatic regime.[27] It is interesting to note that the prefactors for **4a**$^+$ and **4b**$^+$ are quite similar – small prefactors thus appear to be the norm for such compounds. This gives further support to our claim that the nuclear frequency along the reaction coordinate in **4a**$^+$ is dominated by solvent reorientation, rather than intramolecular vibrations.

Table 6.3 Comparison of optical and thermal ET parameters for **4a**$^+$ and **4b**$^+$

Compound	λ (cm^{-1})	V_{NN} (cm^{-1})[a]	ΔG^*_{NN} (cm^{-1})[b]	ΔG^*_{ESR} (cm^{-1})[c]	A (s^{-1})[c]
4a$^+$	7780	490	1490	940	3.1×10^{10}
4b^{+}[d]	6600	230	1430	1190	3.6×10^{10}

Obtained from: [a] Eq. 1.3 taking R as the N–N separation; [b] Eq. 2.2; [c] fits of the ESR rate data to Eq. 2.1; [d] Refs. 27 and 28.

As shown in Table 6.3, the activation barriers extracted from optical data, ΔG^*_{NN}, exceed those determined from the ESR spectra, ΔG^*_{ESR}, when the diabatic electron transfer distance is equated to the N–N separation. This comparison shows once again that the redox centers cannot be regarded as purely localized on the triarylamines, but are displaced somewhat into the bridge. We anticipate many more compounds for which optical and thermal electron transfer can be observed and correlated. Such studies will undoubtedly afford a deeper insight into the intramolecular electron transfer processes in mixed-valence triarylamines.

6.3.3 Three-Center Class-II Triarylamines

Mixed-valence compounds that contain only two redox centers are among the simplest model systems for the study of electron transfer phenomena. Then again, those with three redox centers are more realistic models, for they allow electron transfer to occur in two dimensions. Chapter 5 was devoted to the study of such compounds. One need not be limited to the *meta*-topology of the compounds in that chapter, however. Once made, compounds like **5b** in Figure 6.20 should allow one to study the effect of saturated vs. unsaturated bridges on the electron transfer in three-center triarylamines.

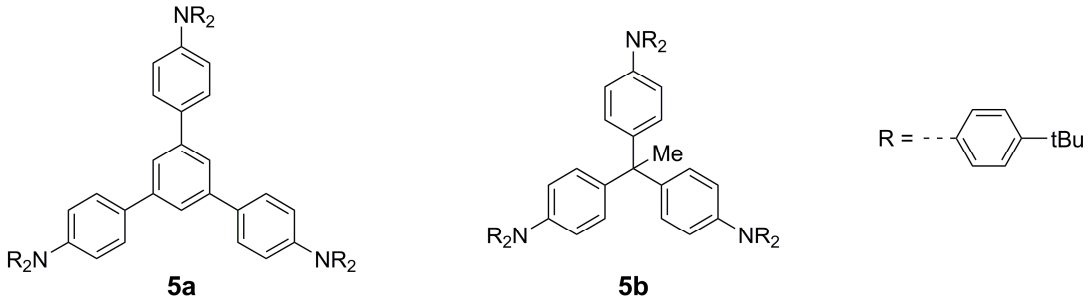

Figure 6.20 Examples of three-center class-II triarylamines

One way to estimate the electronic coupling in a mixed-valence compound is from the energy splitting of occupied orbitals in its neutral state.[29] In contrast to the case for two-center compounds, the electronic structure of a three-center compound depends on the sign of V. If the electronic coupling between redox centers is negative, the HOMO is degenerate; if V is positive, the HOMO–1 is degenerate.[30] The electronic coupling estimated in this way for **5a** and **5b** is given in Table 6.4; **5b** has the larger magnitude, consistent with its smaller N–N distance. What is more interesting, however, is that the values are of opposite sign. Compounds **5a** and **5b** could thus allow the first opportunity to determine the effect of the sign of V on the intramolecular electron transfer in three-center class-II triarylamines. For a given value of V, the thermal activation barrier is expected to be larger when $V > 0$ than when $V < 0$.[30]

Table 6.4 Electronic coupling estimated from orbital splitting[a]

Compound	V (cm^{-1})	Compound	V (cm^{-1})
5a	–110	**5b**	270

[a] Computed with DFT at the B3LYP/6-31G(d,p) level

6.3.4 Multi-Center Class-II+III Triarylamines

Earlier in this chapter, we considered four-center triarylamines in which both localized (class-II) and delocalized (class-III) transitions can occur. The notion of stabilizing high-spin compounds with *p*-phenylenediamine units can be further extended to give *multi*-center class-II+III triarylamines. The first compound with such a motif – **6a** in Figure 6.21 – was made by Wienk and Janssen.[12]

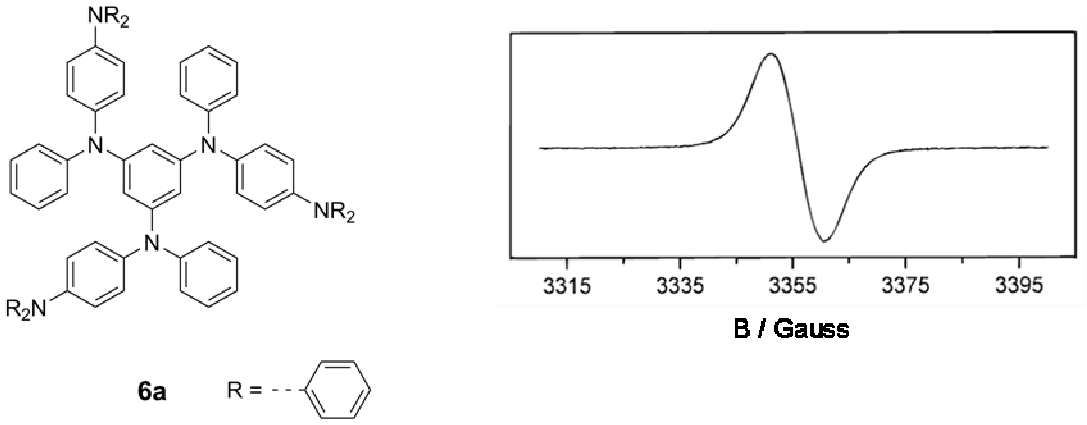

Figure 6.21 Structure of **6a** and room-temperature ESR spectrum of **6a**$^+$ obtained upon chemical oxidation in dichloromethane[12]

As shown in Figure 6.21, oxidation of **6a** leads to one broad ESR transition at room temperature, even when much less than one equivalent of oxidant is used.[12] The lack of fine structure can be attributed to disproportionation. As a corollary, though the optical spectrum shows a weak intervalence band due to intramolecular electron transfer between neutral and oxidized *p*-phenylenediamine units, the intensity of the band decreases well before an average of one electron is removed.[12] It appears quite difficult to isolate the mixed-valence state.

Ito et al. added yet another amine to each arm of **6a** to give the nine-center compounds in Figure 6.22.[31–33] In addition to a study of intramolecular electron transfer in multi-center triarylamines, compounds **6c–6e** could allow a study of end group effects. We focus here on **6d** and its three-center counterpart, **6b**.

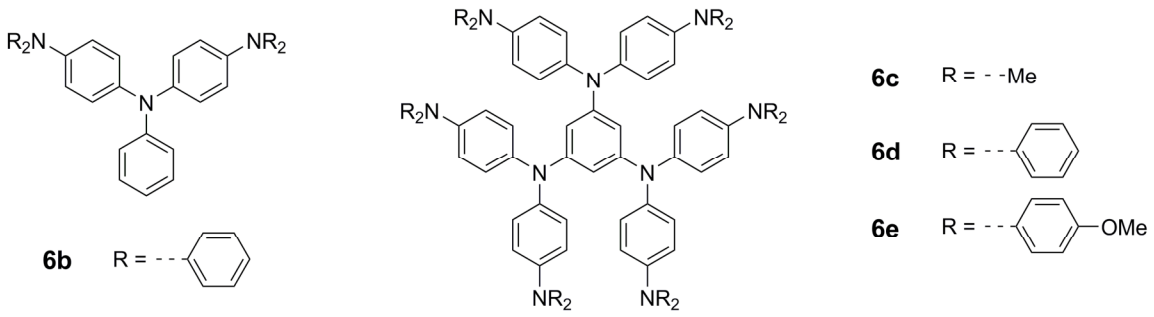

Figure 6.22 Structure of compounds **6b–6e**

The room-temperature ESR spectrum of $\mathbf{6b}^+$ in Figure 6.23 shows a broad nine-line pattern due to hyperfine interaction with three ^{14}N nuclei.[33] This line shape persists over a wide temperature range, indicating that the unpaired electron in $\mathbf{6b}^+$ is fully delocalized on the ESR time scale. In contrast, the variable-temperature ESR spectra of $\mathbf{6d}^+$ in Figure 6.23 show no hyperfine structure.[33] The peak-to-peak line width is temperature dependent, however, and the spectra can be simulated assuming dynamic exchange among the triamine units. The absorption spectrum of $\mathbf{6d}^+$ was also recorded, but any intervalence bands due to electron transfer *among* the arms were obscured by the intense intervalence transition *within* the arms.[33] Nevertheless, this study lends further credence to the central posit of this chapter that two types of intervalence states can coexist within a single molecule.

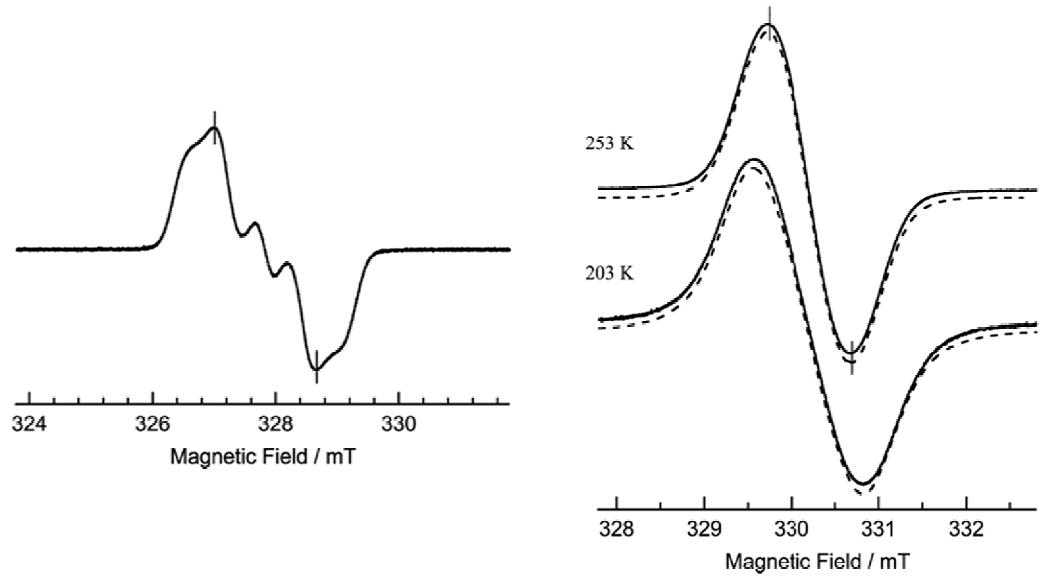

Figure 6.23 Room-temperature ESR spectrum of **6b**$^+$ (left) and variable-temperature ESR spectra for **6d**$^+$ (right) obtained upon chemical oxidation in dichloromethane[33]

6.4 Conclusions

The mixed-valence triarylamines in this thesis span the range from strongly- to weakly-coupled, and from two- to multi-center. Yet they all share one effect in common: that of bridge energy. By *raising* the energy of the bridge in Chapters 3 and 5, we increased both the electronic coupling between redox centers and the spin density on the bridge. By *lowering* the energy of the bridge in Chapter 4, we decreased the electronic coupling and thereby reduced the thermal electron transfer rate. We employ Hückel theory below to illustrate the effect of bridge energy. In using such an approach, we assume that the highest-occupied molecular orbital of the bridge mediates the coupling between redox centers, and we neglect any effects of geometry.

To begin, we represent the HOMO of each amine center as a *p*-orbital, as shown in Figure 6.24. There are two possible combinations of the amine orbitals: in-phase or out-of-phase, which, in the absence of direct orbital overlap, are of equal energy. One

can approximate the HOMO of the bridge in a similar manner. The out-of-phase combination of amine orbitals cannot interact with the bridge orbital, and it remains nonbonding in the composite system. In contrast, the in-phase combination can interact with the bridge to give rise to a bonding (lower-energy) and anti-bonding (higher-energy) molecular orbital. The energy difference between the two highest-occupied orbitals is, to a first approximation, a measure of the electronic coupling in the mixed-valence compound. As shown in Figure 6.24, the HOMO, which corresponds to the singly-occupied orbital in the radical cation, is dominated by amine orbitals in the case of large energy separation between the redox centers and the bridge.

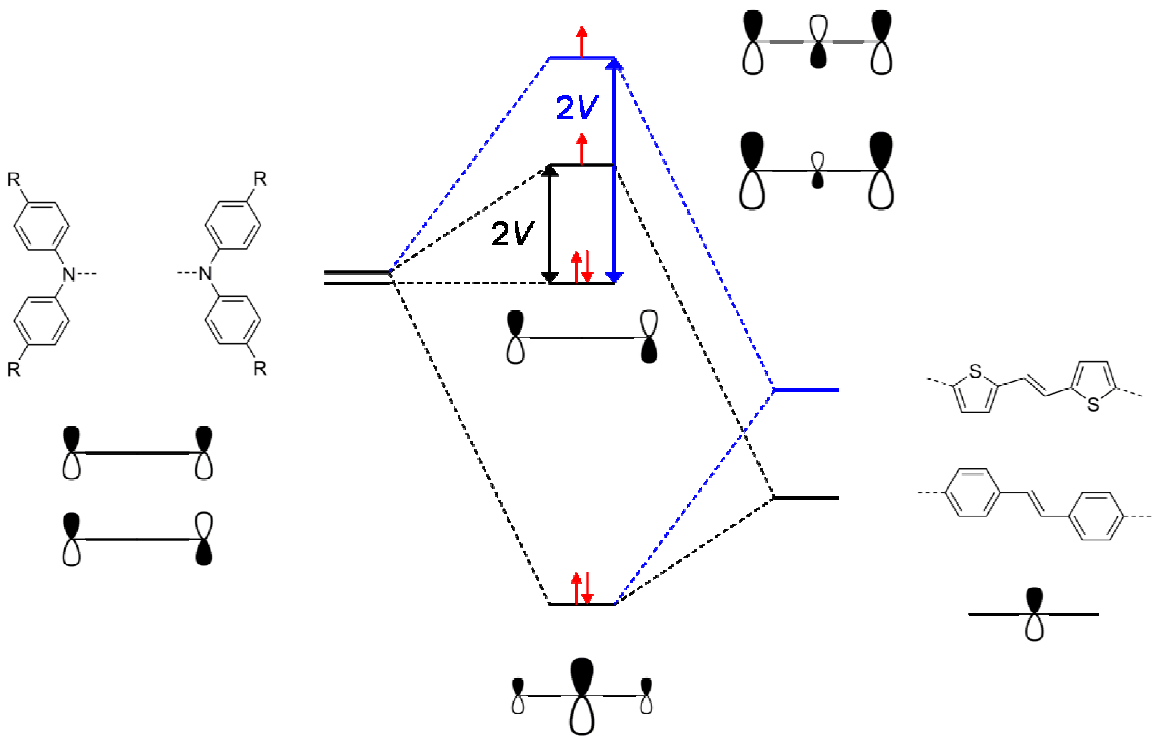

Figure 6.24 A simple Hückel theory diagram of the effect of bridge energy on the electronic coupling and spin density in a two-center mixed-valence compound

If we increase the energy of the bridge, for example by replacing benzene with thiophene, the resonance of the bridge and amine orbitals will increase, and thus the

splitting will increase. Not only that, but the singly-occupied orbital will have less amine character and more bridge character. This is exactly what we saw in Chapters 3 and 5. In Chapter 4, it was by lowering the energy of the bridge that we were able to reduce the electronic coupling such that we could observe thermal electron transfer on the ESR timescale. In principle, one can produce the same effect by raising the energy of the amine centers, for example by adding more electron-donating R groups. Thus, one can use the simple picture in Figure 6.24 to *tune* the properties of mixed-valence compounds, and to reconcile the central results of this thesis.

The field of mixed-valence chemistry has seen much progress since the first reports in the 1960s. In the case of two-center triarylamines, we now understand the effect of bridge energy on electron delocalization and, as shown here and in the publications below, on thermal electron transfer rates. But the study of intramolecular electron transfer phenomena is far from complete. In particular, much is left to learn about mixed-valence compounds with more than two redox centers. A further step is to extend what is now known about intramolecular electron transfer and delocalization to the *inter*molecular reactions that govern charge mobility in organic semiconductors. We fully expect that this field will continue to thrive.

- Odom, S. A.; Lancaster, K.; Beverina, L.; Lefler, K. M.; Thompson, N. J.; Coropceanu, V.; Brédas, J.-L.; Marder, S. R.; Barlow, S. *Chem. Eur. J.* **2007**, *13*, 9637

- Lancaster, K.; Odom, S. A.; Jones, S. C.; Thayumanavan, S.; Marder, S. R.; Brédas, J.-L.; Coropceanu, V.; Barlow, S. *J. Am. Chem. Soc.* **2009**, *131*, 1717

REFERENCES

[1] Yoshizawa, K.; Chano, A.; Ito, A.; Tanaka, K.; Yamabe, T.; Fujita, H.; Yamauchi, J.; Shiro, M. *J. Am. Chem. Soc.* **1992**, *114*, 5994.

[2] Stickley, K. R.; Blackstock, S. C. *J. Am. Chem. Soc.* **1994**, *116*, 11576.

[3] Longuet-Higgins, H. C. *J. Chem. Phys.* **1950**, *18*, 265.

[4] Ovchinnikov, A. A. *Theor. Chim. Acta* **1978**, *47*, 297.

[5] Borden, W. T.; Davidson, E. R. *J. Am. Chem. Soc.* **1977**, *99*, 4587.

[6] Hush, N. S. *Prog. Inorg. Chem.* **1967**, *8*, 391.

[7] Robin, M. B.; Day, P. *Adv. Inorg. Chem. Radiochem.* **1967**, *10*, 247.

[8] Lambert, C.; Nöll, G. *J. Am. Chem. Soc.* **1999**, *121*, 8434.

[9] Bushby, R. J.; McGill, D. R.; Ng, K. M.; Taylor, N. *J. Chem. Soc., Perkin Trans. 2* **1997**, 1405.

[10] Coropceanu, V.; Malagoli, M.; André, J. M.; Brédas, J.-L. *J. Am. Chem. Soc.* **2002**, *124*, 10519.

[11] Wienk, M. M.; Janssen, R. A. J. *Chem. Commun.* **1996**, 267.

[12] Wienk, M. M.; Janssen, R. A. J. *J. Am. Chem. Soc.* **1997**, *119*, 4492.

[13] Bewick, A.; Serve, D.; Joslin, T. A. *J. Electroanal. Chem.* **1983**, *154*, 81.

[14] Szeghalmi, A. V.; Erdmann, M.; Engel, V.; Schmitt, M.; Amthor, S.; Kriegisch, V.; Nöll, G.; Stahl, R.; Lambert, C.; Leusser, D.; Stalke, D.; Zabel, M.; Popp, J. *J. Am. Chem. Soc.* **2004**, *126*, 7834.

[15] Selby, T. D.; Blackstock, S. C. *J. Am. Chem. Soc.* **1999**, *121*, 7152.

[16] Ito, A.; Taniguchi, A.; Yamabe, T.; Tanaka, K. *Org. Lett.* **1999**, *1*, 741.

[17] Risko, C.; Coropceanu, V.; Barlow, S.; Geskin, V.; Schmidt, K.; Gruhn, N. E.; Marder, S. R.; Brédas, J.-L. *J. Phys. Chem. C* **2008**, *112*, 7959.

[18] Ito, A.; Ono, Y.; Tanaka, K. *Angew. Chem. Int. Ed.* **2000**, *39*, 1072.

[19] Selby, T. D.; Blackstock, S. C. *Org. Lett.* **1999**, *1*, 2053.

[20] Hauck, S. I.; Lakshmi, K. V.; Hartwig, J. F. *Org. Lett.* **1999**, *1*, 2057.

[21] Yan, X. Z.; Pawlas, J.; Goodson III, T.; Hartwig, J. F. *J. Am. Chem. Soc.* **2005**, *127*, 9105.

[22] Nelsen, S. F.; Li, G.; Schultz, K. P.; Tran, H. Q.; Guzei, I. A.; Evans, D. H. *J. Am. Chem. Soc.* **2008**, *130*, 11620.

[23] Odom, S. A.; Lancaster, K.; Beverina, L.; Lefler, K. M.; Thompson, N. J.; Coropceanu, V.; Brédas, J.-L.; Marder, S. R.; Barlow, S. *Chem. Eur. J.* **2007**, *13*, 9637.

[24] Barlow, S.; Risko, C.; Chung, S.-J.; Tucker, N. M.; Coropceanu, V.; Jones, S. C.; Levi, Z.; Brédas, J.-L.; Marder, S. R. *J. Am. Chem. Soc.* **2005**, *127*, 16900.

[25] Zheng, S.; Barlow, S.; Risko, C.; Kinnibrugh, T. L.; Khrustalev, V. N.; Jones, S. C.; Antipin, M. Y.; Tucker, N. M.; Timofeeva, T. V.; Coropceanu, V.; Brédas, J.-L.; Marder, S. R. *J. Am. Chem. Soc.* **2006**, *128*, 1812.

[26] Lancaster, K.; Odom, S. A.; Jones, S. C.; Thayumanavan, S.; Marder, S. R.; Brédas, J.-L.; Coropceanu, V.; Barlow, S. *J. Am. Chem. Soc.* **2009**, *131*, 1717.

[27] Kattnig, D. R.; Mladenova, B.; Grampp, G.; Kaiser, C.; Heckmann, A.; Lambert, C. *J. Phys. Chem. C* **2009**, *113*, 2983.

[28] Amthor, S.; Lambert, C. *J. Phys. Chem. A* **2006**, *110*, 1177.

[29] Coropceanu, V.; Malagoli, M.; André, J. M.; Brédas, J.-L. *J. Chem. Phys.* **2001**, *115*, 10409.

[30] Launay, J. P.; Babonneau, F. *Chem. Phys.* **1982**, *67*, 295.

[31] Ito, A.; Ino, H.; Matsui, Y.; Hirao, Y.; Tanaka, K.; Kanemoto, K.; Kato, T. *J. Phys. Chem. A* **2004**, *108*, 5715.

[32] Hirao, Y.; Ino, H.; Ito, A.; Tanaka, K.; Kato, T. *J. Phys. Chem. A* **2006**, *110*, 4866.

[33] Hirao, Y.; Ito, A.; Tanaka, K. *J. Phys. Chem. A* **2007**, *111*, 2951.

APPENDIX A

VIBRONIC COUPLING MODELS FOR TWO- AND THREE-CENTER MIXED-VALENCE COMPOUNDS

A.1 Two-Center, One-Mode Semiclassical Model

In what follows, we derive the electronic Hamiltonian that gives rise to the oft-seen potential energy curves for two-center mixed-valence compounds.[1] To begin we suppose that one center, which we designate A, is charged and the other center, B, is neutral. We assign the electronic Hamiltonian operators associated with the two centers as H_{el}^{A} and H_{el}^{B}, and if the corresponding wave functions are ψ^{A^+} and ψ^{B}:

$$H_{el}^{A}\psi^{A^+} = W^{A^+}\psi^{A^+} \qquad H_{el}^{B}\psi^{B} = W^{B}\psi^{B}$$

In the reverse case, where center A is neutral and center B is charged, the corresponding wave functions are ψ^{A} and ψ^{B^+}:

$$H_{el}^{A}\psi^{A} = W^{A}\psi^{A} \qquad H_{el}^{B}\psi^{B^+} = W^{B^+}\psi^{B^+}$$

If all nuclei are held fixed so that the nuclear kinetic energy is zero, and if no interaction is allowed between the two centers, we can write the electronic Schrödinger equation for each composite system:

$$\left(H_{el}^{A} + H_{el}^{B}\right)\psi^{A^+}\psi^{B} \equiv \left(H_{el}^{A} + H_{el}^{B}\right)\psi_a = \left(W^{A^+} + W^{B}\right)\psi_a \equiv W_a\psi_a$$

$$\left(H_{el}^{A} + H_{el}^{B}\right)\psi^{A}\psi^{B^+} \equiv \left(H_{el}^{A} + H_{el}^{B}\right)\psi_b = \left(W^{A} + W^{B^+}\right)\psi_b \equiv W_b\psi_b$$

We note that in our case, the two centers are equivalent by symmetry, and so the electronic wave functions ψ_a and ψ_b are degenerate, or $W_a = W_b$.

We now allow nuclear motion and seek vibrational wave functions corresponding to the states ψ_a and ψ_b. We expand the potential energy in a power series in the normal coordinates and keep terms only through quadratic. We note that since each center retains its point group symmetry in both oxidation states, it is only necessary to consider totally symmetric normal coordinates. This is not to be confused with the symmetry of the *composite* system, which can indeed show *broken* symmetry upon oxidation. We then assume that there is only one such coordinate associated with each center, which we designate Q_A and Q_B. The vibrational potential energies of centers A and B in their neutral and charged states are:

$$W^A = W^A(Q_A = 0) + l^A Q_A + \frac{k^A}{2} Q_A^2 \qquad W^{A^+} = W^{A^+}(Q_A = 0) + l^{A^+} Q_A + \frac{k^{A^+}}{2} Q_A^2$$

$$W^B = W^B(Q_B = 0) + l^B Q_B + \frac{k^B}{2} Q_B^2 \qquad W^{B^+} = W^{B^+}(Q_B = 0) + l^{B^+} Q_B + \frac{k^{B^+}}{2} Q_B^2$$

We now define the zero of energy by $W^{A^+}(Q_A = 0) + W^B(Q_B = 0) = 0$, which, since $W_a = W_b$, is the same as setting $W^A(Q_A = 0) + W^{B^+}(Q_B = 0) = 0$. We then choose origins by setting Q_A and Q_B to zero at the minima of W^A and W^B, respectively, so that $l^A = l^B = 0$. To end, we see that since centers A and B are equivalent, $l^{A^+} = l^{B^+} = l$, $k^{A^+} = k^{B^+} = k^+$ and $k^A = k^B = k$. The potential energies for the composite system, before any interaction between the centers is allowed, are:

$$W_a = lQ_A + \frac{k^+}{2}Q_A^2 + \frac{k}{2}Q_B^2$$

$$W_b = lQ_B + \frac{k}{2}Q_A^2 + \frac{k^+}{2}Q_B^2$$

Next, we introduce the new coordinates $Q_\pm = \frac{1}{\sqrt{2}}(Q_A \pm Q_B)$ such that $Q_A = \frac{1}{\sqrt{2}}(Q_+ + Q_-)$ and $Q_B = \frac{1}{\sqrt{2}}(Q_+ - Q_-)$. We also assume that $k^+ = k$, or that the force constant is the same in both oxidation states, which gives:

$$W_a = \frac{l}{\sqrt{2}}Q_- + \frac{k}{2}Q_-^2 + \frac{l}{\sqrt{2}}Q_+ + \frac{k}{2}Q_+^2$$

$$W_b = -\frac{l}{\sqrt{2}}Q_- + \frac{k}{2}Q_-^2 + \frac{l}{\sqrt{2}}Q_+ + \frac{k}{2}Q_+^2$$

Because we assume that $k^+ = k$, the problem is separable with respect to Q_+ and Q_-. Not only this, but because W_a and W_b give identical parabolas in Q_+ space, the coordinate Q_+ is superfluous. The latter is a result from linear algebra, which tells us that any constant added along the diagonal of a matrix simply adds to its eigenvalues and has no effect on the corresponding eigenfunctions. The crucial coordinate here is thus Q_-.

We next define the dimensionless variable $q = \frac{k}{l}Q_-$ such that $Q_- = \frac{l}{k}q$. We further define the parameter λ, or the reorganization energy, as $\lambda = \frac{l^2}{k}$ and so the potential surfaces in q space are:

$$W_a = \lambda\left[\frac{1}{\sqrt{2}}q + \left(\frac{1}{\sqrt{2}}q\right)^2\right]$$

$$W_b = \lambda\left[-\frac{1}{\sqrt{2}}q + \left(\frac{1}{\sqrt{2}}q\right)^2\right]$$

We finally let centers A and B interact. We denote such coupling by V^{AB} and amend this to the electronic Hamiltonian:

$$H_{el} = H_{el}^{A} + H_{el}^{B} + V^{AB}$$

If we assume that centers A and B are such that the overlap between orbitals on the two different centers is zero, or:

$$\left\langle \psi_i \middle| \psi_j \right\rangle = \delta_{ij} \qquad i, j = a, b$$

and let $H_{ij} = \left\langle \psi_i \middle| H_{el}\psi_j \right\rangle$ and $V_{ij} = \left\langle \psi_i \middle| V^{AB}\psi_j \right\rangle$, then:

$$H_{aa} = W_a + V_{aa} \qquad H_{ab} = V_{ab}$$

$$H_{ba} = H_{ab} = V_{ab} \qquad H_{bb} = W_b + V_{bb} = W_b + V_{aa}$$

when the nuclei are held fixed at $q = 0$. The last two equalities are due to the equivalency of centers A and B. Because the quantity V_{aa} appears only along the diagonal, we can define a new zero of energy by $V_{aa} = 0$. The Schrödinger equations thus become:

$$H_{el}\psi_k = W_k\psi_k \qquad \psi_k = c_{ak}\psi_a + c_{bk}\psi_b \qquad k = 1,2$$

$$H_{el} = \begin{bmatrix} W_a & V_{ab} \\ V_{ab} & W_b \end{bmatrix}$$

Our task is to solve the corresponding secular determinant. The roots of the determinant are simply the eigenvalues of the electronic Hamiltonian operator. We refer to the roots W_k as potential surfaces because they describe the potential energy of the system as a function of nuclear coordinates. The surfaces, as a function of V_{ab}, are equivalent to those shown in Figure 1.2. We seek the vibronic manifold associated with the potential surfaces in order to calculate the absorption band contour that results when transitions occur between the surfaces. This contour is the so-called intervalence band.

To begin we write our *vibronic* wave functions as linear combinations of the *electronic* wave functions ψ_1 and ψ_2:

$$\Psi_k = \psi_1 \chi_{1,k} + \psi_2 \chi_{2,k} \qquad k = 1,2,\cdots,\infty$$

If we allow nuclear motion, we must now use the full Hamiltonian; that is, we must include the nuclear kinetic energy operator:

$$H = H_{el} + T_n$$

Our task is to solve the *vibronic* Schrödinger equation:

$$H\Psi_k = E_k \Psi_k$$

where E_k are the vibronic eigenvalues. To do so, we multiply the vibronic Schrödinger equation by ψ_1 and ψ_2 in turn and integrate over electronic coordinates. We recall that $H_{el}\psi_i = W_i\psi_i$ and $\langle \psi_i | \psi_j \rangle = \delta_{ij}$ to obtain:

$$W_1\chi_{1,k} + \langle \psi_1 | T_n \psi_1 \rangle \chi_{1,k} + \langle \psi_1 | T_n \psi_2 \rangle \chi_{2,k} = E_k \chi_{1,k}$$

$$W_2\chi_{2,k} + \langle\psi_2 | T_n\psi_2\rangle\chi_{2,k} + \langle\psi_2 | T_n\psi_1\rangle\chi_{1,k} = E_k\chi_{2,k}$$

If we assume that the nuclear kinetic energy operator commutes with the electronic wave functions ψ_i so that $T_n\psi_i\chi_{i,k} = \psi_i T_n\chi_{i,k}$, and note once more the orthonormality of the ψ_i's:

$$[W_1 + T_n]\chi_{1,k} = E_k\chi_{1,k}$$

$$[W_2 + T_n]\chi_{2,k} = E_k\chi_{2,k}$$

We see that the vibrational function $\chi_{i,k}$ is determined only by the W_i potential surface. The nuclear motion is confined to that surface alone, and so we can write:

$$\Psi_k^{(i)} = \psi_i\chi_{i,k} \qquad i = 1,2 \qquad k = 1,2,\cdots,\infty$$

In other words, the Born-Oppenheimer approximation is operative. We caution here that such an approximation is quite crude, and is actually only valid if either λ or $V_{ab} = 0$. For all other cases, the approximation breaks down, and the nuclear motion cannot be confined to a single potential surface. Be that as it may, such an approach is often used to simulate the intervalence bands. We thus continue on with these Born-Oppenheimer products to calculate the band contour.

To start, we sweep a vertical arrow connecting the potential surfaces in q space. At each value of q, we make a contribution to the band at an energy equal to the length of the arrow and with an intensity proportional to the product of the Boltzmann factor and the square of the transition moment. We add together all contributions at the same transition energy and normalize the result. The totality of such lines comprises the intervalence band contour:

$$F(E) = \frac{\sum_q e^{-W_1/k_B T} \left| \left\langle \psi_1 \left| \hat{d} \psi_2 \right\rangle \right|^2 \delta[E - (W_2 - W_1)]}{\sum_q e^{-W_1/k_B T}}$$

Here, $E = h\nu$ is the photon energy, $\left\langle \psi_1 \left| \hat{d} \psi_2 \right\rangle \right.$ is the transition dipole moment, δ is the Dirac delta function, W_1 and W_2 are the roots of the secular determinant, and the sum in the denominator is the normalizing factor.

In writing such an expression we treat the vibrational motion semiclassically. That is, for a given vibronic transition we assume that the entire contribution to the vibrational overlap integral $\left\langle \chi_{2,k'} \left| \chi_{1,k} \right\rangle \right.$ is at the classical turning points. The nuclear motion pauses at these points and so E_k is equal to W_k. We also assume a continuum of vibrational energy levels on each potential surface; that is, the spacing between successive levels is infinitesimal. Both of our assumptions are favored by high temperature because an increasing number of vibrational levels are populated and the harmonic oscillator functions approach classical behavior for large quantum number.

The transition dipole moment $\left\langle \psi_1 \left| \hat{d} \psi_2 \right\rangle \right.$ depends on the amount of mixing between the localized states. That is, it depends on the eigenvectors of the electronic Hamiltonian. Recall that these are of the form:

$$\psi_1 = c_{a1}\psi_a + c_{b1}\psi_b \qquad \psi_2 = c_{a2}\psi_a + c_{b2}\psi_b$$

The transition dipole moment is thus:

$$\left\langle \psi_1 \left| \hat{d} \psi_2 \right\rangle \right. = c_{a1}c_{a2} \left\langle \psi_a \left| \hat{d} \psi_a \right\rangle \right. + c_{b1}c_{b2} \left\langle \psi_b \left| \hat{d} \psi_b \right\rangle \right.$$

If we take the origin as the midpoint of the line connecting the two centers, and let R equal the distance between the centers, the moments are:

$$\left\langle \psi_a \left| \hat{d} \psi_a \right\rangle = \frac{-1}{2\sqrt{2}} eR \qquad \left\langle \psi_b \left| \hat{d} \psi_b \right\rangle = \frac{1}{2\sqrt{2}} eR \right.$$

It follows that the transition dipole moment is:

$$\left\langle \psi_1 \left| \hat{d} \psi_2 \right\rangle = \frac{eR}{2\sqrt{2}} \left(c_{b1} c_{b2} - c_{a1} c_{a2} \right) \right.$$

To end, we rewrite the delta function as the following limit:

$$\delta\left[E - \left(W_2 - W_1\right)\right] = \lim_{c \to 0} \frac{1}{2\sqrt{\pi c}} e^{-\left[E - (W_2 - W_1)\right]^2 / 4c}$$

This is equivalent to assuming that each vibronic line takes a Gaussian shape. As c → 0, the band contour thus becomes:

$$F(E) = \frac{\sum_q e^{-W_1 / k_B T} \left| \left\langle \psi_1 \left| \hat{d} \psi_2 \right\rangle \right|^2 e^{-\left[E - (W_2 - W_1)\right]^2 / 4c}}{2\sqrt{\pi c} \sum_q e^{-W_1 / k_B T}}$$

A.2 Two-Center, One-Mode Vibronic Coupling Model

The semiclassical model of the previous section, though often used, is not a rigorous solution of the vibronic Schrödinger equation; the PKS model was the first such solution.[2,3] We outline below the model of Piepho, Krausz and Schatz. Recall that, before we made the Born-Oppenheimer approximation, we wrote the *vibronic* wave functions as linear combinations of the *electronic* wave functions ψ_1 and ψ_2:

$$\Psi_k(r,q) = \psi_1(r,q)\chi_{1,k}(q) + \psi_2(r,q)\chi_{2,k}(q) \qquad k = 1,2,\cdots,\infty$$

where r and q denote electronic and nuclear coordinates, respectively. In fact, it is the q-dependence of ψ_1 and ψ_2 that forces us to make such a drastic approximation. To eliminate the q-dependence, and thus the need to invoke the Born-Oppenheimer approximation, we define the new functions $\psi_\pm$ as:

$$\psi_\pm = \frac{1}{\sqrt{2}}(\psi_a \pm \psi_b)$$

The *electronic* wave functions ψ_+ and ψ_- are q-independent, and the *vibronic* wave functions are thus:

$$\Psi_k(r,q) = \psi_+(r)\chi_{+,k}(q) + \psi_-(r)\chi_{-,k}(q)$$

where χ_+ and χ_- are linear combinations of χ_1 and χ_2. Our task, once again, is to solve the vibronic Schrödinger equation:

$$H\Psi_k = E_k\Psi_k$$

where E_k are the vibronic eigenvalues. To do so, we multiply the vibronic Schrödinger equation by ψ_+ and ψ_- in turn and integrate over electronic coordinates r. We recall that $\langle \psi_i | \psi_j \rangle = \delta_{ij}$, where $i, j = a, b$, and thus $\langle \psi_\pm | \psi_\pm \rangle = \delta_\pm$, to obtain:

$$\langle \psi_+ | H_{el}\psi_+ \rangle \chi_{+,k} + \langle \psi_+ | T_n\psi_+ \rangle \chi_{+,k} + \langle \psi_+ | H_{el}\psi_- \rangle \chi_{-,k} + \langle \psi_+ | T_n\psi_- \rangle \chi_{-,k} = E_k\chi_{+,k}$$

$$\langle \psi_- | H_{el}\psi_+ \rangle \chi_{+,k} + \langle \psi_- | T_n\psi_+ \rangle \chi_{+,k} + \langle \psi_- | H_{el}\psi_- \rangle \chi_{-,k} + \langle \psi_- | T_n\psi_- \rangle \chi_{-,k} = E_k\chi_{-,k}$$

If we assume that T_n commutes with ψ_a and ψ_b, and therefore $\psi_\pm$, so that $T_n\psi_\pm\chi_{\pm,k} = \psi_\pm T_n\chi_{\pm,k}$, and note once more the orthonormality of $\psi_\pm$, we obtain:

$$\langle\psi_+|H_{el}\psi_+\rangle\chi_{+,k} + T_n\chi_{+,k} + \langle\psi_+|H_{el}\psi_-\rangle\chi_{-,k} = E_k\chi_{+,k}$$

$$\langle\psi_-|H_{el}\psi_+\rangle\chi_{+,k} + \langle\psi_-|H_{el}\psi_-\rangle\chi_{-,k} + T_n\chi_{-,k} = E_k\chi_{-,k}$$

The electronic wave functions $\psi_\pm$ are *not* eigenfunctions of H_{el}. Recall, however, that if we let $H_{ij} = \langle\psi_i|H_{el}\psi_j\rangle$ and $V_{ij} = \langle\psi_i|V^{AB}\psi_j\rangle$, where $i, j = a, b$, then:

$$H_{aa} = W_a \qquad H_{ab} = H_{ba} = V_{ab} \qquad H_{bb} = W_b$$

and so the vibronic Schrödinger equations become:

$$\left(\frac{W_a + W_b}{2} + V_{ab}\right)\chi_{+,k} + T_n\chi_{+,k} + \left(\frac{W_a - W_b}{2}\right)\chi_{-,k} = E_k\chi_{+,k}$$

$$\left(\frac{W_a - W_b}{2}\right)\chi_{+,k} + \left(\frac{W_a + W_b}{2} - V_{ab}\right)\chi_{-,k} + T_n\chi_{-,k} = E_k\chi_{-,k}$$

Next, we re-define the parameters q and λ as:

$$q = \sqrt{\frac{4\pi^2\nu_-}{h}}Q_- \qquad \lambda = \frac{1}{\sqrt{8\pi^2 h\nu_-^3}}l$$

where $\nu_- = \frac{\sqrt{k}}{2\pi}$ is the fundamental vibrational frequency associated with normal coordinate Q_- (or q). The potentials, in units of $h\nu_-$, are:

$$\frac{W_a}{h\nu_-} = \lambda q + \frac{q^2}{2}$$

$$\frac{W_b}{h\nu_-} = -\lambda q + \frac{q^2}{2}$$

Note that the quadratic term is no longer a function of λ, as it was in the previous section. The vibronic equations are now:

$$\left(T_n + \frac{q^2}{2} + V_{ab}\right)\chi_{+,k} + (\lambda q)\chi_{-,k} = E_k \chi_{+,k}$$

$$(\lambda q)\chi_{+,k} + \left(T_n + \frac{q^2}{2} - V_{ab}\right)\chi_{-,k} = E_k \chi_{-,k}$$

where V_{ab} and E_k are in units of $h\nu_-$. We see that the equations for χ_+ and χ_- are coupled. To circumvent this complication, we expand χ_+ and χ_- in the complete orthonormal set of harmonic oscillator functions χ_n:

$$\chi_{+,k} = \sum_n c^+_{k,n}\chi_n \qquad \chi_{-,k} = \sum_n c^-_{k,n}\chi_n \qquad n = 0,1,2,\cdots,\infty$$

The vibronic wave functions are thus:

$$\Psi_k = \psi_+ \sum_n c^+_{k,n}\chi_n + \psi_- \sum_n c^-_{k,n}\chi_n$$

We now exploit the properties of harmonic oscillators. To start, we note that $\chi_n(-q) = (-1)^n \chi_n(q)$. This permits us to separate the Ψ_k in accord with their behavior under interchange:

$$\Psi_k^+ = \psi_+ \sum_{n,even} C_{k,n}^+ \chi_n + \psi_- \sum_{n,odd} C_{k,n}^+ \chi_n$$

$$\Psi_k^- = \psi_+ \sum_{n,odd} C_{k,n}^- \chi_n + \psi_- \sum_{n,even} C_{k,n}^- \chi_n$$

Ψ_k^- and Ψ_k^+ do and do not change sign under interchange, respectively. Our task is to calculate the coefficients $C_{k,n}^+$ and $C_{k,n}^-$ for each value of *k*. We focus on $C_{k,n}^+$ first:

$$\left(T_n + \frac{q^2}{2} + V_{ab}\right) \sum_{n,even} C_{k,n}^+ \chi_n + \lambda q \sum_{n,odd} C_{k,n}^+ \chi_n = E_k^+ \sum_{n,even} C_{k,n}^+ \chi_n$$

$$\lambda q \sum_{n,even} C_{k,n}^+ \chi_n + \left(T_n + \frac{q^2}{2} - V_{ab}\right) \sum_{n,odd} C_{k,n}^+ \chi_n = E_k^+ \sum_{n,odd} C_{k,n}^+ \chi_n$$

To simplify the vibronic equations, we exploit two other properties of harmonic oscillators:

$$\left(T_n + \frac{q^2}{2}\right)\chi_n = \left(n + \frac{1}{2}\right)\chi_n$$

$$\langle \chi_{n-1} | q\chi_m \rangle = \sqrt{\frac{m+1}{2}}\delta_{m,n-1} \qquad \langle \chi_{n+1} | q\chi_m \rangle = \sqrt{\frac{m}{2}}\delta_{m,n+1}$$

Note that the eigenvalues $\left(n + \frac{1}{2}\right)$ are in units of $h\nu_-$. If we multiply the vibronic Schrödinger equations above by each χ_n in turn and integrate over nuclear coordinates *q*, the two equations reduce to one:

$$C_{k,n}^+ \left[\left(m + \frac{1}{2} + (-1)^m V_{ab} \right) \delta_{m,n} + \lambda \left(\sqrt{\frac{m}{2}}\delta_{m,n+1} + \sqrt{\frac{m+1}{2}}\delta_{m,n-1} \right) \right] = C_{k,n}^+ H_{m,n}^+ = C_{k,n}^+ E_k^+ \delta_{m,n}$$

where m, $n = 0 - \infty$. For m, $n = 0 - 3$, the vibronic Hamiltonian $H^{+}_{m,n}$ takes the form:

$$H^{+}_{m,n} = \begin{bmatrix} \frac{1}{2}+V_{ab} & \sqrt{\frac{1}{2}}\lambda & 0 & 0 \\ \sqrt{\frac{1}{2}}\lambda & \frac{3}{2}-V_{ab} & \lambda & 0 \\ 0 & \lambda & \frac{5}{2}+V_{ab} & \sqrt{\frac{3}{2}}\lambda \\ 0 & 0 & \sqrt{\frac{3}{2}}\lambda & \frac{7}{2}-V_{ab} \end{bmatrix}$$

The *complete* matrix is, of course, infinite. In practice, one truncates the number of quanta (n) to calculate the intervalence band contour. Returning to $C^{-}_{k,n}$ we obtain:

$$\left(T_n + \frac{q^2}{2} + V_{ab}\right)\sum_{n,odd} C^{-}_{k,n}\chi_n + \lambda q \sum_{n,even} C^{-}_{k,n}\chi_n = E^{-}_{k} \sum_{n,odd} C^{-}_{k,n}\chi_n$$

$$\lambda q \sum_{n,odd} C^{-}_{k,n}\chi_n + \left(T_n + \frac{q^2}{2} - V_{ab}\right)\sum_{n,even} C^{-}_{k,n}\chi_n = E^{-}_{k} \sum_{n,even} C^{-}_{k,n}\chi_n$$

We multiply the equations by each χ_n in turn and integrate over nuclear coordinates q to obtain:

$$C^{-}_{k,n}\left[\left(m + \frac{1}{2} + (-1)^{m+1}V_{ab}\right)\delta_{m,n} + \lambda\left(\sqrt{\frac{m}{2}}\delta_{m,n+1} + \sqrt{\frac{m+1}{2}}\delta_{m,n-1}\right)\right] = C^{-}_{k,n}H^{-}_{m,n} = C^{-}_{k,n}E^{-}_{k}\delta_{m,n}$$

where m, $n = 0 - \infty$. For m, $n = 0 - 3$, the vibronic Hamiltonian $H^{-}_{m,n}$ takes the form:

$$H^{-}_{m,n} = \begin{bmatrix} \frac{1}{2} - V_{ab} & \sqrt{\frac{1}{2}}\lambda & 0 & 0 \\ \sqrt{\frac{1}{2}}\lambda & \frac{3}{2} + V_{ab} & \lambda & 0 \\ 0 & \lambda & \frac{5}{2} - V_{ab} & \sqrt{\frac{3}{2}}\lambda \\ 0 & 0 & \sqrt{\frac{3}{2}}\lambda & \frac{7}{2} + V_{ab} \end{bmatrix}$$

To summarize, we can solve for both the vibronic eigenvalues $E_k^{\pm}$ and the coefficients $C_{k,n}^{\pm}$ of the vibronic eigenvectors:

$$\Psi_k^{+} = \psi_{+} \sum_{n,even} C_{k,n}^{+} \chi_n + \psi_{-} \sum_{n,odd} C_{k,n}^{+} \chi_n$$

$$\Psi_k^{-} = \psi_{+} \sum_{n,odd} C_{k,n}^{-} \chi_n + \psi_{-} \sum_{n,even} C_{k,n}^{-} \chi_n$$

We can, thereby, calculate the position (related to $E_k^{\pm}$) and intensity (related to $C_{k,n}^{\pm}$) of each transition contributing to the intervalence band contour. The intensity of one such vibronic line is given by:

$$I(k' \rightarrow k) = \frac{N_{k'} - N_k}{N} \left| \left\langle \Psi_{k'}^{+} \middle| \hat{d} \Psi_k^{-} \right\rangle \right|^2$$

where $\left\langle \Psi_{k'}^{+} \middle| \hat{d} \Psi_k^{-} \right\rangle$ is the transition dipole moment. Note that, due to symmetry, only $\pm \rightarrow \mp$ transitions are allowed. To evaluate this expression, we re-write the vibronic wave functions as:

$$\Psi_{k'}^{+} = \psi_{+} \chi_{+,k'}^{+} + \psi_{-} \chi_{-,k'}^{+}$$

$$\Psi_k^- = \psi_+ \chi_{+,k}^- + \psi_- \chi_{-,k}^-$$

and thus:

$$\left\langle \Psi_{k'}^+ \middle| \hat{d} \middle| \Psi_k^- \right\rangle = \left\langle \psi_+ \chi_{+,k'}^+ + \psi_- \chi_{-,k'}^+ \middle| \hat{d} \middle| \psi_+ \chi_{+,k}^- + \psi_- \chi_{-,k}^- \right\rangle$$

We now make the Franck-Condon approximation; that is, we assume $\left\langle \psi_\pm \chi_\pm^\pm \middle| \hat{d} \middle| \psi_\pm \chi_\pm^\pm \right\rangle$ = $\left\langle \psi_\pm \middle| \hat{d} \middle| \psi_\pm \right\rangle \left\langle \chi_\pm^\pm \middle| \chi_\pm^\pm \right\rangle$. Next, we note that $\left\langle \chi_{+,k'}^+ \middle| \chi_{+,k}^- \right\rangle = \left\langle \chi_{-,k'}^+ \middle| \chi_{-,k}^- \right\rangle = 0$ to obtain:

$$\left\langle \Psi_{k'}^+ \middle| \hat{d} \Psi_k^- \right\rangle = \left\langle \psi_+ \middle| \hat{d} \psi_- \right\rangle \left\langle \chi_{+,k'}^+ \middle| \chi_{-,k}^- \right\rangle + \left\langle \psi_- \middle| \hat{d} \psi_+ \right\rangle \left\langle \chi_{-,k'}^+ \middle| \chi_{+,k}^- \right\rangle$$

The total moment now depends on the *electronic* transition dipole moment and the vibrational overlap. Recall that $\psi_\pm = \frac{1}{\sqrt{2}} (\psi_a \pm \psi_b)$ and thus:

$$\left\langle \psi_+ \middle| \hat{d} \psi_- \right\rangle = \left\langle \psi_- \middle| \hat{d} \psi_+ \right\rangle = \frac{1}{2} \left\langle \psi_a \middle| \hat{d} \psi_a \right\rangle - \frac{1}{2} \left\langle \psi_b \middle| \hat{d} \psi_b \right\rangle$$

If we take the origin as the midpoint of the line connecting the two centers, and let *R* equal the distance between the centers, the moments are:

$$\left\langle \psi_a \middle| \hat{d} \psi_a \right\rangle = \frac{-eR}{2} \qquad \left\langle \psi_b \middle| \hat{d} \psi_b \right\rangle = \frac{eR}{2}$$

It follows that the total moment is:

$$\left\langle \Psi_{k'}^+ \middle| \hat{d} \Psi_k^- \right\rangle = \frac{-eR}{2} \left[\left\langle \chi_{+,k'}^+ \middle| \chi_{-,k}^- \right\rangle + \left\langle \chi_{-,k'}^+ \middle| \chi_{+,k}^- \right\rangle \right]$$

The quantity in brackets reduces to a vector multiplication of the coefficients $C_{k,n}^{\pm}$; that is, $\left\langle \chi_{+,k'}^{+} \middle| \chi_{-,k}^{-} \right\rangle + \left\langle \chi_{-,k'}^{+} \middle| \chi_{+,k}^{-} \right\rangle = \sum_n C_{k',n}^{+} C_{k,n}^{-}$. The intensity of one vibronic line is thus:

$$I(k' \to k) = \left(\frac{e^2 R^2}{4} \right) \left(\frac{N_{k'} - N_k}{N} \right) \left(\sum_n C_{k',n}^{+} C_{k,n}^{-} \right)^2$$

where the middle quantity relates to the fraction of molecules in each vibronic state:

$$\frac{N_{k'} - N_k}{N} = \frac{e^{-E_{k'}^{+}/k_B T} - e^{-E_k^{-}/k_B T}}{\sum_{k'} e^{-E_{k'}^{+}/k_B T}}$$

The totality of such lines comprises the intervalence band contour.

In this section, we saw that the PKS model, which uses a valence bond basis, considers only one electron transfer coordinate – the antisymmetric combination (q_-) of vibrations localized on the redox centers. Piepho later developed a model, using a molecular orbital basis, which also considers a symmetric mode (q_+) governing the distance between centers.[4] The Piepho model is discussed in Chapter 1.

A.3 Three-Center, Two-Mode Semiclassical Model

In what follows, we derive the electronic Hamiltonian that gives rise to the potential energy curves for three-center mixed-valence compounds. This was first done by Launay and Babonneau.[5] To begin we suppose that one center, which we designate A, is charged and the other two centers, B and C, are neutral. We assign the electronic

Hamiltonian operators associated with the three centers as H_{el}^{A}, H_{el}^{B} and H_{el}^{C}, and if the corresponding wave functions are ψ^{A^+}, ψ^{B} and ψ^{C}:

$$H_{el}^{A}\psi^{A^+} = W^{A^+}\psi^{A^+} \qquad H_{el}^{B}\psi^{B} = W^{B}\psi^{B} \qquad H_{el}^{C}\psi^{C} = W^{C}\psi^{C}$$

In the second case, where centers A and C are neutral and center B is charged, the corresponding wave functions are ψ^{A}, ψ^{B^+} and ψ^{C}:

$$H_{el}^{A}\psi^{A} = W^{A}\psi^{A} \qquad H_{el}^{B}\psi^{B^+} = W^{B^+}\psi^{B^+} \qquad H_{el}^{C}\psi^{C} = W^{C}\psi^{C}$$

In the third and final case, where centers A and B are neutral and center C is charged, the corresponding wave functions are ψ^{A}, ψ^{B} and ψ^{C^+}:

$$H_{el}^{A}\psi^{A} = W^{A}\psi^{A} \qquad H_{el}^{B}\psi^{B} = W^{B}\psi^{B} \qquad H_{el}^{C}\psi^{C^+} = W^{C^+}\psi^{C^+}$$

If all nuclei are held fixed so that the nuclear kinetic energy is zero, and if no interaction is allowed between the three centers, we can write the electronic Schrödinger equation for each composite system:

$$\left(H_{el}^{A} + H_{el}^{B} + H_{el}^{C}\right)\psi^{A^+}\psi^{B}\psi^{C} \equiv \left(H_{el}^{A} + H_{el}^{B} + H_{el}^{C}\right)\psi_a = \left(W^{A^+} + W^{B} + W^{C}\right)\psi_a \equiv W_a\psi_a$$

$$\left(H_{el}^{A} + H_{el}^{B} + H_{el}^{C}\right)\psi^{A}\psi^{B^+}\psi^{C} \equiv \left(H_{el}^{A} + H_{el}^{B} + H_{el}^{C}\right)\psi_b = \left(W^{A} + W^{B^+} + W^{C}\right)\psi_b \equiv W_b\psi_b$$

$$\left(H_{el}^{A} + H_{el}^{B} + H_{el}^{C}\right)\psi^{A}\psi^{B}\psi^{C^+} \equiv \left(H_{el}^{A} + H_{el}^{B} + H_{el}^{C}\right)\psi_c = \left(W^{A} + W^{B} + W^{C^+}\right)\psi_c \equiv W_c\psi_c$$

We note that in our case, the three centers are equivalent by symmetry, and so the electronic wave functions ψ_a, ψ_b and ψ_c are degenerate, or $W_a = W_b = W_c$.

We now allow nuclear motion and seek vibrational wave functions corresponding to the states ψ_a, ψ_b and ψ_c. We expand the potential energy in a power series in the normal coordinates and keep terms only through quadratic. We note that since each center retains its point group symmetry in both oxidation states, it is only necessary to consider totally symmetric normal coordinates. We then assume that there is only one such coordinate associated with each center, which we designate Q_A, Q_B and Q_C. The vibrational potential energies in both neutral and charged states are:

$$W^A = W^A(Q_A = 0) + l^A Q_A + \frac{k^A}{2} Q_A^2 \qquad W^{A^+} = W^{A^+}(Q_A = 0) + l^{A^+} Q_A + \frac{k^{A^+}}{2} Q_A^2$$

$$W^B = W^B(Q_B = 0) + l^B Q_B + \frac{k^B}{2} Q_B^2 \qquad W^{B^+} = W^{B^+}(Q_B = 0) + l^{B^+} Q_B + \frac{k^{B^+}}{2} Q_B^2$$

$$W^C = W^C(Q_C = 0) + l^C Q_C + \frac{k^C}{2} Q_C^2 \qquad W^{C^+} = W^{C^+}(Q_C = 0) + l^{C^+} Q_C + \frac{k^{C^+}}{2} Q_C^2$$

We now define the zero of energy by $W^{A^+}(Q_A = 0) + W^B(Q_B = 0) + W^C(Q_C = 0) = 0$, which is the same as setting $W^A(Q_A = 0) + W^{B^+}(Q_B = 0) + W^C(Q_C = 0) = 0$ or $W^A(Q_A = 0) + W^B(Q_B = 0) + W^{C^+}(Q_C = 0) = 0$. We then choose origins by setting Q_A, Q_B and Q_C to zero at the minima of W^A, W^B and W^C, respectively, so that $l^A = l^B = l^C = 0$. To end, we see that since centers A, B and C are equivalent, $l^{A^+} = l^{B^+} = l^{C^+} = l$, $k^{A^+} = k^{B^+} = k^{C^+} = k^+$ and $k^A = k^B = k^C = k$. The potential energies for the composite system, before any interaction between the centers is allowed, are:

$$W_a = lQ_A + \frac{k^+}{2}Q_A^2 + \frac{k}{2}Q_B^2 + \frac{k}{2}Q_C^2$$

$$W_b = lQ_B + \frac{k}{2}Q_A^2 + \frac{k^+}{2}Q_B^2 + \frac{k}{2}Q_C^2$$

$$W_c = lQ_C + \frac{k}{2}Q_A^2 + \frac{k}{2}Q_B^2 + \frac{k^+}{2}Q_C^2$$

We now introduce the new coordinates $Q_1 = \frac{1}{\sqrt{3}}(Q_A + Q_B + Q_C)$, $Q_2 = \frac{1}{\sqrt{6}}(2Q_A - Q_B - Q_C)$ and $Q_3 = \frac{1}{\sqrt{2}}(Q_B - Q_C)$ such that $Q_A = \frac{1}{\sqrt{3}}Q_1 + \frac{\sqrt{2}}{\sqrt{3}}Q_2$, $Q_B = \frac{1}{\sqrt{3}}Q_1 - \frac{1}{\sqrt{6}}Q_2 + \frac{1}{\sqrt{2}}Q_3$ and $Q_C = \frac{1}{\sqrt{3}}Q_1 - \frac{1}{\sqrt{6}}Q_2 - \frac{1}{\sqrt{2}}Q_3$. We also assume that $k^+ = k$, or that the force constant is the same in both oxidation states, which gives:

$$W_a = \frac{l}{\sqrt{3}}Q_1 + \frac{l\sqrt{2}}{\sqrt{3}}Q_2 + \frac{k}{2}\left(Q_1^2 + Q_2^2 + Q_3^2\right)$$

$$W_b = \frac{l}{\sqrt{3}}Q_1 - \frac{l}{\sqrt{6}}Q_2 + \frac{l}{\sqrt{2}}Q_3 + \frac{k}{2}\left(Q_1^2 + Q_2^2 + Q_3^2\right)$$

$$W_c = \frac{l}{\sqrt{3}}Q_1 - \frac{l}{\sqrt{6}}Q_2 - \frac{l}{\sqrt{2}}Q_3 + \frac{k}{2}\left(Q_1^2 + Q_2^2 + Q_3^2\right)$$

Because we assume that $k^+ = k$, the problem is separable with respect to Q_1, Q_2 and Q_3. Not only this, but because W_a, W_b and W_c give identical parabolas in Q_1 space, the coordinate Q_1 is superfluous. The crucial coordinates here are thus Q_2 and Q_3.

We next define the dimensionless variables $q_2 = \frac{-k}{l}Q_2$ and $q_3 = \frac{-k}{l}Q_3$

such that $Q_2 = \frac{-l}{k} q_2$ and $Q_3 = \frac{-l}{k} q_3$. We further define the parameter λ, or the reorganization energy, as $\lambda = \frac{l^2}{k}$ and so the potential surfaces in q_2–q_3 space are:

$$W_a = \lambda\left[\frac{-2}{\sqrt{6}} q_2 + \frac{1}{2}\left(q_2^2 + q_3^2\right)\right]$$

$$W_b = \lambda\left[\frac{1}{\sqrt{6}} q_2 - \frac{1}{\sqrt{2}} q_3 + \frac{1}{2}\left(q_2^2 + q_3^2\right)\right]$$

$$W_c = \lambda\left[\frac{1}{\sqrt{6}} q_2 + \frac{1}{\sqrt{2}} q_3 + \frac{1}{2}\left(q_2^2 + q_3^2\right)\right]$$

We finally let centers A, B and C interact. We denote such coupling by V and amend this to the electronic Hamiltonian:

$$H_{el} = H_{el}^{A} + H_{el}^{B} + H_{el}^{C} + V$$

If we assume that centers A, B and C are such that the overlap between orbitals on the three different centers is zero, or:

$$\left\langle \psi_i \middle| \psi_j \right\rangle = \delta_{ij} \qquad i, j = a, b, c$$

and let $H_{ij} = \left\langle \psi_i \middle| H_{el} \psi_j \right\rangle$ and $V_{ij} = \left\langle \psi_i \middle| V \psi_j \right\rangle$, then:

$$H_{aa} = W_a + V_{aa} \qquad H_{ab} = H_{ba} = V_{ab}$$

$$H_{bb} = W_b + V_{bb} = W_b + V_{aa} \qquad H_{ac} = H_{ca} = V_{ac} = V_{ab}$$

$$H_{cc} = W_c + V_{cc} = W_c + V_{aa} \qquad H_{bc} = H_{cb} = V_{bc} = V_{ab}$$

when the nuclei are held fixed at $q_2 = q_3 = 0$. The last equalities are due to the equivalency of centers A, B and C. Because the quantity V_{aa} appears only along the diagonal, we can define a new zero of energy by $V_{aa} = 0$. We also let $V_{ab} = V$. The Schrödinger equations thus become:

$$H_{el}\psi_k = W_k\psi_k \qquad \psi_k = c_{ak}\psi_a + c_{bk}\psi_b + c_{ck}\psi_c \qquad k = 1,2,3$$

$$H_{el} = \begin{bmatrix} W_a & V & V \\ V & W_b & V \\ V & V & W_c \end{bmatrix}$$

Our task is to solve the corresponding secular determinant. We seek the vibronic manifold associated with the potential surfaces W_k in order to calculate the absorption band contour that results when transitions occur between the surfaces. This contour is the so-called intervalence band.

To begin we write our *vibronic* wave functions as linear combinations of the *electronic* wave functions ψ_1, ψ_2 and ψ_3:

$$\Psi_k = \psi_1\chi_{1,k} + \psi_2\chi_{2,k} + \psi_3\chi_{3,k} \qquad k = 1,2,\cdots,\infty$$

If we allow nuclear motion, we must now use the full Hamiltonian; that is, we must include the nuclear kinetic energy operator:

$$H = H_{el} + T_n$$

Our task is to solve the *vibronic* Schrödinger equation:

$$H\Psi_k = E_k\Psi_k$$

where E_k are the vibronic eigenvalues. To do so, we multiply the vibronic Schrödinger equation by ψ_1, ψ_2 and ψ_3 in turn and integrate over electronic coordinates. We recall that $H_{el}\psi_i = W_i\psi_i$ and $\langle \psi_i | \psi_j \rangle = \delta_{ij}$ to obtain:

$$W_1\chi_{1,k} + \langle \psi_1 | T_n\psi_1 \rangle \chi_{1,k} + \langle \psi_1 | T_n\psi_2 \rangle \chi_{2,k} + \langle \psi_1 | T_n\psi_3 \rangle \chi_{3,k} = E_k\chi_{1,k}$$

$$W_2\chi_{2,k} + \langle \psi_2 | T_n\psi_1 \rangle \chi_{1,k} + \langle \psi_2 | T_n\psi_2 \rangle \chi_{2,k} + \langle \psi_2 | T_n\psi_3 \rangle \chi_{3,k} = E_k\chi_{2,k}$$

$$W_3\chi_{3,k} + \langle \psi_3 | T_n\psi_1 \rangle \chi_{1,k} + \langle \psi_3 | T_n\psi_2 \rangle \chi_{2,k} + \langle \psi_3 | T_n\psi_3 \rangle \chi_{3,k} = E_k\chi_{3,k}$$

If we assume that the nuclear kinetic energy operator commutes with the electronic wave functions ψ_i so that $T_n\psi_i\chi_{i,k} = \psi_i T_n\chi_{i,k}$, and note once more the orthonormality of the ψ_i's:

$$[W_1 + T_n]\chi_{1,k} = E_k\chi_{1,k}$$

$$[W_2 + T_n]\chi_{2,k} = E_k\chi_{2,k}$$

$$[W_3 + T_n]\chi_{3,k} = E_k\chi_{3,k}$$

We see that the vibrational function $\chi_{i,k}$ is determined only by the W_i potential surface. The nuclear motion is confined to that surface alone, and so we can write:

$$\Psi_k^{(i)} = \psi_i\chi_{i,k} \qquad i = 1,2,3 \qquad k = 1,2,\cdots,\infty$$

In other words, the Born-Oppenheimer approximation is operative.

To calculate the intervalence band contour, we sweep a vertical arrow connecting the potential surfaces in q_2–q_3 space. Much as we did in the two-center case, at each value we make a contribution to the band at an energy equal to the length of the arrow and with an intensity proportional to the product of the Boltzmann factor and the square

of the transition moment. We add together all contributions at the same transition energy and normalize the result. The totality of such lines comprises the band contour:

$$F(E) = \frac{\sum_{q_2}\sum_{q_3} e^{-W_1/k_BT}\left|\left\langle \psi_1 \left| \hat{d}\psi_i \right\rangle\right|^2 \delta[E-(W_i - W_1)]}{\sum_{q_2}\sum_{q_3} e^{-W_1/k_BT}} \qquad i = 2,3$$

Here, $E = h\nu$ is the photon energy, $\left\langle \psi_1 \left| \hat{d}\psi_i \right\rangle\right.$ is the transition dipole moment, δ is the Dirac delta function, W_1, W_2 and W_3 are the roots of the secular determinant, and the integral in the denominator is the normalizing factor. In writing such an expression, we treat the vibrational motion semiclassically.

The transition dipole moments $\left\langle \psi_1 \left| \hat{d}\psi_i \right\rangle\right.$ depend on the amount of mixing between the localized states. That is, they depend on the eigenvectors of the electronic Hamiltonian. Recall that these are of the form:

$$\psi_1 = c_{a1}\psi_a + c_{b1}\psi_b + c_{c1}\psi_c$$

$$\psi_2 = c_{a2}\psi_a + c_{b2}\psi_b + c_{c2}\psi_c$$

$$\psi_3 = c_{a3}\psi_a + c_{b3}\psi_b + c_{c3}\psi_c$$

The transition dipole moments are thus:

$$\left\langle \psi_1 \left| \hat{d}\psi_2 \right\rangle\right. = c_{a1}c_{a2}\left\langle \psi_a \left| \hat{d}\psi_a \right\rangle\right. + c_{b1}c_{b2}\left\langle \psi_b \left| \hat{d}\psi_b \right\rangle\right. + c_{c1}c_{c2}\left\langle \psi_c \left| \hat{d}\psi_c \right\rangle\right.$$

$$\left\langle \psi_1 \left| \hat{d}\psi_3 \right\rangle\right. = c_{a1}c_{a3}\left\langle \psi_a \left| \hat{d}\psi_a \right\rangle\right. + c_{b1}c_{b3}\left\langle \psi_b \left| \hat{d}\psi_b \right\rangle\right. + c_{c1}c_{c3}\left\langle \psi_c \left| \hat{d}\psi_c \right\rangle\right.$$

If we take the origin of the coordinate system as the center of the equilateral triangle formed by the equivalent centers, the moment along each coordinate is:

$$\left\langle \psi_a \left| \hat{d}_x \psi_a \right\rangle = 0 \qquad \left\langle \psi_a \left| \hat{d}_y \psi_a \right\rangle = \frac{2}{\sqrt{6}} eR \right.$$

$$\left\langle \psi_b \left| \hat{d}_x \psi_b \right\rangle = \frac{1}{\sqrt{2}} eR \qquad \left\langle \psi_b \left| \hat{d}_y \psi_b \right\rangle = \frac{-1}{\sqrt{6}} eR \right.$$

$$\left\langle \psi_c \left| \hat{d}_x \psi_c \right\rangle = \frac{-1}{\sqrt{2}} eR \qquad \left\langle \psi_c \left| \hat{d}_y \psi_c \right\rangle = \frac{-1}{\sqrt{6}} eR \right.$$

It follows that the transition moments along each coordinate are:

$$\left\langle \psi_1 \left| \hat{d}_x \psi_2 \right\rangle = \frac{eR}{\sqrt{2}} \left(c_{b1} c_{b2} - c_{c1} c_{c2} \right) \qquad \left\langle \psi_1 \left| \hat{d}_y \psi_2 \right\rangle = \frac{eR}{\sqrt{6}} \left(2c_{a1} c_{a2} - c_{b1} c_{b2} - c_{c1} c_{c2} \right) \right.$$

$$\left\langle \psi_1 \left| \hat{d}_x \psi_3 \right\rangle = \frac{eR}{\sqrt{2}} \left(c_{b1} c_{b3} - c_{c1} c_{c3} \right) \qquad \left\langle \psi_1 \left| \hat{d}_y \psi_2 \right\rangle = \frac{eR}{\sqrt{6}} \left(2c_{a1} c_{a3} - c_{b1} c_{b3} - c_{c1} c_{c3} \right) \right.$$

The square of the transition dipole moment is thus:

$$\left| \left\langle \psi_1 \left| \hat{d} \psi_2 \right\rangle \right|^2 = (eR)^2 \left[\frac{1}{2} \left(c_{b1} c_{b2} - c_{c1} c_{c2} \right)^2 + \frac{1}{6} \left(2c_{a1} c_{a2} - c_{b1} c_{b2} - c_{c1} c_{c2} \right)^2 \right] \right.$$

$$\left| \left\langle \psi_1 \left| \hat{d} \psi_3 \right\rangle \right|^2 = (eR)^2 \left[\frac{1}{2} \left(c_{b1} c_{b3} - c_{c1} c_{c3} \right)^2 + \frac{1}{6} \left(2c_{a1} c_{a3} - c_{b1} c_{b3} - c_{c1} c_{c3} \right)^2 \right] \right.$$

To end, we rewrite the delta function as the following limit:

$$\delta\left[E - \left(W_i - W_1 \right) \right] = \lim_{c \to 0} \frac{1}{2\sqrt{\pi c}} \, e^{-\left[E - (W_i - W_1) \right]^2 / 4c} \qquad i = 2,3$$

As $c \to 0$, the band contour thus becomes:

$$F(E) = \frac{\sum_{q_2}\sum_{q_3} e^{-W_1/kT} \left|\left\langle \psi_1 \left| \hat{d}\psi_i \right\rangle\right|^2 e^{-[E-(W_i-W_1)]^2/4c}}{2\sqrt{\pi c}\sum_{q_2}\sum_{q_3} e^{-W_1/kT}} \qquad i = 2,3$$

All of the models outlined here are coded in MATLAB; the programs are available upon request.

REFERENCES

[1] Sutin, N. *Prog. Inorg. Chem.* **1983**, *30*, 441.

[2] Piepho, S. B.; Krausz, E. R.; Schatz, P. N. *J. Am. Chem. Soc.* **1978**, *100*, 2996.

[3] Wong, K. Y.; Schatz, P. N. *Prog. Inorg. Chem.* **1981**, *28*, 369.

[4] Piepho, S. B. *J. Am. Chem. Soc.* **1988**, *110*, 6319.

[5] Launay, J. P.; Babonneau, F. *Chem. Phys.* **1982**, *67*, 295.